Modeling of Methane Multiple Reforming in Biogas-Fuelled SOFC and Its Application to Operation Analyses

トラン, ダン, ロン

https://doi.org/10.15017/1866295

出版情報：九州大学, 2017, 博士（工学）, 課程博士
バージョン：
権利関係：

Modeling of Methane Multiple Reforming in Biogas-Fuelled SOFC and Its Application to Operation Analyses

Tran Dang Long

Department of Hydrogen Energy Systems
Graduate School of Engineering
Kyushu University

Modeling of Methane Multiple Reforming in Biogas-Fuelled SOFC and Its Application to Operation Analyses

by

Tran Dang Long

Department of Hydrogen Energy Systems
Graduate School of Engineering
Kyushu University

SUBMITTED TO THE GRADUATE SCHOOL OF ENGINEERING IN PARTIAL FULFILLMENT OF THE REQUIREMENTS FOR THE DEGREE OF DOCTOR OF ENGINEERING

AT THE KYUSHU UNIVERSITY

JUNE 2017

Approved by:

Assoc.Prof. Yusuke Shiratori, advisor/examiner
Graduate School of Engineering, Kyushu University

Prof. Kazunari Sasaki, co-examiner
Graduate School of Engineering, Kyushu University

Prof. Kohei Ito, co-examiner
Graduate School of Engineering, Kyushu University

Prof. Takuya Kitaoka, co-examiner
Graduate School of Bioresource and Bioenvironmental Sciences, Kyushu University

Fukuoka, Japan

ABSTRACT

This research focuses on solid oxide fuel cell (SOFC) operated at high temperature (700–800 ^{o}C) with the direct feed of biogas, a gaseous mixture of 55–70 vol% CH_4 and 30–45 vol% CO_2 obtained from the anaerobic fermentation of organic matters such as garbage, livestock manure and agricultural residues. When the biogas is supplied directly to SOFC, CH_4 dry and steam reforming simultaneously occur in a porous Ni-based anode material to produce syngas (Methane multiple-reforming (MMR) process). This type of operation is called direct internal reforming (DIR) operation. Biogas-fuelled DIR-SOFC is a promising technology for sustainable development of a rural area abundant in biomass resources.

For the realization of this technology, prior to system development, operating behavior of it has to be fully understood. However, how to model the complex kinetics of MMR process was a big challenge. In this study, from the reforming data obtained in the series of systematic experiments using Ni-based anode-supported cells (ASCs), a MMR model (model parameters) was inductively generated using the approach of artificial neural network (ANN). The developed MMR model can provide the net consumption and production rates of gaseous species (CH_4, CO_2, H_2O, H_2 and CO) involved in the MMR process at arbitrary temperatures and gas compositions. And, it can be applied for different types of Ni-based catalysts by adjusting a correction factor to compensate the differences in catalytically-active surface area.

Computational fluid-dynamics (CFD) calculations, in which mass and heat transports, MMR and electrochemical processes occurring inside the cell were taken into consideration, were conducted for the DIR-SOFC fuelled by biogas. Consistency of the CFD calculation incorporating the MMR model developed in this study (MMR model-incorporated CFD) with the measured performance of SOFC fuelled by CH_4-CO_2 mixture was confirmed through a three-step model validation process consisting of two model-parameter-tuning steps (model fitting steps with the data experimentally obtained under non-DIR and DIR operations) followed by a validity check whether the established-model can reproduce a performance of DIR-SOFC under an arbitrary

operating condition. The consistency was not achieved by the conventional approach in literature considering MMR as a sum of CH_4 dry and steam reforming (ignoring the concurrent effect of CO_2 and H_2O on the catalytic CH_4 conversion). The MMR model developed in this study was proved to be able to provide more realistic and meaningful estimations for the DIR-SOFCs.

In order to enhance thermomechanical stability and output power of DIR-SOFC fuelled by biogas, internal reforming rates have to be properly controlled. For this purpose, two advanced DIR concepts, with the anode gas-barrier mask (Concept-I) and with the in-cell reformer using paper-structured catalyst (PSC) (Concept-II), were investigated by the MMR model-incorporated CFD calculation. Two types of 20×50 mm^2 ASC, ASC-A and ASC-B, with different thicknesses of anode substrate (Ni-stabilized zirconia) of 950 and 200 μm, respectively, were considered, providing guidelines for selecting a proper cell design depending on the thickness of the anode substrate (in other words the amount of metallic Ni) to obtain a mechanically stable operation with higher power density in the direct feed of simulated biogas mixture ($CH_4/CO_2 = 1$) at 800 ^oC.

For both ASC-A and ASC-B, by adopting Concept-I which can control mass flux of fuel getting into the porous volume of the anode along fuel flow direction, rapid syngas production at the fuel inlet region was suppressed to have homogeneous temperature distribution over the cell. In comparison to the normal ASCs (Normal), about 20% decrease in the maximum thermally-induced stress was estimated with a slight loss (about 8%) of maximum power density for both ASC-A and ASC-B, indicating that the use of anode gas-barrier mask is effective to reduce the risk of electrolyte fracture. Concept-I was confirmed to be a good choice for getting stable operation of DIR-SOFCs.

For the feed of 200 mL min^{-1} simulated biogas, in the cases of Normal and Concept-I, maximum power densities (P_{max}) with thinner anode substrate (ASC-B) were 1.03 and 0.95 W cm^{-2}, respectively, lower than those with thicker one (ASC-A), 1.17 and 1.08 W cm^{-2}, respectively, reflecting that the degree of catalytic CH_4 conversion is a predominant factor of the performance. In fact, by the application of Concept-II, P_{max} of ASC-A and ASC-B were boosted up to 1.25 and 1.45 W cm^{-2}, respectively, although

the risk of electrolyte fracture was increased. The effect of Concept-II was more pronounced for ASC-B with thinner anode substrate, from which H_2O (product of the anodic reaction) was easily drained. As a result, buildup of partial pressure of H_2O within the anode functional layer under high current densities, leading to the decrease in electromotive force, could be suppressed.

This study provided a powerful numerical tool for creating highly efficient and robust DIR-SOFCs operating with biogas.

This dissertation is mainly divided in six parts: overviews of SOFC and conventional modeling approaches for DIR-SOFCs are summarized in General Introduction. Investigation on electrochemical behavior of DIR-SOFC operating with biogas is presented in Chapter 2. In Chapter 3, detailed description of the ANN/FIS-based MMR model is given. CFD model of DIR-SOFC considering MMR and strategy of model validation are described in Chapter 4. The effectiveness of advanced DIR concepts is discussed in Chapter 5. Finally, important findings and outlook for future work are summarized in Chapter 6.

ACKNOWLEDGEMENTS

The study was conducted under the excellent supervision of *Assoc. Prof. Yusuke Shiratori* whom I gratefully acknowledge for his enthusiasm and many hours of helpful discussion throughout the progress of my thesis.

I wish to express my deep gratitude to *Prof. Kazunari Sasaki* for giving me the opportunity to realize this thesis in his laboratory. In particular, I greatly appreciate his valuable scientific comments and suggestions in my research. It is an honor for me that he is one of examiners of my thesis.

I am also deeply grateful to *Prof. Kohei Ito* and *Prof. Takuya Kitaoka* for being committee members of my thesis.

I would also like to thank *Assoc. Prof. Hironori Nakajima* and *Assist. Prof. Yuya Tachikawa* for their helpful supports in using COMSOL Multiphysics software and valuable discussions on SOFC calculations.

I wish to thank to *Prof. Akari Hayashi* and *Assoc. Prof. Masamichi Nishihara* for their helpful comments and suggestions in my research.

I would like to express my appreciation to *Dr. Tran Quang Tuyen* for teaching me fundamentals on SOFCs and skills on conducting experiments, as well as accompanying me during my stay in Japan.

I especially thank *Ms. Mio Sakamoto*, *Mr. Atsushi Kubota* and *Mr. Go Matsumoto*, who assisted me to collect experimental results; *Ms. Nguyen Thi Giang Huong* and *Dr. Pham Hung Cuong* who encouraged me all the time; *Ms. Tomomi Uchida*, who supported me in many things; and all other officemates and students for their support.

I also appreciate Saga Ceramic Research Laboratory (Japan) for their supporting the anode-supported half-cells.

I gratefully acknowledge to Japan International Cooperation Agency (JICA) and ASEAN University Network/Southeast Asia Engineering Education Development Network (AUN/SEED-Net) for awarding me a scholarship to study in Kyushu

University; and Japan Science and Technology Agency (JST) and Science and Technology Research Partnership for Sustainable Development (SATREPS) program for financial support on my research. I greatly appreciate *Ms. Akiko Sakono* in JICA Kyushu International Center (JICA Kyushu) for helpful supports during my PhD period.

Finally, my highest appreciation is addressed to my family: my parents, my sisters and brothers who believe in me and give me any supports without hesitation; my wife, *Thuy Ha*, who always makes me proud and has never complained for my absence at home; and my beloved children, *Vinh Khang* and *Khanh An*, who are my motivation in all circumstances.

TABLE OF CONTENTS

LIST OF FIGURES

LIST OF TABLES

LIST OF SYMBOLS

A_s	active specific surface area / m^{-1}
C_p	specific heat capacity / J kg^{-1} K^{-1}
D_{ik}	binary diffusion / m^2 s^{-1}
E_{Nernst}	Nernst voltage / V
F	Faraday constant / C mol^{-1}
h	heat transfer coefficient / J m^2 s^{-1} K^{-1}
i	current density / A m^{-2}
i_0	exchange current density / A m^{-2}
j	gaseous species flux / mol m^{-2} s^{-1}
k	thermal conductivity / W m^{-1} K^{-1}
p	partial pressure / Pa
R	gas constant / J mol^{-1} K^{-1}
q	reaction rate ratio
$\mathbf{q}$	heat flux vector
R	universal gas constant / J mol^{-1} K^{-1}
r	net reaction rate, net production or consumption rate / mol m^{-3} s^{-1}
T	temperature / K
u	velocity / m s^{-1}
x	mole fraction / -

Greek letters

α	charge transfer coefficient / -
ε	porosity / -
ϵ	emissivity / -
κ	permeability / m^2
μ	viscosity / kg m^{-1} s^{-1}
ρ	density / kg m^{-3}
σ	conductivity / S m^{-1}, thermally-induced stress / MPa
τ	tortuosity / -
ω	mass fraction / -

Subscripts

a	anode
c	cathode
e	electrolyte
i, k	gaseous species index

LIST OF ABBREVIATIONS

AFC	Alkaline Fuel Cell
AFL	Anode Functional Layer
ACCL	Anode Current Collector Layer
ANN	Artificial Neural Network
ASC	Anode-Supported Cell
CCCL	Cathode Current Collector Layer
CFL	Cathode Functional Layer
CG	Coal Gasification
CP	Methane (CH_4) pyrolysis
FIS	Fuzzy Inference System
i-V	Current-Voltage
MCFC	Molten Carbonate Fuel Cell
MMR	Methane (CH_4) Multiple Reforming
OCV	Open-Circuit Voltage
PAFC	Phosphoric Acid Fuel Cell
PEMFC	Proton Membrane Exchange Fuel Cell
RB	Reverse-Boudouard
SOFC	Solid Oxide Fuel Cell
WGS	Water-Gas Shift

CHAPTER 1

General introduction

1.1 Motivation

Biogas is a gaseous mixture obtained from the anaerobic fermentation process of organic matters from garbage, livestock manure, agricultural wastes, etc. It mainly contains CH_4 and CO_2 and traces of H_2S, N_2, H_2O as shown in Table 1.1. The calorific value of CH_4 component is the useful part of biogas. For years, biogas has widely been used as one of renewable energy sources for heating through gas burners and electricity generation through gas engine systems [1]. Due to multiple-step energy conversion mechanism (chemical → thermal → mechanical → electrical energy), energy conversion efficiency of heat engine-based generators is limited to about 25–30% [2].

Table 1.1: Typical composition of practical biogas [3].

	Concentration
CH_4	55–70 vol%
CO_2	30–45 vol%
H_2S	500–4000 ppm
NH_3	100–800 ppm
H_2	< 1 vol%
N_2	< 1 vol%
O_2	< 1 vol%
H_2O	< 1 vol%

Solid oxide fuel cell (SOFC) is a high temperature energy conversion device generating electricity via the electrochemical reaction between a fuel (H_2, CO, hydrocarbons, etc.) and oxygen. Due to single-step energy conversion mechanism (chemical → electrical energy), hydrocarbons-fuelled SOFCs are two times more efficient than conventional heat engines [4]. Compared to hydrocarbons-fuelled power systems adopting proton membrane exchange fuel cells (PEMFCs), alkaline fuel cells (AFCs), phosphoric acid fuel cells (PAFCs), and molten carbonate fuel cell (MCFC), SOFC-based systems are superior due to the elimination of external reformer, high quality waste heat, and high overall system

efficiency. Therefore, biogas-fuelled SOFC power systems are attractive technology for sustainable development (see Fig. 1.1).

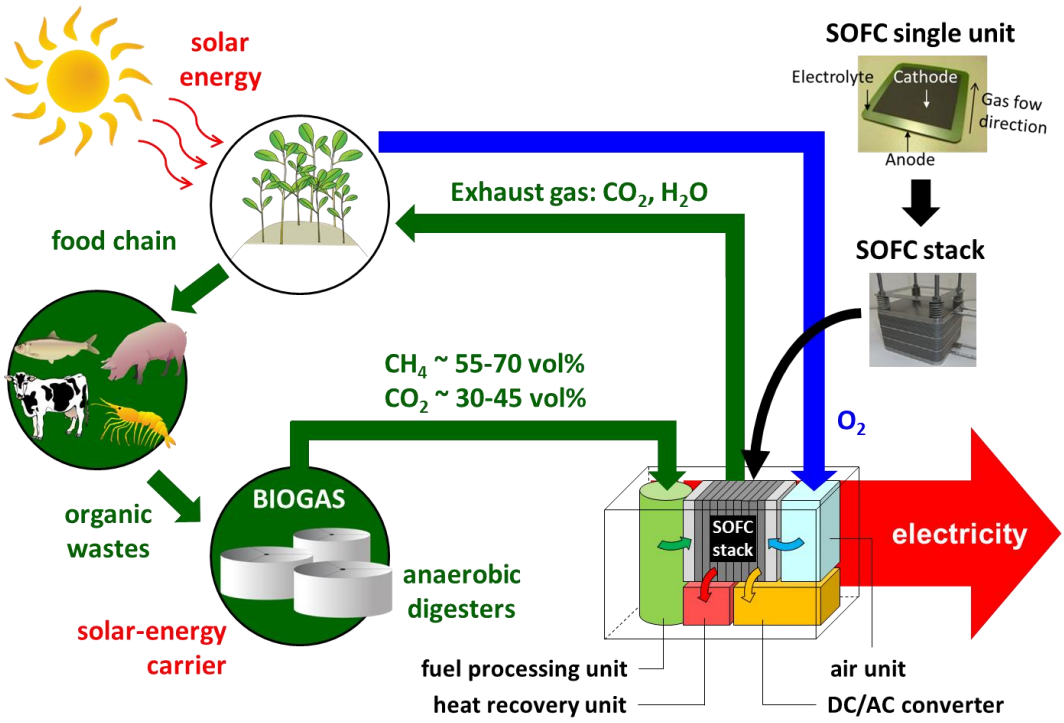

Fig. 1.1: Biogas-fuelled SOFC system as a sustainable power generator.

The feasibility of SOFCs operating with the direct feed of biogas has been intensively studied by many research groups [5–10]. In pursuit of realizing biogas-fuelled SOFC power systems, several technical issues related to stable operation must be overcome such as the risk of mechanical failures of cell components, and the degradation of cell performance caused by carbon deposition and H_2S poisoning. Numerical simulation is invaluable approach to obtain insightful estimation during operation, evaluate effectiveness of various cell/stack designs, and evaluate influences of operation parameters on SOFC performance. The estimated results can be applied for optimizing cell/stack designs and operating conditions, as a result, significantly lowering efforts, time and cost for developing SOFC-based power systems. This study aims to develop a comprehensive computational fluid-dynamics (CFD) model for an SOFC single unit running with biogas. This model includes

mass and heat transports, chemical reactions (the simultaneous CH_4 conversions with CO_2 and H_2O) and electrochemical oxidations occurring simultaneously inside the cell.

1.2 Solid Oxide Fuel Cells (SOFCs)

1.2.1 Overview

The principle of fuel cell operation was first reported by Sir W. Grove in 1839 [11]. In 1897, W. Nernst found that a solid electrolyte in thin rod-shape could become electrically conductive at high temperature [12], opening SOFC technology. The first operation of SOFC was achieved at 1000 ^oC by E. Baur and H. Preis in 1937 using a ceramic material composed of 85% zirconia and 15% yttria [13]. Since 1937, SOFC technology has rapidly matured. At the present, the most common electrolyte materials used are yttria-stabilized zirconia (YSZ) and scandia-stabilized zirconia (ScSZ) [14].

Large scale SOFC systems have been being developed aiming for distributed power plants with high energy conversion efficiency. A 140 kW SOFC cogeneration system was built by Siemens Wetinghouse in 1998, showing excellent performance [15]. Mitsubishi Heavy Industries (Japan) has developed a 200 kW-level micro-gas turbine hybrid system with a maximum efficiency of 52.1% LHV, and a rated ouput of 229 kW in AC was achieved with natural gas as a fuel [16]. Rolls-Royce Fuel Cell Systems (England) has built a stationary 1 MW SOFC power generation system based on their segmented-in-series cell stack named Integrated-Planar SOFC technology [17, 18]. FuelCell Energy (The United States) has developed SOFC power plants using SOFC stacks fabricated by Versa Power Systems (Canada) [19]. In 2015, Mitsubishi Hitachi Joint Venture started to operate a SOFC-Micro Gas Turbine (MGT) hybrid system installed at Kyushu University as a demonstrated unit [20]. The system was designed to produce a rate output of 250 kW at 55% LHV from city gas, and to operate safely and properly at an outdoor location.

Small scale SOFCs of 1–2 kW class have also been being developed all over the world for residential combined-heat-and-power (CHP) systems. City gas is generally used as a

fuel and converted to electricity and heat on site with high overall efficiency more than 80% LHV. In Japan, a demonstrative research project was carried out in which Kyocera, Tokyo gas and TOTO participated as manufacturers of SOFC stacks [21]. Long-term operation over 25,000 h has been demonstrated, and potential of 40,000 h durability has been confirmed, which led to a true commercialization source in 2011 in Japan. Ceramic Fuel Cells (Australia) has manufactured the residential system called BlueGen which can deliver initial electrical efficiency of 60% LHV at 1.5 kW in AC power with only 5% efficiency drop after one year operation [22, 23]. Hexis Ltd. (Switzerland) has operated 1 kW level system for 28000 h [24].

In 2016, Nissan introduced the world's first prototype vehicle powered by a 5-kW level SOFC generator [25]. During operation, a 24 kWh battery package is charged from the SOFC stack using H_2 produced from the reforming of 100% ethanol or ethanol-blended water. A cruising range of more than 600 km is expected for a 30 L fuel tank.

1.2.2 Working principle

Operating mechanism of an SOFC with hydrogen as a fuel is illustrated in Fig. 1.2. The solid electrolyte, an ionic conductor, is sandwiched between two porous electrodes of cathode and anode. The oxygen is supplied, usually from air, to the cathode (air electrode). When H_2 is fed to the anode (fuel electrode), a flow of oxygen ions migrates from cathode side to anode side through the solid electrolyte to oxidize H_2 at the triple-phase boundary (the interface between electrolyte and anode accessible to H_2 gas (TPB)) of anode. Electrons generated at the anode travel through external circuit to the cathode, supplying electrical power. Anode off-gas contains H_2O, product of the electrochemical oxidation of H_2 ($2H_2 + O_2 \leftrightarrows 2H_2O$). It should be mentioned that CO and hydrocarbons are also electrochemically-active species at the TPB.

The difference in chemical potential of oxygen between the cathode and the anode is the driving force for the migration of oxygen ions through the oxygen vacancies in the solid electrolyte, generating the theoretical electromotive force (E) as

$$E = \frac{\mu(O_{2,c}) - \mu(O_{2,a})}{4F} \quad (1.1)$$

,where F is the Faraday constant; the subscripts a and c indicate anode and cathode, respectively; and $\mu(O_2)$ is the chemical potential of oxygen described as

$$\mu(O_2) = \mu^0(O_2) + RTln(p_{O_2}) \quad (1.2)$$

,where μ^0 is the standard chemical potential; and p_{O_2} is the partial pressure of oxygen. Hence, E can be determined as a function of $p_{O_{2,a}}$ and $p_{O_{2,c}}$ as

$$E = \frac{RT}{4F} ln\left(\frac{p_{O_{2,c}}}{p_{O_{2,a}}}\right) \quad (1.3)$$

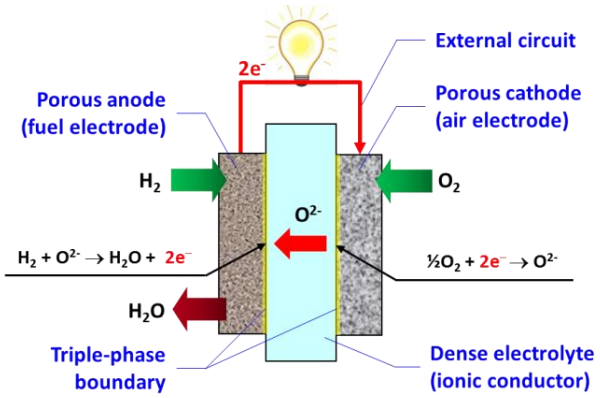

Fig. 1.2: Operating mechanism of an SOFC with H_2 as a fuel.

Considering the electrochemical oxidation of H_2, $p_{O_{2,a}}$ can be given as

$$p_{O_{2,a}} = \frac{1}{K_H}\left(\frac{p_{H_2O,a}}{p_{H_2,a}}\right)^2 \quad (1.4)$$

,where $p_{H_2,a}$ and $p_{H_2O,a}$ are the partial pressure of H_2 and H_2O; and K_H is the equilibrium constant correlated to the standard Gibbs free energy of $2H_2O$ formation (ΔG_f^0) as

$$\Delta G_f^0 = -RTln(K_H) \quad (1.5)$$

Therefore, the correlation between E and the partial pressures of reactants and products can be expressed as

$$E = -\frac{\Delta G_f^0}{4F} + \frac{RT}{2F} ln\left(\frac{p_{H_2,a}}{p_{H_2O,a}}\right) + \frac{RT}{4F} ln\left(p_{O_{2,c}}\right) \quad (1.6)$$

Ideally, open-circuit voltage (OCV) is equal to E. When current flows through the circuit, cell voltage (E_{cell}) becomes lower than the OCV due to internal losses related to ohmic losses of cell components, activation overvoltages of electrode reactions and concentration losses due to the depletions of reactants (Eq. 1.7).

$$E_{cell} = OCV - i(R_a + R_e + R_c) - \left(\eta_{act,a} + \eta_{act,c}\right) - \left(\eta_{conc,a} + \eta_{conc,c}\right) \quad (1.7)$$

,where i is the current density of the cell; R_a, R_e and R_c are the ohmic resistances of anode, electrolyte and cathode, respectively; $\eta_{act,a}$ and $\eta_{act,c}$ are the activation overvoltages of anode and cathode, respectively; $\eta_{conc,a}$ and $\eta_{conc,c}$ are the concentration losses of anode and cathode, respectively. With increase of current density, cell voltage drops because all internal losses increase. Typical current – voltage (i-V) characteristics of the cell is illustrated in Fig. 1.3.

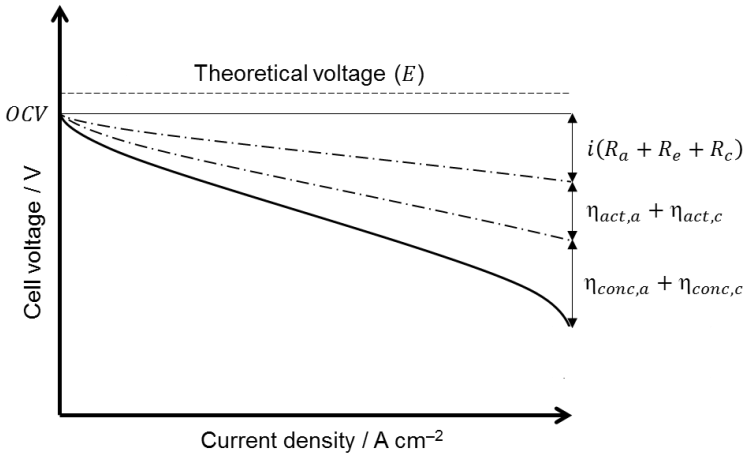

Fig. 1.3: Typical i-V characteristics of an SOFC.

1.2.3 Components

The components of an SOFC single cell are electrolyte, anode, cathode and interconnect. Each component serves several functions in SOFC operation and must meet certain requirements as shown in Table 1.2. The electrolyte has to be gas-tight to prevent leakage of fuel and oxidant gases. Both electrodes have to be porous to provide electrochemical reaction sites. The interconnector plays a role of electrically connecting the anode of one cell and the cathode of the adjoining cell, and also separating the fuel in the anode side from the oxidant in the cathode side. Component materials must be heat resistant and durable in the highly oxidative and reductive atmospheres for cathode and anode sides, respectively, in addition, must be chemically compatible and have similar thermal expansion coefficients. Typical materials of cell components are also listed in Table 1.2. To fabricate a cell, powders of these component materials are formed into desired shapes by general ceramic processing such as extrusion, slip casting, pressing, tape casting, printing and dip coating, followed by heat treatment [26].

Table 1.2: SOFC components [27].

Cell component		Requirement	Typical material
Cell	Electrolyte	Dense (gas-tight) Ionically-conductive	Y_2O_3-stabilized ZrO_2 (YSZ) Sc_2O_3-stabilized ZrO_2 (ScSZ) Gd_2O_3 doped Ce_2O (GDC) $(La,Sr)(Ga,Mg)O_3$ (LSGM)
	Anode	Porous Electrochemically-active Electronically-conductive	Ni-YSZ Ni-ScSZ Ni-GDC
	Cathode	Porous Electrochemically-active Electronically-conductive	$(La,Sr)MnO_3$ $(La,Sr)(Fe,Co)O_3$
Interconnect		Dense (gas-tight) Electronically-conductive	$(La,Sr)CrO_3$ $(La,Ca)CrO_3$ $(Sr,La)TiO_3$ Stainless steel

Various types of SOFC single cell have been designed and classified by shapes and configurations. In terms of cell shape, tubular and planar SOFCs are two basic options [14]. For tubular SOFCs, the cathode is usually made into a long-tube with a porous wall. Outside the cathode tube are the electrolyte and then the anode. Cells are connected through interconnects, as shown in Fig. 1.4-(a). For planar SOFCs, each cell is made into a flat disk or a square or rectangular plate. The cells are put in series and connected by the interconnect plates, as shown in Fig. 1.4-(b). Comparison of planar and tubular structures is summarized in Table 1.3. In earlier stage, SOFC development was focused on the tubular type. Recently, planar SOFC system has attracted much interest due to its apparently high power density.

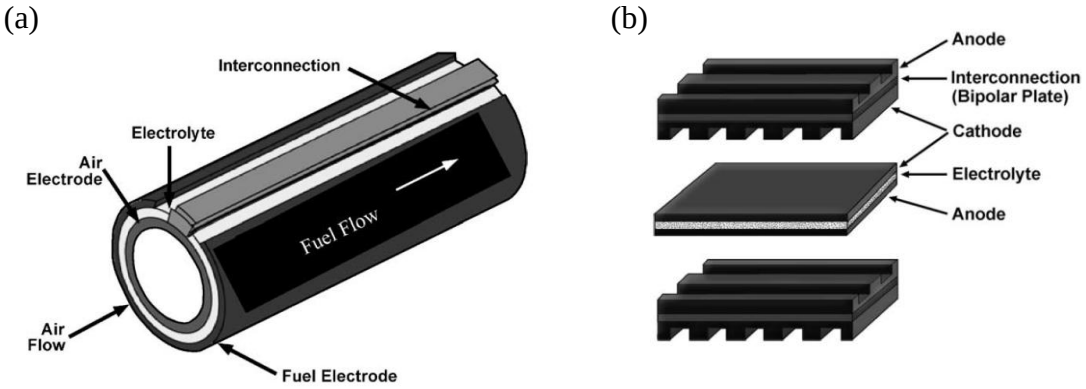

Fig. 1.4: Schematic illustrations of (a) tubular and (b) planar SOFCs [28].

Table 1.3: Comparison of tubular and planar SOFC [14].

	Tubular structure	**Planar structure**
Power density	Low	High
Fabrication process	Complicated	Simple
Fabrication cost	High	Low
Gas sealing	Easy	Difficult
Durability	Excellent	Fair
Thermal-cycling stability	Good	Fair

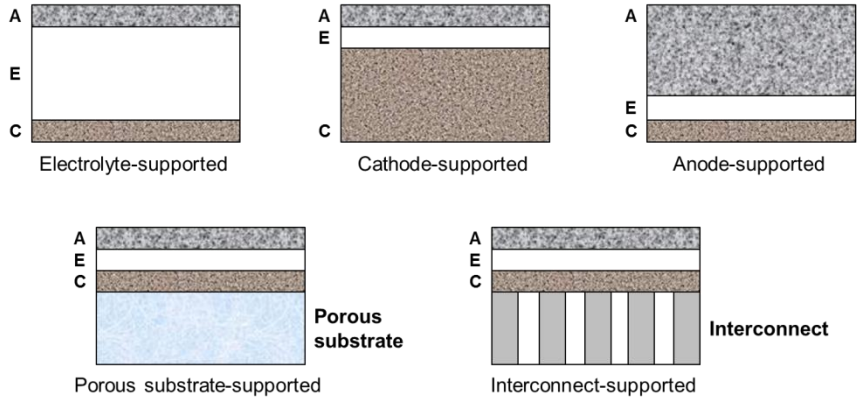

Fig. 1.5: Schematic illustrations of SOFC single cell configurations [14].

Table 1.4: Features of single cell configurations [14].

Cell configuration	Advantage	Disadvantage
Anode-supported	Highly conductive anode; Lower operating temperature via use of thin electrolyte.	Potential anode re-oxidation; Mass transport limitation due to thick anode.
Electrolyte-supported	Relative strong structural support from dense electrolyte; Less susceptible to failure due to anode re-oxidation (Ni-YSZ anode) and cathode reduction (LSM cathode).	Higher resistance due to low electrolyte conductivity; Higher operating temperature required to minimize electrolyte ohmic losses.
Cathode-supported	No-oxidant issues but potential cathode reduction; Lower operating temperature via use of thin electrolyte.	Lower conductivity; Mass transport limitation due to thick cathode.
Interconnect-supported	Lower operating temperature via thin cell components; Stronger structures from metallic interconnects.	Interconnect oxidation; Flow field design limitation due to cell support requirement.
Porous substrate	Thin cell components for low operating temperature; Potential for use of non-cell material for support to improve properties.	Increase complexity due to addition of new materials; Potential electrical shorts with porous metallic substrate due to uneven surface.

In terms of cell configuration, SOFC single cell is classified into self-supporting and external-supporting as shown in Fig. 1.5. For self-supporting configuration, the cell can be designed as anode-supported, electrolyte-supported or cathode-supported. In external-supporting configuration, the cell is fabricated as thin layers on the interconnect or a porous substrate. Comparison of single cell configurations is summarized in Table 1.4.

1.2.4 Direct internal reforming (DIR) operation

Metallic Ni has strong catalytic activity at the operating temperature range of SOFCs (600–1000 ^{o}C), making SOFCs ready for the direct use of hydrocarbon fuels. In fact, hydrocarbons can be catalytically reformed with H_2O and CO_2 within Ni-based anode materials (direct internal reforming (DIR) capability) to produce H_2 and CO, subsequently electrochemical oxidized at the TPB to generate electricity and heat. By adopting DIR operation, SOFC systems fuelled by hydrocarbons are attractive power generators since heat released by electrochemical oxidations is recycled for reforming reactions, resulting in simple balance of plants and high overall system efficiency [14, 29].

The feasibility of DIR-SOFCs operating with hydrocarbons such as pure CH_4, humidified CH_4, biogas/landfill gas (CH_4/CO_2 mixtures), propane, as well as biodiesel fuels (produced from soybean, canola, jatropha, palm and waste-cooking oils, etc.) has been demonstrated by many researchers [5–10, 30–35]. Technical issues to be solved for the realisation of DIR operation with hydrocarbons are: (I) the generation of large thermal stresses accompanied by the endothermicity of reforming reactions, (II) the deactivation of the anode due to carbon deposition, and (III) fuel impurity (sulphur, phosphorous, chlorine) poisoning.

The endothermic reforming reactions result in local temperature drops within the cell. Temperature drops are particularly noticeable at the fuel inlet, where the reforming rate is high because fuel concentration is the highest at the location [36, 37]. As a result, tensile stress is generated in the dense electrolyte thin film, causing, in the worst case, electrolyte

fracture [38–40]. However, the heat released by the exothermic electrochemical oxidation can mitigate the temperature drop, suppressing the risk of electrolyte fracture.

Since Ni is a strong C-H bond-breaker, carbon formation on Ni catalyst remarkably degrades the cell performance by covering the electrochemical and reforming reaction sites. Under load condition, carbon species deposited the Ni catalysts can be electrochemically oxidized by oxygen ions traveling through the electrolyte from the cathode [41–43]; however, carbon removal by the fuel cell current is limited to the region near the TPB [44]. Proper operating conditions such as operating temperature, steam to carbon (S/C) ratio, and fuel utilization can thermodynamically suppress carbon deposition [29]. As shown in Fig. 1.6, for a typical biogas mixture containing 60 vol% CH_4 and 40 %vol CO_2, a humidified biogas stream having S/C ratio of 1.1 is sufficient to surely avoid carbon deposition in anode porous volume under DIR operation in a temperature range of 600–1000 ^{o}C.

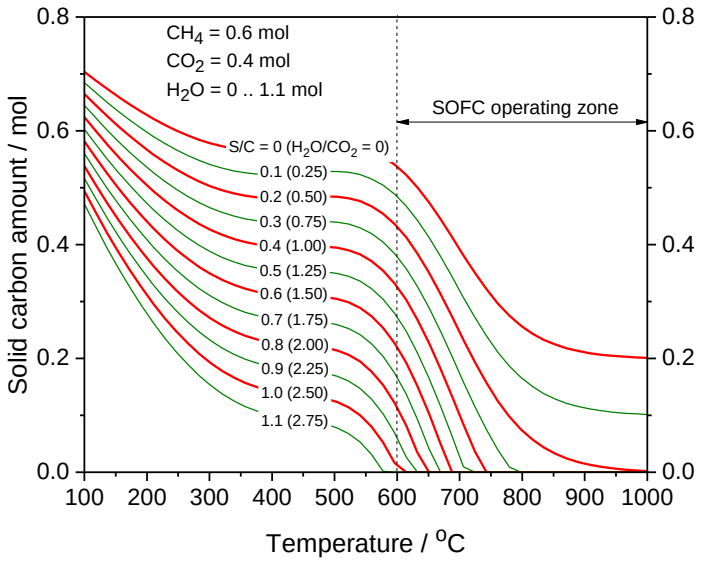

Fig. 1.6: Carbon formation boundary for humidified biogas mixtures (Fuel: CH_4:CO_2:H_2O = 0.6:0.4:x (x = 0–1.1)) calculated by HSC Chemistry 9.0 (Outotec, Finland), showing the effect of S/C on coking prevention within the operating temperature range of SOFCs.

However, additional energy is required to evaporate the water. With increase of operating temperature, the degree of humidification (S/C ratio) should be lowered to reduce the

energy burden, moreover, maximize electromotive force (power generation) of the fuel cell (see Fig. 1.7). In addition, re-oxidation of Ni metal must also be taken into consideration. To simplify the system, steam recirculation from the anode off-gas is a better approach than the use of an external humidifier [45, 46].

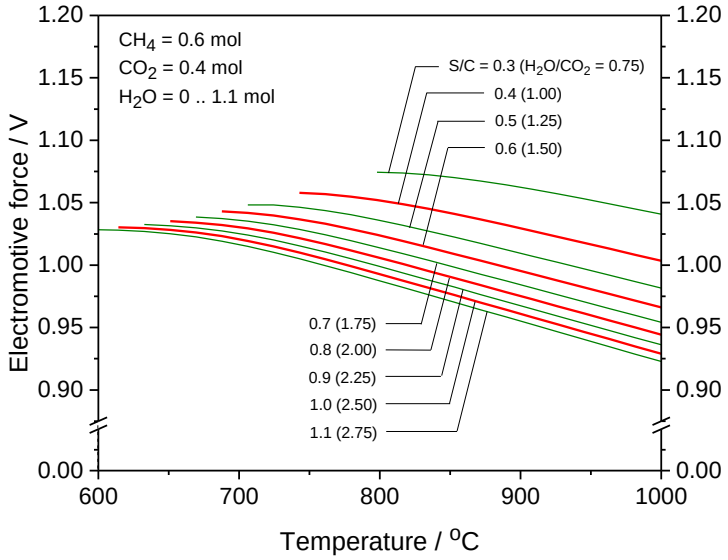

Fig. 1.7: Calculated electromotive force under open-circuit condition in DIR-SOFC operating with humidified biogas mixtures (Fuel: CH_4:CO_2:H_2O = 0.6:0.4:x (x = 0–1.1)) without carbon deposition, showing the effect of S/C on power generation.

Another approach to solve carbon deposition problem in SOFC anodes is to apply additional coking-resistant catalyst layers to quickly convert almost fuel to syngas, and thus prevent the anode from exposure to hydrocarbons [47, 48]. On the other hand, the use of chemically-inert diffusion layers has been also suggested to prevent coking through controlling mass transport [49, 50]. This gas diffusion layer suppresses the mass flux of fuel entering the anode as well as the drainage of H_2O (product of the electrochemical oxidation of H_2) to the fuel channel, in consequence, inhibiting coking due to elevated S/C ratio. By this approach, stable DIR operation can be achieved but low cell performance is noticeable.

From anode material side, coking-tolerant anode materials have been studied intensively [51–58]. Ceria-doped YSZ anodes have shown remarkably higher carbon removal rate than YSZ due to high oxygen storage capacity and rapid lattice oxygen mobility [41–53]. Copper-based anodes have been demonstrated to have high resistance to carbon formation; however, low catalytic activity of copper for electrochemical oxidations is a concern [54–56]. Ru and Pd have clearly exhibited excellent dry reforming activity and high resistance against carbon deposition [57, 58]; however, the amount of noble metal catalysts loaded must be considered because of their high costs.

Shiratori and co-workers developed paper-structured catalysts (PSCs) by loading metal-catalyst particles to inorganic fiber networks [59–64]. Due to high mechanical-flexibility and high gas diffusivity (about 90% in porosity and 20 μm in pore diameter) PSCs can easily be applied as in-cell reformers to enhance anode performance of DIR-SOFCs. In-cell reformers using hydrotalcite-dispersed PSCs have been proved to effectively prevent anode materials from H_2S poisoning during DIR operation with the direct feed of simulated biogas (CH_4/CO_2 = 1 mixture) containing 5 ppm H_2S. In addition, temperature gradient in the electrolyte caused by the endothermic CH_4 conversion could significantly be suppressed by adopting a series of functionally-graded PSCs (amount of Ni-loading is gradually increased along fuel flow direction). Therefore, PSC-based in-cell reformer is an attractive concept for downsizing and cost reduction of SOFC systems.

1.3 Overview of modeling approaches for DIR-SOFCs

Physical and chemical phenomena in the DIR-SOFC operating with CH_4-based fuels (fuel compositions of CH_4-CO_2-H_2O-H_2-CO) are illustrated in Fig. 1.8.

- In the cathode side, N_2 (the inert gaseous species) and O_2 diffuse into the cathode porous volume, and the electrochemical reduction of O_2 (reaction (1.1) listed in Table 1.5) takes place at the TPB.

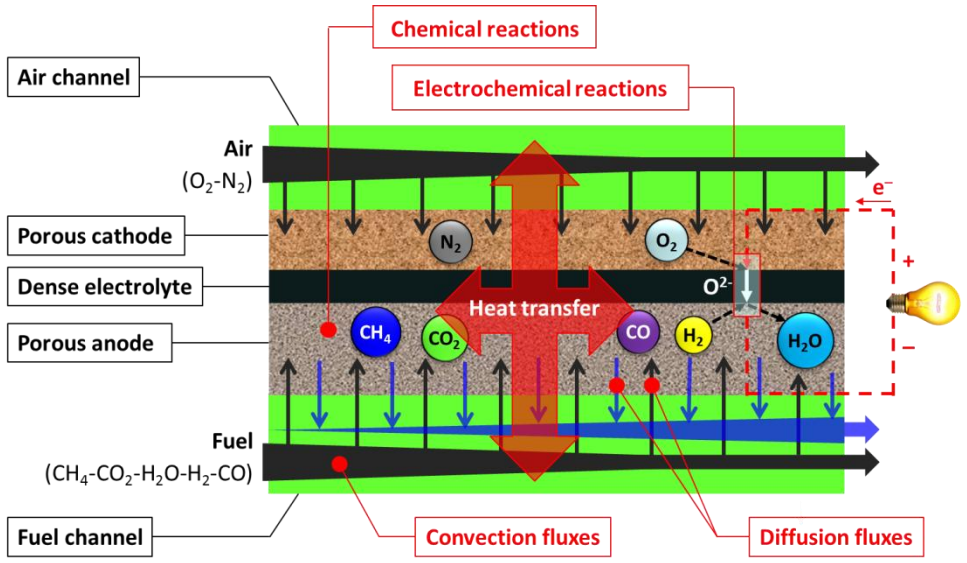

Fig. 1.8: Physical and chemical phenomena in the DIR-SOFC operating with CH_4-based fuels.

Table 1.5: Possible overall reactions in the DIR-SOFC operating with CH_4-based fuels.

No.	Overall reaction	
1.1	$½O_2 + 2e^- \leftrightarrows O^{2-}$	Electrochemical reduction (cathode TPB)
1.2	$H_2 + O^{2-} \leftrightarrows H_2O + 2e^-$	Electrochemical oxidation (anode TPB)
1.3	$CO + O^{2-} \leftrightarrows CO_2 + 2e^-$	Electrochemical oxidation (anode TPB)
1.4	$CH_4 + 4O^{2-} \leftrightarrows 2H_2O + CO_2 + 8e^-$	Electrochemical oxidation (anode TPB)
1.5	$C + 2O^{2-} \leftrightarrows CO_2 + 4e^-$	Electrochemical oxidation (anode TPB)
1.6	$CH_4 + CO_2 \leftrightarrows 2H_2 + 2CO$	Dry reforming (anode)
1.7	$CH_4 + H_2O \leftrightarrows 3H_2 + CO$	Steam reforming (anode)
1.8	$H_2O + CO \leftrightarrows H_2 + CO_2$	Water-gas shift (anode)
1.9	$CH_4 \leftrightarrows C + 2H_2$	Pyrolysis (anode)
1.10	$C + CO_2 \leftrightarrows 2CO$	Reverse-Boudouard (anode)
1.11	$C + H_2O \leftrightarrows H_2 + CO$	Coal gasification (anode)

- In the anode side, fuel diffuses into the anode porous volume where CH_4 is catalytically converted to syngas through dry and steam reforming reactions (reactions (1.6) and (1.7), respectively) on the surface of the metallic Ni particles embedded in anode material. CH_4 reforming in SOFC anode is actually a complex reaction based on the simultaneous CH_4 conversions with H_2O and CO_2, so-called methane multiple-reforming

(MMR) process. In addition, kinetically fast water-gas shift (WGS) reaction (reaction (1.8)) occurs. At the TPB of anode side, H_2, CO, CH_4 and solid C are electrochemically oxidized (reactions (1.2), (1.3), (1.4) and (1.5), respectively) to generate electricity and heat. It should be mentioned that in the MMR process the contributions of CH_4 dry and steam reforming reactions in syngas production significantly vary with respect to gas composition (CH_4-CO_2-H_2O-H_2-CO mixture).

- Reforming reactions are strongly endothermic, resulting in the formation of heat sinks in a catalytic volume. Meanwhile, during power generation, heat is released due to the exothermicity of the electrochemical oxidations. In addition, Joule's heat caused by electrical resistances of cell components and electrode overvoltages has to be taken into consideration. Spatial variation of temperature inside the cell is governed by heat convection with fluid flows, heat conduction through cell components, heat exchange between the cell and environment, and radiative heat transport within the cell.

Modeling of a DIR-SOFC is not easy since cell behavior is simultaneously affected by many processes. Appropriate modeling approaches were adopted to reduce computational time. Zero-dimensional (0D) modeling is easy for investigating output performance of a cell/stack without considering interior spatial variations [65, 66]. On the other hand, influences of mass and heat transports on the chemical and electrochemical reactions can only be solved by computational fluid-dynamics (CFD) approaches ranging from one-dimensional (1D) to three-dimensional (3D) models, which can provide unobservable information inside a real cell/stack. In a 1D model, spatial variations on one direction are of interest, and those in other two directions are assumed to be uniform [67–69]. A 2D model is greatly suitable for symmetric cell designs such as tubular and button cells where spatial variations in one direct can be neglected [70–72]. With a 3D model, the influences of cell/stack design and operating conditions on SOFC performance can be fully coupled [73–76], thus, providing more realistic results than other CFD approaches, however, computational effort is a great concern.

The most important point in the numerical evaluation of a DIR-SOFC is to establish a mathematical model describing complex phenomena inside the cell. In most cases, chemical and electrochemical reaction kinetics involving micro-scale processes are grossly simplified, and expressed as a function of temperature and gas composition. Meanwhile, mass and heat transports are usually described through physical fields of velocity, pressure and temperature, expressed by continuum partial differential equations (PDEs). Due to the complexity of the phenomena in SOFC, these PDEs cannot be solved by analytical methods. Instead, they are approximated by numerical model equations through a discretization technique commonly using finite-volume method (FVM) or finite-element method (FEM). By using numerical methods, the solution of numerical model equations which is an approximation of the real solution of the PDEs can be achieved. Being capable of exactly satisfying conservations of mass, momentum, energy and species, FVM is essentially suitable for CFD calculations, and the FVM-based commercial codes of CFD-Ace, CFX, FLUENT and STAR-CD have widely been used for numerical simulations of DIR-SOFCs [71, 77–79]. For multiphysics analysis in which different types of numerical model equations are needed to be simultaneously solved, such as the problem of thermo-mechanical stability under DIR operation, FEM can handle and provide accurate results, leading to increase in the use of the FEM-based COMSOL software package in numerical works on DIR-SOFCs [69, 72, 75, 76].

Depending on particular objectives of a study, various modeling approaches based on solid scientific theories have been adopted to express physical and chemical phenomena inside SOFCs at different levels of assumptions, and summarized in the following sections.

1.3.1 Mass transport

SOFC performance is very sensitive to mass transport of gaseous species in bulk channels and porous electrodes, since the kinetics of chemical and electrochemical reactions are strongly dependent on gas composition. Especially for DIR-SOFC, modeling of gas convection and gas diffusion whose driving forces are pressure and composition

gradients, respectively, have to be carefully performed. In the free spaces of fuel and air channels, the convection term of a gaseous species in a fluid flow can be solved by Navier-Stokes momentum equations, whereas those in porous electrodes can be expressed by Darcy-Brinkman momentum equations or sometimes assumed to be negligible [68, 80]. In porous electrodes, the diffusive mass flux of a gases species is governed by molecular (ordinary) diffusion mechanism and Knudsen diffusion mechanism; the former is related to the interactions among gas molecules in a gaseous mixture and the latter is corresponding to the collision of gas molecules with solid walls of porous media if the mean free path of gas molecules is larger than the pore diameter. As for the interdiffusion, various versions of Fick's law (FL) model, Stefan-Maxwell model (SMM) and dusty-gas model (DGM) are available selections for the modeling of SOFCs. In the operations with H_2-H_2O or CO-CO_2 mixtures, the extended Fick's law (EFL) model specified for a binary mixture including Knudsen diffusive term is the most popular selection. In multicomponent systems as DIR-SOFCs fed by CH_4-based fuels, where multiple concentration gradients (see Eq. (4.4)) must be considered to solve the diffusive term of individual gaseous species, the SMM is a choice for simplicity because Knudsen diffusion is not included in calculation [74, 76, 81, 82]. In many numerical works on DIR-SOFCs, the fidelity of the SMM was improved by adding Knudsen diffusive term to the flux equations [67, 68, 71, 83]. To obtain more realistic results, the DGM which virtually treats solid particles of the porous media as large "dust" molecules in the gas mixture is recommended for multicomponent systems since both diffusion mechanisms are included and the effect of convection motion is also considered in the calculation of gas diffusion [72, 84, 85], however, high computational-cost must be paid.

1.3.2 Heat transport

Isothermal condition is sometimes adopted in parametric studies of DIR-SOFCs for the sake of simplicity [67, 86] in spite of strong dependences of chemical and electrochemical reaction kinetics on temperature. Spatial variation of temperature inside the cell is governed by multiple heat sources and heat transport including heat convection and heat conduction

associated with thermal conductivities of gaseous species and cell components. Strong endothermic CH_4 reforming and slightly exothermic WGS reactions are chemical heat sources, and each of them can be determined as a product of the enthalpy change and the rate of the reaction. Heat sources related to power generation consist of thermodynamic heat of the electrochemical oxidations of H_2 and CO and Joule's heat caused by activation and ohmic losses. When a system is assumed to be thermally-isolated, solid walls are considered as adiabatic boundaries, and therefore, heat fluxes through solid walls are omitted [73, 74]. Radiative transport within porous electrodes can be neglected due to its minor contribution in heat transport compared to the conductive term in solid materials as reported by Damm and Fedorov [87]. Surface-to-surface radiation between electrodes and channel walls should be included for obtaining good estimation [73, 88], however, in many previous works, this was ignored to reduce the complexities in calculation [79, 89].

1.3.3 Chemical reactions

Fuel compositions of humidified CH_4 (mixtures of CH_4/H_2O), partially pre-reformed CH_4 (mixtures of CH_4-CO_2-H_2O-H_2-CO) and biogas/landfill gas (mixtures of CH_4/CO_2 or CH_4-CO_2-H_2O) have intensively been investigated in numerical studies on DIR-SOFCs [65, 71, 73, 75, 78–80, 82, 83, 90–96]. In many works, only the reaction rate of CH_4 steam reforming was solved, neglecting the contribution of CH_4 dry reforming in syngas production regardless of the presence of CO_2 in large quantity [65, 93–95] and its rate constant comparable to that of steam reforming [97]. Rate expressions for CH_4 steam reforming in SOFC anodes reported by Lehnert *et al.* [67], Achenbach and Riensche, Haberman and Young [74], [90], Xu and Froment [98] have commonly been used for determining the net consumption and production rates of CH_4, H_2O, H_2 and CO, and thermal energy involved in the CH_4 conversion as well. Not many works have taken the MMR process into account. For parametric studies on the DIR-SOFCs operated by humidified landfill gas with considerably high CO_2 content, Meng Ni ignored the concurrent effects of H_2O and CO_2 in the catalytic CH_4 conversion, and the kinetics of the MMR process was determined as the sum of the kinetics of steam and dry reforming

reactions, experimentally-derived from CH_4-H_2O and CH_4-CO_2 systems, respectively [96]. Similar approach was employed by Girona *et al.* to evaluate the risk of carbon deposition during DIR operation of an SOFC fuelled by CH_4-CO_2 mixtures [83]. Deutschmann and co-workers [99, 100] have developed an overall multistep reaction mechanism of CH_4 reforming over Ni-based catalysts, based on 42 irreversible elementary reactions, which covers almost possible reactions taking place in series and parallel in the CH_4 conversion, including CH_4 reforming reactions with H_2O and CO_2, water-gas shift reaction, reverse-Boudouard reaction, coal gasification and methanation. The use of this modeling approach for numerical assessments of DIR-SOFCs is limited due to its complexity [78, 80].

The WGS reaction has commonly been assumed to be very fast and at equilibrium. Under this condition, the partial pressures of CO, H_2O, H_2, and CO_2 (p_{CO}, p_{H_2O}, p_{H_2} and p_{CO_2}, respectively) in gas composition always satisfy the mass action law for the WGS reaction [73, 79, 81, 89], that is, $p_{H_2}p_{CO_2}/p_{CO}p_{H_2O} = K_{eq,WGS}$, where $K_{eq,WGS}$ is equilibrium constant of WGS. Generally, for the WGS reaction, empirical kinetic expressions proposed by Lehnert *et al.* [67] and Haberman and Young [74] have been taken into consideration [76, 82, 92, 96].

Under DIR operation, carbon deposition in the SOFC anode can become a severe problem because metallic Ni promotes CH_4 pyrolysis (reaction (1.9)). Besides, Boudouard reaction (reaction (1.10)) and hydrogenation of CO (reactions (1.11), respectively) must be considered as carbon forming reactions.

The risk of coking in a cell can be thermodynamically estimated by using a gas composition profile [83, 101, 102].

1.3.4 Electrochemical reactions

For simplicity, electrochemically-active zones can be considered as interfaces between electrolyte and electrodes [67, 73, 74, 86]. However, charge transfer reactions can occur within reaction zones in the vicinity of the interfaces, namely anode functional layer (AFL) and cathode functional layer (CFL) for anode and cathode sides, respectively. Thicknesses

of these functional layers are generally within 50 μm from the interface [68, 76, 79]. In the AFL, both H_2 and CO are active species for anodic reactions (reactions (1.2) and (1.3), respectively) while CH_4 is quickly reformed to syngas with CO_2 and H_2O (reactions (1.6) and (1.7), respectively) rather than electrochemically oxidized [103].

For the anodic reaction, due to the fact that the electrochemical oxidation of H_2 is kinetically 2–3 times faster than that of CO, and moreover, CO is quickly shifted to H_2 through the kinetically fast WGS reaction (reaction (1.8)) [104–107], electrochemical oxidation of H_2 has commonly been assumed to be a predominant reaction for power generation. Nevertheless, in many cases, the electrochemical oxidations of H_2 and CO were simultaneously taken into consideration [67, 73, 94, 96, 108–110], or both were independently calculated by different rate expressions experimentally-derived from H_2-H_2O and CO-CO_2 systems [78, 82, 92]. The relationship between current density and activation overvoltage can be expressed by a non-linear Butler-Volmer equation. Exchange current density can be set to a constant value [65, 78, 79, 83, 84] or expressed as a function of temperature and partial pressures of reactants and products [75, 76, 82, 101]. For simplicity, a linearized form of Butler-Volmer expression is used for determining activation overvoltage as a product of current density and charge-transfer resistance of the electrode [111].

1.3.5 Model validation

Because mathematical models of SOFC are based on different levels of assumptions, model validation is essentially necessary before further evaluations. In the work of Wang *et al.*, the fidelity of their 3D-CFD model of a planar electrode-supported SOFC was verified by comparing the current-voltage (i-V) curve measured at 1000 ^{o}C with humidified H_2 as a fuel in the current density range of 0.1–1 A cm^{-2} with the estimation [77]. Colpan *et al.* compared a measured i-V curve for the feed of CH_4-based fuel with the calculated one using their 0D model of DIR-SOFC, and reported the differences within +/–12 and +/–8% for cell voltage and output power, respectively, in the current density range of 0.1–0.6 A

cm^{-2} [65]. Razbani *et al.* proved that their 3D-CFD model could reproduce the i-V curve of a real electrolyte-supported SOFC running at 900 ^{o}C with a mixture of H_2/CO = 1 [82]. Janardhanan and Deutschmann fitted their 2D-CFD model of a button-type SOFC with i-V data measured with humidified CH_4 (CH_4/H_2O = 97/3 mixture) reported by Liu and Barnett [30]; after model-fitting, the consistence between calculated and measured results was only fairly good for the temperature range of 650–800 ^{o}C [84]. Santarelli *et al.* conducted reforming test for a tubular cell with the feed of CO_2-rich ($CO_2/CH_4 > 1$) simulated biogas mixtures, and the results of internal reforming tests obtained under open-circuit condition with CO_2/CH_4 = 2.33, 3.14 and 4 were used to correct a kinetic model describing CH_4 reforming in the anode, which was subsequently used for estimating cell behavior under load conditions [80].

It should be mentioned that in the previous works the validations of numerical models to simulate the performances of DIR-SOFCs were mostly evaluated by the fitting of the calculated i-V curves with measured curves under DIR operation. However, those are not said to be full validations, because consistencies regarding i-V curve for the feed of H_2 (non-DIR operation), ohmic and activation overvoltages, temperature distribution and reforming data were not confirmed.

1.4 Research objectives

As previously discussed in Sec **1.2.4**, the use of humidified biogas (CH_4:CO_2:H_2O mixtures) is a simple solution to prevent carbon deposition for stable DIR operation (see Fig. 1.6). S/C ratio of the fuel stream must be as low as possible for improving power generation (see Fig. 1.7) as well as overall system efficiency. Under these fuel conditions, syngas production is governed by both CH_4 dry and steam reforming reactions (the MMR process). However, the complex kinetics of MMR has not fully been modeled so far. The contribution of CH_4 dry reforming has commonly been ignored for simplicity in numerical works of DIR-SOFCs operating with CH_4-based fuel containing high CO_2 quantity, leading to the fact that cell performance could not be estimated accurately, and therefore thermo-

mechanical analysis could not be conducted. Development of a complete MMR model, which can calculate the consumption and production rates of gaseous species involved in CH_4 conversion at arbitrary temperatures and gas compositions (CH_4-CO_2-H_2O-H_2-CO mixtures), is the key to precisely estimate performance of DIR-SOFCs fed by biogas-based fuels. Besides, the contribution of the electrochemical oxidation of CO to fuel cell power generation under DIR operation is a basic question. Verifying the validity of the developed SOFC model in both non-DIR and DIR operations is also greatly important. To meet the target of this study, the following research activities were carried out:

1. Investigate electrochemical behavior of DIR-SOFCs fuelled by biogas (Chapter 2).
2. Develop a novel approach for modeling MMR in SOFC anodes (Chapter 3).
3. Design a comprehensive CFD-model of DIR-SOFCs and a solid strategy for model validation (Chapter 4).
4. Evaluate the effectiveness of DIR concepts for SOFCs operating with the direct feed of biogas using the established DIR-SOFC model (Chapter 5).

References

[1] J.B. Holm-Nielsen, T. Al Seadi, P. Oleskowicz-Popiel, The future of anaerobic and biogas digestion, Bioresour. Technol. 100 (2009) 5478–5484.
[2] K. von Mitzlaff, Engine for biogas, DTZ GmbH, German, 1998.
[3] Alves HJ *et al.*, Overview of hydrogen production technologies from biogas and the applications in fuel cells, Internal Journal of Hydrogen Energy (2010), http://dx.doi.org/10.1016/j.ijhydene.2013.02.05x7.
[4] E.D. Wachsman, C.A. Marlowe, K.T. Lee, Role of solid oxide fuel cells in a balanced energy strategy, Energy 49 (2013) 90–94.
[5] J. Staniforth, K. Kendall, Biogas powering a small tubular solid oxide fuel cell, J. Power Sources 71 (1998) 275–277.
[6] J. Van Herle, Y. Membrez, O. Bucheli, Biogas as a fuel source for SOFC co-generators, J. Power Sources 127 (2004) 300–312.

[7] G. Goula, V. Kiousis, L. Nalbandian, I.V. Yentekakis, Catalytic and electrocatalytic behaviour of Ni-based cermet anodes under internal dry reforming of CH_4+CO_2 mixtures in SOFCs, Solid States Ionics 177 (2006) 2119–2123.

[8] A. Lanzini, P. Leone, Experimental investigation of direct internal reforming of biogas in solid oxide fuel cells, Int. J. Hydrogen Energy 35 (2010) 2463–2476.

[9] Y. Shiratori, T. Ijichi, T. Oshima, K. Sasaki, Internal reforming SOFC running on biogas, Int. J. Hydrogen Energy 35 (2010) 7905–7912.

[10] M. Miyake, M. Iwami, K. Goto, K. Iwamoto, K. Morimoto, M. Shiraishi, K. Takatori, M. Takeuchi, S. Nishimoto, Y. Kameshima, Intermediate-temperature solid oxide fuel cell employing reformed effective gas: Power generation and inhibition of carbon deposition, J. Power Sources 340 (2017) 318–324.

[11] W.R. Grove, On Voltaic Series and the Combination of Gases by Platinum, Philosophical Magazine 14 (1839) 127–130.

[12] W. Nernst, Verfahren zur Erzeugung von elektrischem Glühlicht, DRP 104 872, filed (1897.07.07).

[13] E. Baur, H. Preis, Über Brennstoff-Ketten mit Festleitern, Z Elektrochem 43:727-732.

[14] N.Q. Minh, Ceramic fuel cells, J. Am. Ceram. Soc. 76(3) (1993) 563–588.

[15] National Museum of American History, Behring Center, Smithsonian Institution 2001.

[16] S. Yoshida, T. Kabata, M. Nishiura, S. Koga, K. Tomida, K. Miyamoto, Y. Teramoto, N. Matake, H. Tsukuda, S. Suemori, Y. Ando, Y. Kobayashi, Y. Development of the SOFC-GT combined cycle system with tubular type cell stack, ECS Transactions 35(1) (2011) 105–111.

[17] B. Haberman, C.M. Baca, T.R. Ohrn, IP-SOFC performance measurement and prediction, ECS Transactions 35(1) (2011) 451–464.

[18] F.J. Gardner, M.J. Day, N.P. Brandon, M.N. Pashley, M. Cassidy, SOFC technology development at Rolls-Royce, J. Power Sources 86 (2000) 122–129.

[19] P. Huang, H. Ghezel-Ayagh, SOFC module material development at fuel cell energy, ECS Transactions 35(1) (2011) 2631–2638.

[20] Mitsubishi Heavy Industries Technical Review Vol. 52 No. 4 (December 2015).

[21] K. Hosoi, M. Ito, M. Fukae, Status of national project for SOFC development in Japan, ECS Transactions 35(1) (2011) 11–18.

[22] K. Föger, Commercialisation of CFCL's residantial power station BluGen. in 9th European SOFC Forum, P. Connor, J. Irvine, M. Cassidy, C. Savaniu, M. Smith, S. Knowles Editors, European Fuel Cell Forum Proceedings Series, Switzerland, 2010, pp.2.22–2.28.

[23] R. Payne, J. Love, M. Kah, CFCL's BlueGen product, ECS Transactions 35(1) (2011) 81–85.

[24] A. Mai, B. Iwanschitz, U. Weissen, R. Denzler, D. Haberstock, V. Nerlich, A. Schuler, Status of Hexis' SOFC stack development and the Galileo 1000 N micro-CHP system, ECS Transactions 35(1) (2011) 87–95.

[25] https://newsroom.nissan-global.com/releases/160614-01-e.

[26] D. Stöver, H.P. Buchkremer, J.P.P. Huijsmans, MEA/cell preparation methods: Europe/USA, In: Handbook of Fuel Cells-Fundamentals, Technology and Applications, W. Vielstich, A. Lamm, H.A. Gasteiger (Eds.), John Wiley & Sons Ltd., England, 2003, pp.1015–1031.

[27] Y. Shiratori, Q.T. Tran, Y. Takahashi, S. Taniguchi, K. Sasaki K.. Highly Efficient Biomass Utilization with Solid Oxide Fuel Cell Technology. Chapter 8 in Renewable Energy-Trends and Applications, InTech, 2011.

[28] S.C. Singhal, Solid oxide fuel cells for stationary, mobile, and military applications, Solid State Ionics 152–153 (2002) 405–410.

[29] K. Sasaki, Y. Teraoka, Equilibria in fuel cell gases. I. Equilibirum compositions and reforming conditions, J. Electrochem. Soc. 150(7) (2003) A878–A884.

[30] J. Liu, S.A. Barnett, Operation of anode-supported solid oxide fuel cells on methane and natural gas, Solid State Ionics 158 (2003) 11–16.

[31] E.P. Murray, S.J. Harris, J. Liu, S.A. Barnett, Direct solid oxide fuel cell operation using isooctane, Eletrochem. Solid-State Lett. 9(6) (2006) A292–A294.

[32] H. Sumi, Y.H. Lee, H. Muroyama, T. Matsui, K. Eguchi, Comparison between internal steam and CO_2 reforming of methane for Ni-YSZ and Ni-ScSZ SOFC anodes, J. Electrochem. Soc. 157(8) (2010), B1118–B1125.
[33] W.A.G. McPhee, M. Boucher, J. Stuart, R.S. Parnas, M. Koslowke, T. Tao, B.A. Wilhite, Demonstration of a liquid-tin anode solid-oxide fuel cell (LTA-SOFC) operating from biodiesel fuel, Energy Fuels 23(10) (2009) 5036–5041.
[34] G. Nahar, K. Kendall, Biodiesel formulations as fuel for internally reforming solid oxide fuel cell, Fuel processing technology 92 (2011), 1345–1354.
[35] T.Q. Tran, Y. Shiratori, K. Sasaki, Feasibility of palm-biodiesel fuel for a direct internal reforming solid oxide fuel cell, Int. J. Energy Res., published online (2012).
[36] J. Wang, F. Yoshida, M. Kawase, T. Watanabe, Performance and effective kinetic models of methane steam reforming over Ni/YSZ anode of planar SOFC, Int. J. Hydrogen Energy 34 (2009) 3885–3893.
[37] Y. Takahashi, Y. Shiratori, S. Furuta, K. Sasaki, Thermo-mechanical reliability and catalytic activity of Ni-Zirconia anode supports in internal reforming SOFC running on biogas, Solid State Ionics 225 (2012) 113–117.
[38] A. Selimovic, M. Kemm, T. Torisson, M. Assadi, Steady state and transient thermal stress analysis in planar solid oxide fuel cells, J. Power Sources 145 (2005) 463–469.
[39] A. Nakajo, Z. Wuillemin, J. Van herle, D. Favrat, Simulation of thermal stresses in anode-supported solid oxide fuel stacks. Part I: Probability of failure of the cells, J. Power Sources 193 (2009) 203–215.
[40] G. Anandakumar, N. Li, A. Verma, P. Singh, J.H. Kim, Thermal stress and probability of failure analyses of functionally graded solid oxide fuel cells, J. Power Sources 195 (2010) 6659–6670.
[41] Y. Lin, Z. Zhan, J. Liu, S.A. Barnett, Direct operation of solid oxide fuel cells with methane fuel, Solid State Ionics 176 (2005) 1827–1835.
[42] A. Weber, B. Sauer, A.C. Müller, D. Herbstritt, E.I. Tiffée, Oxidation of H2, CO and methane in SOFCs with Ni/YSZ-cermet anodes, Solid State Ionics 152–153 (2002), 543–550.
[43] I.V. Yentekakis, Open- and closed-circuit study of an intermediate temperature SOFC directly fuelled with simulated biogas mixtures, J. Power Sources 160 (2006) 422–425.
[44] X.M. Ge, S.H. Chan, Q.L. Liu, Q. Sun, Solid oxide fuel cell anode materials for direct hydrocarbon utilization, Adv. Energy Mater. 2 (2012) 1156–1181.
[45] R. Peters, R. Dahl, U. Klüttgen,C. Palm, D. Stolten, Internal reforming of methane in solid oxide fuel cell systems, J. Power Sources 106 (2002) 238–224.
[46] J. Ma, C. Jiang, M. Cassidy, J.S. Irvine, Simulated biogas for nickel-based solid oxide fuel cells, J. Electrochem. Soc. 59 (1) (2014) 321–326.
[47] J.M. Klein, M. Hénault, C. Roux, Y. Bultel, S. Georges, Direct methane solid oxide fuel cell working by gradual internal steam reforming: Analysis operation, J. Power Sources 193 (2009) 331–337.
[48] S.D. Nobrega, P. Gelin, S. Georges, M.C. Steil, B.L. Augusto, F.B. Noronha, F.C. Fonseca, A fuel-flexible solid oxide fuel cell operating in gradual internal reforming, J. Electrochem. Soc. 161(3) (2014) F354–F359.
[49] Y. Lin, Z. Zhan, S.A. Barnett, Improving the stability of direct-methane solid oxide fuel cells using anode barrier layers, J. Power Sources 158 (2006) 1313–1316.
[50] H. Zhu, A.M Colclasure, R.J. Kee, Y. Lin, S.A. Barnett, Ande barrier layers for tubular solid-oxide fuel cells with methane fuel streams, J. Power Sources 161 (2006) 413–419.
[51] J.A. Farmer, C.T. Campbell, Ceria maintains smaller metal catalyst particles by strong metal-support bonding, Science 329 (2010) 933–936.
[52] O.C. Nunes, R.J. Gorte, J.M. Vohs, High mobility of ceria films on zirconia at moderate temperatures, J. Mater. Chem. 15 (2005) 1520–1522.
[53] B. Han, K. Zhao, X. Hou, D.J. Kim, B.H. Kim, S. Ha, M.G. Norton, Q. Xu, B.G. Ahn, Ni-$(Ce_{0.8-x}Ti_x)Sm_{0.2}O_{2-\delta}$ anode for low temperature solid oxide fuel cells running on dry methane fuel, J. Power Sources 338 (2017) 1–8.
[54] R. Gorte, P. Seungdoo, J. Vohs, W. Conghua, Anodes for direct oxidation of dry hydrocarbons in a solid-oxide fuel cell, Adv. Mater. 12 (2000) 1465–1469.

[55] V.V. Krishnan, S. McIntosh, R.J. Gorte, J.M. Vohs, Measurement of electrode overpotentials for direct hydrocarbon conversion fuel cells, Solid State Ionics 166 (1/2) (2004) 191–197.
[56] W. Wang, H. Zhu, G. Yang, H.J. Parl, D.W. Jung, C. Kwak, Z. Shao, A NiFeCu alloy anode catalyst for direct-methane solid oxide fuel cells, J. Power Sources 258 (2014) 134–141.
[57] M.J. Sakei, H. Uchida, M. Watanabe, Noble metal catalysts highly-dispersed on Sm-doped ceria for the application to internal reforming solid oxide fuel cells operated at medium temperature, Catal. Lett. 26 (1994) 149–157.
[58] A. Babaei, S.P. Jiang, J. Li, Electrocatalytic promotion of palladium nanoparticles on hydrogen oxidation on Ni/GDC anodes of SOFCs via spillover, J. Electrochem. Soc. 156 (2009) B1022–B1029.
[59] Y. Shiratori, T.Q. Tran, Y. Umemura, T. Kitaoka, K. Sasaki, Paper-structured catalyst for the steam reforming of biodiesel fuel, Int. J. Hydrogen Energy 38 (2013) 11278–11287.
[60] Y. Shiratori, T. Ogura, H. Nakajima, M. Sakamoto, Y. Takahashi, Y. Wakita, T. Kitaoka, K. Sasaki, Study on paper-structured catalyst for direct internal reforming SOFC fueled by the mixture of CH_4 and CO_2, Int. J. Hydrogen Energy 38 (2013) 10542–10551
[61] Y. Shiratori, M. Sakamoto, Q.T. Tran, Y. Uchiyama, N. Uchiyama, Performance of SOFC power unit assisted by paper-structured catalyst, ECS Transactions 68(1) (2015) 2783–2788.
[62] Y. Shiratori, M. Sakamoto, T. Uchida, H. Le, T. Quang-Tuyen, K. Sasaki, Hydrotalcite-dispersed paper-structured catalyst for the dry reforming of methane, Int. J. Hydrogen Energy 40 (2015) 320–327.
[63] A. Saimura, Y. Shiratori, T. Kitaoka, Dual-layer paper-structured catalysts for sequential desulfurization and methane-steam reforming of simulated biogas containing hydrogen sulfide, J. Mater. Sci. 52 (2016) 314–325.
[64] Y. Shiratori, M. Sakamoto, Performance improvement of direct internal reforming solid oxide fuel cell fuelled by H_2S-contaminated biogas with paper-structured-catalyst technology, J. Power Sources 332 (2016) 170–179.
[65] C.O. Colpan, I. Dincer, F. Hamdullahpur, Thermodynamic modeling of direct internal reforming solid oxide fuel cells operating with syngas, Int. J. Hydrogen Energy 32 (2007) 787–795.
[66] A. Baldinelli, L. Barelli, G. Bidini, Performance characterization and modeling of syngas-fed SOFCs (solid oxide fuel cells) varying fuel composition, Energy 90 (2015) 2070–2084.
[67] W. Lehnert, J. Meusinger, F. Thom, Modelling gas transport phenomena in SOFC anodes, J. Power Sources 87 (2000) 57–63.
[68] M.M. Hussain, X. Li, I. Dincer, Mathematical modeling of transport phenomena in porous SOFC anodes, Int. J. Therm. Sci. 46 (2007) 48–56.
[69] W. Kong, H. Zhu, Z. Fei, Z. Lin, A modified dusty gas model in the form of a Fick's model for the prediction of multicomponent mass transport in a solid oxide fuel cell anode, J. Power Sources 206 (2012) 171–178.
[70] M. Ni, Electrolytic effect in solid oxide fuel cells running on steam/methane mixture, J. Power Sources 196 (2011) 2027–2036.
[71] L.M. Klein, Y. Bultel, S. Georges, M. Pons, Modeling a SOFC fuelled by methane: From direct internal reforming to gradual internal reforming, Chem. Eng. Sci. 62 (2007) 1636–1649.
[72] D.H. Jeon, A comprehensive CFD model of anode-supported solid oxide fuel cells, Electrochmi. Acta 54 (2009) 2727–2736.
[73] H. Yakabe, T. Ogiwara, M. Hishinuma, I. Yasuda, 3-D model calculation for planar SOFC, J. Power Sources 102 (2001) 144–154.
[74] B.A. Haberman, J.B. Young, Three-dimensional simulation of chemically reacting gas flows in the porous support structure of an integrated-planar solid oxide fuel cell, Int. J. Heat Mass Transfer 47 (2004) 3617–3629.
[75] K. Nikooyeh, A.A. Jeje, J.M. Hill, 3D modeling of anode-supported planar SOFC with internal reforming of methane, J. Power Sources 171 (2007) 601–609.
[76] M. Andersson, H. Paradis, J. Yuan, B. Sundén, Three dimensional modeling of an solid oxide fuel cell coupling charge transfer phenomena with transport processes and heat generation, Electrochim. Acta 109 (2013) 881–893.

[77] Y. Wang, F. Yoshida, T. Watanabe, S. Weng, Numerical analysis of electrochemical characteristics and heat/species transport for planar porous-electrode-supported SOFC, J. Power Sources 170 (2007) 101–110.
[78] V. Danilov, M.O. Tadé, A CFD-based model of a planar SOFC for anode flow field design, Int. J. Hydrogen Energy 34 (2009) 8998–9006.
[79] T.X. Ho, P. Kisinski, A.C. Hoffmann, A. Vik, Transport, chemical and electrochemical processes in a planar solid oxide fuel cell: Detailed three-dimensional modeling, J. Power Sources 195 (2010) 6764–6773.
[80] M. Santarelli, F. Quesito, V. Novaresio, C. Guerra, A. Lanzini, D. Beretta, Direct reforming of biogas on Ni-based SOFC anodes: Modelling of heterogeneous reactions and validation with experiments, J. Power Sources 242 (2013) 405–414.
[81] S. Nagata, A. Momma, T. Kato, Y. Kasuga, Numerical analysis of output characteristics of tubular SOFC with internal reformer, J. Power Sources 101 (2001) 60–71.
[82] O. Razbani, M. Assadi, M. Andersson, Three-dimensional CFD modeling and experimental validation of an electrolyte supported solid oxide fuel cell fed with methane-free biogas, Int. J. Hydrogen Energy 38 (2013) 10068–10080.
[83] K. Girona, J. Laurencin, J. Fouletier, F. Lefebvre-Joud, Carbon deposition in CH_4/CO_2 operated SOFC: Simulation and experimentation studies, J. Power Sources 210 (2012) 381–391.
[84] V. Janardhanan, O. Deutschmann, CFD analysis of a solid oxide fuel cell with internal reforming: Coupled interactions of transport, heterogeneous catalysis and electrochemical processes, J. Power Sources 162 (2006) 1192–1202.
[85] Q. Wang, L. Li, C. Wang, Numerical study of thermoelectric characteristics of a planar solid oxide fuel cell with direct internal reforming of methane, J. Power Sources 186 (2009) 399–407.
[86] H. Zhu, R.J. Kee, V.M. Janardhanan, O. Deutschmann, D.G. Goodwin, Modeling elementary heterogeneous chemistry and electrochemistry in solid-oxide fuel cells, J. Electrochem. Soc. 152 (12) (2005) A2427–A2440.
[87] D.L. Damm, A.G. Fedorov, Radiation heat transfer in SOFC materials and components, J. Power Sources 143 (2005) 158–165.
[88] V.M. Janardhanan, V. Heuvelline, O. Deutschmann, Performance analysis of a SOFC under direct internal reforming conditions, J. Power Sources 172 (2007) 296–307.
[89] K.P. Recknagle, R.E. Williford, L.A. Chick, D.R. Rector, M.A. Khaleel, Three-dimensional thermo-fluid electrochemical modelling of planar SOFC stacks, J. Power Sources 113 (2003) 109–114.
[90] E. Achenbach, Three-dimensional and time-dependent simulation of a planar solid oxide fuel cell stack, J. Power Sources 49 (1994) 333–348.
[91] P. Aguiar, C.S. Adjiman, N.P. Brandon, Anode-supported intermediate temperature direct internal reforming solid oxide fuel cell. I: model-based steady-state performance, J. Power Sources 138 (2004) 120–136.
[92] H. Iwai, Y. Yamamoto, M. Saito, H. Yoshida, Numerical simulation of intermediate-temperature direct-internal-reforming planar solid oxide fuel cell, Energy 36 (2011) 2225–2234.
[93] Q. Hu, S. Wang, T.L. Wen, Analysis of processes in planar solid oxide fuel cells, Solid State Ionics 179 (2008) 1579–1587.
[94] E. Vakouftsi, G.E. Marnellos, C. Athanasiou, F. Coutelieris, CFD modeling of a biogas fuelled SOFC, Solid State Ionics 192 (2011) 458–463.
[95] F.E. Blancas, I.B. Celik, V.R. Hernandez, A.H. Guerrero, J.M.R. Avila, Numerical modeling of SOFCs operating on biogas from biodigesters, Int. J. Hydrogen Energy 28 (2013) 377–384.
[96] M. Ni, Is steam addition necessary for the landfill gas fueled solid oxide fuel cells?, Int. J. Hydrogen Energy 38 (2013) 16373–16386.
[97] J. Wei, E. Iglesia, Isotopic and kinetic assessment of the mechanism of reactions of CH_4 with CO_2 and H_2O to form synthesis gas an carbon on nickel catalysts, J. Catal. 224 (2004) 370–383.
[98] J. Xu, G.F. Froment, Methane steam reforming, methanation and water-gas shift: I. Intrinsic kinetics, AlChE J. 35 (1) (1989) 88–96.

[99] E.S. Hecht, G.K. Gupta, H. Zhu, A.M. Dean, R.K. Kee, L. Maier, O. Deutschmann, Methane reforming kinetics within a Ni-YSZ SOFC anode support, Appl. Catal., A 295 (2005) 40–51.
[100] H. Zhu, R.J. Kee, V.M. Janardhanan, O. Deutschmann, D.G. Goodwin, Modeling elementary heterogeneous chemistry and electrochemistry in solid-oxide fuel cells, J. Electrochem. Soc. 152 (12) (2005) A2427–A2440.
[101] J.M. Klein, S. Georges, Y. Bultel, Modeling of a SOFC fuelled by methane: Anode barrier to allow gradual internal reforming without coking, J. Eleoctrochem. Soc. 155(4) (2008) B333–B339.
[102] S. Assabumrungrat, N. Laosiripojana, P. Piroonlerkgul, Determination of the boundary of carbon formation for dry reforming of methane in a solid oxide fuel cell, J. Power Sources 159 (2006) 1274–1282.
[103] D. Mogensen, J.D. Grunwaldt, P.V. Hendriksen, K.D. Johansen, J.U. Nielsen, Internal steam reforming in solid oxide fuel cells: Status and opportunities of kinetics studies and their impact on modeling, J. Power Sources 196 (2011), 25–38.
[104] Y. Matsuzaki, I. Yasuda, Electrochemical oxidation of H_2 and CO in a H_2-H_2O-CO-CO_2 system at the interface of a Ni-YSZ cermet electrode and YSZ electrolyte, J. Electrochem. Soc. 147(5) (2000) 1630–1635.
[105] P. Holtappels, L.G.J. De Haart, U. Stimming, I.C. Vinke, M. Mogensen, Reaction of CO/CO2 gas mixtures on Ni-YSZ cermet electrodes, J. Appl. Electrochem. 29 (1999), 561–568.
[106] A. Weber, B. Sauer, A.C. Müller, D. Herbstritt, E.I. Tiffée, Oxidation of H_2, CO and methane in SOFCs with Ni/YSZ-cermet anodes, Solid State Ionics 152–153 (2002), 543–550.
[107] Y. Jiang, A.V. Virkar, Fuel composition and diluent effect on gas transport and performance of anode-supported SOFCs, J. Electrochem. Soc. 150(7) (2003) A942–A951.
[108] T.X. Ho, P. Kosinski, A.C. Hoffmann, A. Vik, Numerical analysis of a planar anode-supported SOFC with composite electrodes, Int. J. Hydrogen Energy 34 (2009) 3488–3499.
[109] M. Andersson, J. Yuan, B. Sundén, SOFC modeling considering hydrogen and carbon monoxide as electrochemical reactants, J. Power Sources 232 (2013) 42–54.
[110] R. Suwanwarangkul, E. Croiset, E. Entchev, S. Charojrochkul, M.D. Pritzker, M.W. Fowler, P.L. Douglas, S. Chewathanakup, H. Mahaudom, Experimental and modeling study of solid oxide fuel cell operating with syngas fuel, J. Power Sources 161 (2006) 308–322.
[111] M. Ni, Electrolytic effect in solid oxide fuel cells running on steam/methane mixture, J. Power Sources 196 (2011) 2027–2036.

CHAPTER 2

Electrochemical behavior of DIR-SOFCs operating with biogas

Understanding the electrochemical-behavior of SOFCs under DIR operation with biogas mixtures, CH_4-CO_2 or CH_4-CO_2-H_2O, is greatly important to develop realistic mathematical models of the cell. Because the electrochemical oxidations of H_2 and CO simultaneously take place at triple-phase boundary (TPB) of anode, the degree of each contribution to power generation is a basic question. In this Chapter, the electrochemical behaviors of a button-type electrolyte-supported cell (ESC) running with the direct feed of simulated biogas are presented and discussed focusing on this point.

Sec. **2.1** summarizes electrochemical characteristics of Ni-based SOFC anode with H_2 and CO. Sec. **2.2** describes electrochemical measurements for a button ESC operating with CH_4-CO_2-N_2 mixtures. The measured cell performance including reforming data, *i-V* curves and impedance spectra are presented and discussed in Sec. **2.3**. Finally, in sec. **2.4**, important findings are summarized.

2.1 Electrochemical characteristics of Ni-based anodes with H_2 and CO

The electrochemical oxidation of Ni-based anodes with H_2 and CO as a fuel have been found to be strongly dependent on at least two rate-determining processes including (1) the adsorption of fuel species on the Ni surface, followed by the diffusion of surface fuel species to TPB, where (2) charge-transfer reactions with O^{2-} take place to release electrons to the electrode [1–6]. The rate of the electrochemical oxidation of CO was reported to be 2–3 times lower than that of H_2 by Matsuzaki and Yasuda, who examined the electrochemical behavior of Ni-YSZ cermet electrodes in the temperature range of 750–1000 ^oC using H_2 and CO as a fuel [7]. Their findings are consistent with observations in many researches on the electrochemistry of CO in Ni-based anodes [8–10].

Sukeshini *et al.* investigated electrochemical characteristics of various micro-patterned Ni electrodes on YSZ electrolyte operating in a temperature range of 750–850 ^oC with H_2-CO mixtures, and reported that *i-V* curves obtained with fuel compositions with H_2/CO molar ratio above 0.33 were very close to that with pure H_2 [4]. Weber *et al.* studied electrochemical performance of a planar SOFC with Ni-YSZ cermet anode in a temperature range from 750 to 950 ^oC for H_2-CO mixtures [9]. They found that

compared to pure H_2 drops in output power for H_2-CO mixtures were insignificant even at an initial CO-content of 90%. Similarly, Jiang and Virkar demonstrated that cell performances at 800 ^oC obtained for H_2-CO mixtures containing H_2 over 45% were almost equal to that for pure H_2 [10]. Sumi *et al.* also showed that as long as H_2/CO was higher than 0.32, there were very little differences in i-V curves and anode polarization resistances of an SOFC with Ni-based anode measured at 750 and 1000 ^oC for the different feeds of H_2-CO-CO_2-N_2 mixtures [11].

In spite of the different operation conditions, they came to the same conclusion that Ni-stabilized zirconia cermet anodes working with H_2-CO mixtures show H_2-like electrochemical behavior.

When the mixtures of CH_4-CO or CH_4-CO_2-H_2O are fed to SOFC anodes, CH_4 is catalytically converted to syngas, H_2-CO mixture, through CH_4 dry and steam reforming reactions (reactions (1.6) and (1.7), respectively, listed in Table 1.5). At TPB of anode, H_2, CO, CH_4 are electrochemically oxidized simultaneously to generate electricity (reactions (1.2), (1.3) and (1.4), respectively). CH_4 most likely takes part in reforming process rather than power generation due to the fact that the rate of (1.4) is much slower than the CH_4 reforming ((1.6) and (1.7)) [12], and (1.2) and (1.3) [9, 13]. Therefore, the electrochemical behaviors of biogas-fuelled DIR-SOFCs are mainly governed by (1.2) and (1.3). In this study, degrees of contributions of H_2 and CO in DIR power generation will be discussed for the feed of biogas mixtures (CH_4-CO_2).

2.2 Experiment

Experiments were conducted using button-type electrolyte-supported cells (ESCs) fuelled by simulated biogas mixtures (CH_4-CO_2-N_2) with various CH_4/CO_2 ratios. Details of the cell fabrication and experimental procedure are described below.

2.2.1 Cell fabrication

Fig. 2.1 shows the configuration of the ESC used in this study, indicating thicknesses of cell components measured by a wide-area 3D measurement system (VR-

3100, Keyence, Japan). A disk made from commercial 10ScSZ (10 mol% Sc_2O_3-1 mol% CeO_2-ZrO_2; Daiichi Kigenso Kagaku Kogyo, JAPAN) with a diameter of 20 mm and a thickness of about 200 μm was used as the electrolyte. The paste of NiO:ScSZ with a weight ratio of 56:44 was screen printed on the electrolyte surface as the anode functional layer (AFL). After AFL paste was dried, the paste of NiO:ScSZ with a weight ratio of 80:20 was screen printed on the AFL as the anode current collector layer (ACCL), followed by sintering at 1300 ^oC in air for 3 h to obtain porous anode with a surface area of 8 × 8 mm^2. The paste of cathode functional layer (CFL), which is a mixture of ScSZ and $(La_{0.8}Sr_{0.2})_{0.98}MnO_3$ (abbreviated by LSM; Praxair, USA) with a weight ratio of 50:50, was screen printed on the opposite surface of the electrolyte disk. Then, the paste of LSM was screen printed on the dried CFL as the cathode current collector layer (CCCL), followed by sintering at 1200 ^oC in air for 5 h to obtain porous cathode. A Pt reference electrode was attached on the cathode side surface of the ScSZ disk using platinum paste.

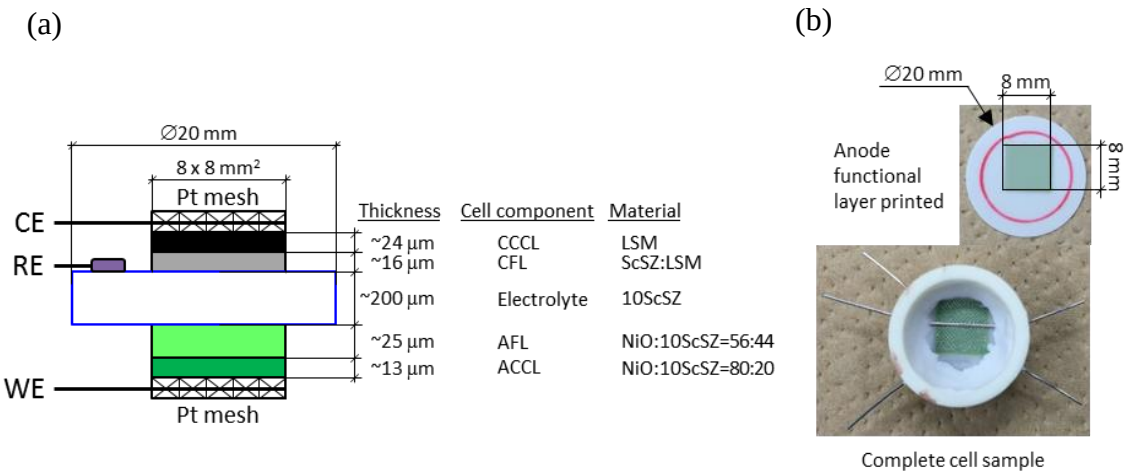

Fig. 2.1: Button-type ESC prepared in this study to investigate the electrochemical behaviour of DIR-SOFC operating with the direct feed of simulated biogas mixtures; (a) illustration of cell configuration and (b) photograph of the cell unit. WE – working electrode (anode); CE – counter electrode (cathode); and RE – reference electrode.

The button cell was sandwiched by two alumina rings to obtain a complete single unit of ESC. Ceramic bond (Aron Ceramic, TOAGOSEI Co. Ltd., Japan) was pasted around the outer and inner perimeters of the rings for gas sealing between the electrolyte and the rings.

2.2.2 Experimental setup

As shown in Fig. 2.2, an ESC was sandwiched between two alumina tubes for fuel (the lower tube) and air (the upper tube) feedings. Glass rings were inserted between the alumina rings attached to the ESC and the tubes for gas sealing at high temperature.

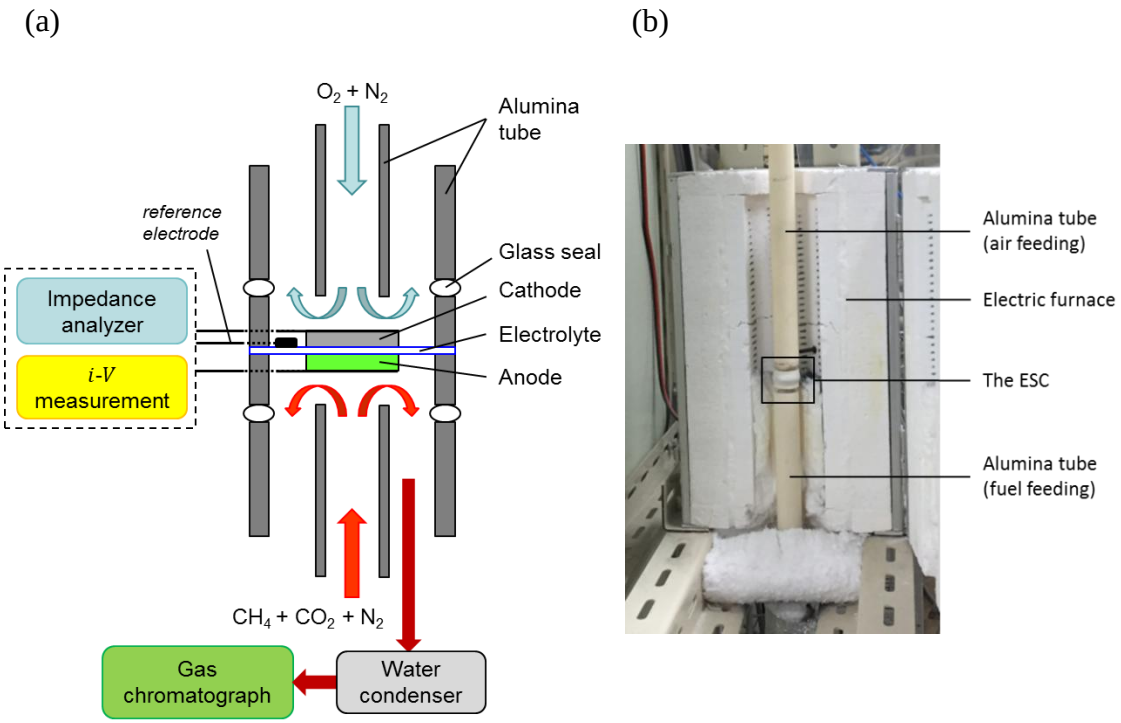

Fig. 2.2: Electrochemical measurement setup for DIR-SOFC fuelled by a simulated biogas mixture; (a) schematic drawing and (b) photograph.

After heating to 900 °C in 4.5 h in an electric furnace, 100 mL min^{-1} of pure N_2 was supplied through the inner alumina tube to purge the anode compartment for 30 min. Then, the anode gas was switched from pure N_2 to 100 mL min^{-1} of H_2/N_2 = 1:9 mixture to reduce NiO in the porous cermet anode to metallic Ni. After the reduction treatment for 2.5 h, the anode gas was switched to 80 mL min^{-1} of pure H_2 (dry), and simultaneously furnace temperature was started to reduce to the testing temperature of 800 ^{o}C. Then, a constant current of 0.256 A (equivalent to 0.4 A cm^{-2}) was applied for 200 h under the flows of pure H_2 and air (150 mL min^{-1}) for anode and cathode, respectively, for the stabilization of electrodes.

2.2.3 Experimental procedure

After the stabilization process, fuel was switched from pure H_2 to 80 mL min^{-1} of simulated biogas mixture (CH_4:CO_2:N_2). CH_4 flow rate (f_{CH_4}) was fixed at 20 mL min^{-1} corresponding to a constant partial pressure of CH_4 (p_{CH_4}) in fuel mixtures of 0.25 atm. CO_2 flow rate (f_{CO_2}) was varied from 5 to 40 mL min^{-1} corresponding to p_{CO_2} of 0.0625 to 0.5 atm, and initial CH_4/CO_2 ratio of 4.0 to 0.5, respectively. N_2 gas was used as a balance gas. Electrochemical measurements were conducted using an automatic SOFC testing system (TOYO Corporation, Japan). During the measurement of i-V curves in a current density range of 0.4 A cm^{-2}, current interruption method was applied to measure ohmic losses and electrode overvoltages. Anode-side electrochemical impedance spectra (EIS) were collected at open circuit voltage (OCV) in a frequency range of 0.1 Hz–100 kHz using an impedance analyzer (VersaSTAT 3, Ametek, UK). The anode off-gas was passed through a water trap, and its composition (dry basis) was analyzed by an automatic gas chromatograph (GC-20B, Shimadzu, Japan) under OCV condition.

After i-V measurement for a CH_4/CO_2 ratio, fuel was switched from simulated biogas mixture to 80 mL min^{-1} dry H_2, and the cell was maintained for 10 h at 0.4 A cm^{-2} to remove carbonaceous species deposited on the Ni surface, followed by an i-V measurement for dry H_2. Then, the anode gas was switched from dry H_2 to simulated biogas mixture with a desired CH_4/CO_2 ratio.

2.3 Results and discussion

2.3.1 Internal reforming behavior under open-circuit condition

There were unnoticeable deviations among i-V curves obtained for dry H_2 before each electrochemical measurement for CH_4-CO_2-N_2 mixture, indicating that anode performance was maintained throughout a series of experiments. The net production rate of H_2O (r_{H_2O}) was estimated from the balance of species (Eq. 3.2).

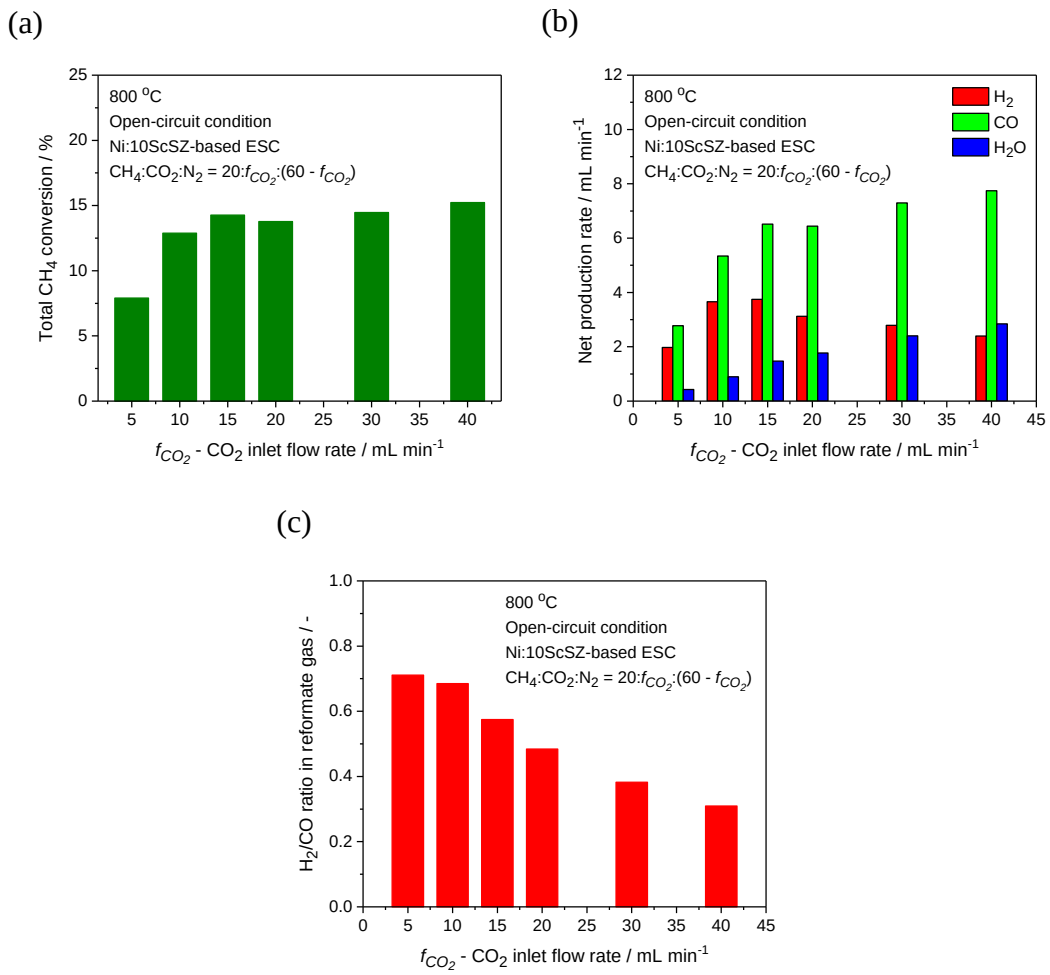

Fig. 2.3: Internal reforming behavior of ESC with Ni-10ScSZ anode (total anode thickness of about 38 μm, surface area of 8 × 8 mm^2) with 80 mL min^{-1} of simulated biogas mixtures (CH_4:CO_2:N_2 = 20:f_{CO_2}:(60 – f_{CO_2})) measured at 800 °C; (a) total CH_4 conversion, (b) net production rates of H_2, CO and H_2O and (c) H_2/CO molar ratio of reformate gas with respect to CO_2 inlet flow rate (f_{CO_2}).

Fig. 2.3 presents internal reforming behavior under open-circuit condition with 80 mL min^{-1} of simulated biogas mixtures (CH_4:CO_2:N_2 = 20:f_{CO_2}:(60 – f_{CO_2})). Total CH_4 conversion (χ_{CH_4}) did not exceed 15% under the experimental conditions of this study (see Fig. 2.3-(a)). At a constant f_{CH_4} of 20 mL min^{-1}, χ_{CH_4} sharply increased from about 8 to 14% with increasing f_{CO_2} from 5 to 15 mL min^{-1}. Further increase of f_{CO_2} to 40 mL min^{-1}, χ_{CH_4} became insusceptible to f_{CO_2}. The similar trend of χ_{CH_4} with respect to f_{CO_2} at a constant f_{CH_4} has been observed in the work of Bradford and Vannice, who

investigated the reaction kinetics of CH_4 dry reforming over Ni-based catalysts in a temperature range of 400–600 ^oC [14]. Tsipouriari and Verykios also reported the same tendencies on the catalytic behavior of CH_4 conversion with CO_2 over a Ni-La_2O_3 catalyst from 650 to 750 ^oC [15].

The net production rates of H_2, CO and H_2O are shown in Fig. 2.3-(b). Sum of the net production rates of H_2 and CO was not higher than 10.5 mL min^{-1}. The reverse-WGS reaction (reaction (1.8)) also took place, resulting in H_2/CO ratio less than 1 in the reformate gas (see Figs. 2.3-(c)). The dissociation of H_2O on the Ni surface could result in O(Ni) species [16] which have been found to accelerate surface diffusion of H_2 to TPB via spillover mechanism [1]. In the work of Jiang and Virkar as mentioned in Section **2.1**, limiting current densities measured at 800 ^oC for H_2 diluted with H_2O were 20–44% higher than those for H_2 diluted with CO_2 at the same degrees of dilution, suggesting that the adsorption of CO_2 on the Ni surface did not lead to the formation O(Ni) species (refer to Appendix A). Hence, under DIR operation O(Ni) concentration was greatly dependent on the partial pressure of H_2O (p_{H_2O}).

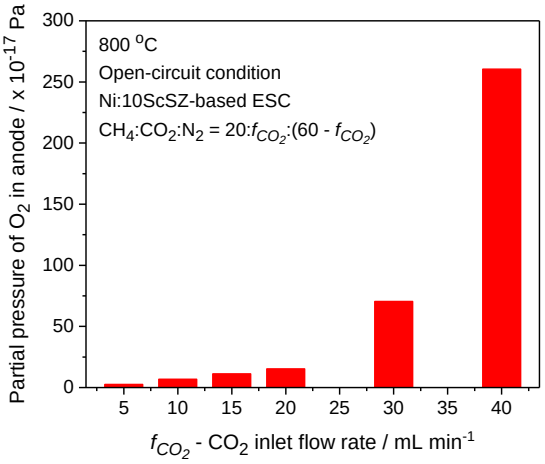

Fig. 2.4: Thermodynamically-calculated partial pressure of oxygen in anode side ($p_{O_2,a}$) with respect to CO_2 inlet flow rate (f_{CO_2}) at 800 ^oC for 80 mL min^{-1} of simulated biogas mixtures (CH_4:CO_2:N_2 = 20:f_{CO_2}:(60 – f_{CO_2})).

While CH_4 conversion was not further promoted for f_{CO_2} > 15 mL min^{-1}, reverse-WGS reaction still proceeded, keeping shift of H_2 to H_2O. O(Ni) concentration therefore

increased with increasing f_{CO_2} under a constant f_{CH_4}. In addition, $p_{O_2,a}$, calculated with HSC Chemistry 9.0 software package (Outotec, Finland), increased with increasing f_{CO_2} as f_{CH_4} was fixed (see Fig. 2.4), indicating that interfacial conductivity of anode also increased [17].

Enhanced O(Ni) concentration and $p_{O_2,a}$ in DIR operation can promote surface diffusion of H_2 (refer to Appendix A), and this makes H_2 predominant electrochemical reactant rather than CO.

2.3.2 Electrochemical impedance for simulated biogas mixtures

Fig. 2.5 shows anode-side impedance spectra under open-circuit condition for different CH_4-CO_2-N_2 mixtures at f_{CH_4} = 20 mL min^{-1}. For f_{CO_2} varying from 5 to 40 mL min^{-1}, impedance spectra consisted of two arcs partially overlapped, suggesting that the anodic reaction is controlled by at least two rate-determining processes associated with mass-transfers of gaseous species to and from TPB and fuel conversion (low frequency arc), and charge-transfer processes at TPB (high frequency arc) [1, 2, 18, 19].

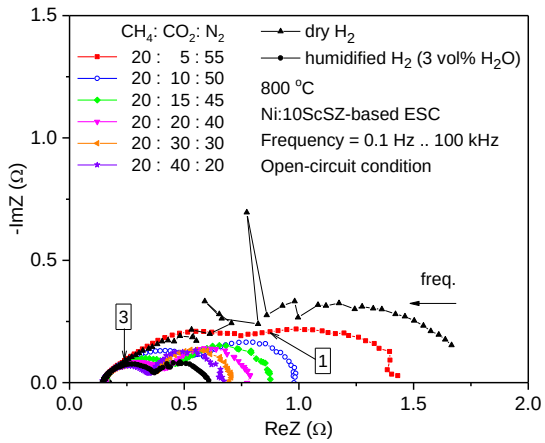

Fig. 2.5: Anode-side impedance spectra at 800 °C for the ESC with Ni-10ScSZ measured under open-circuit condition with 80 mL min^{-1} of different CH_4-CO_2-N_2 mixtures. Spectra for dry and humidified H_2 were also plotted for the comparison. Number in the box indicates the value of power.

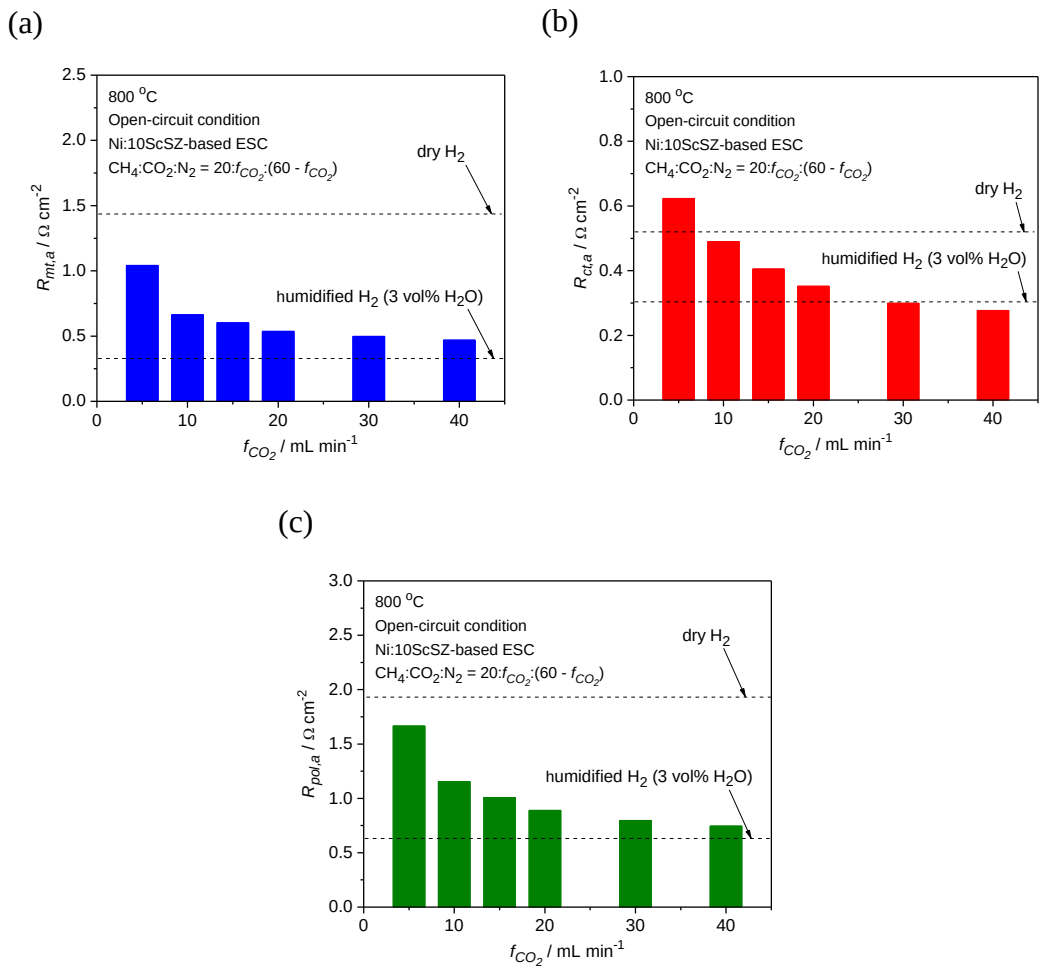

Fig. 2.6: Polarization resistances of Ni-10ScSZ anode at 800 °C obtained in the EIS under open-circuit condition with 80 mL min^{-1} of simulated biogas mixtures (CH_4:CO_2:N_2 = 20:f_{CO_2}:(60 – f_{CO_2})); (a) mass-transfer resistance ($R_{mt,a}$), (b) charge-transfer resistance ($R_{ct,a}$)and (c) polarization resistance ($R_{pol,a}$ = $R_{mt,a}$ + $R_{ct,a}$) with respect to CO_2 inlet flow rate, f_{CO_2}.

As shown in Fig. 2.5, the size of low- and high-frequency arcs decreased with increasing f_{CO_2} at constant f_{CH_4}. Mass-transfer, charge-transfer and total polarization resistances of anode, $R_{mt,a}$, $R_{ct,a}$ and $R_{pol,a}$ (= $R_{mt,a}$ + $R_{ct,a}$), respectively, with respect to f_{CO_2} under open-circuit condition are plotted in Fig. 2.6. $R_{mt,a}$ and $R_{ct,a}$ for humidified H_2 (3 vol% H_2O) was smaller than those for dry H_2. The effect of humidification was more pronounced for $R_{mt,a}$ compared to $R_{ct,a}$, indicating the promotion of surface diffusion of H_2 on the O(Ni) species through the spillover mechanism [1]. When the fuel was switched from dry H_2 to simulated biogas mixtures,

$R_{mt,a}$ remarkably reduced and approached that for humidified H_2 with increasing f_{CO_2} (see Fig. 2.6-(a)). This suggests that under DIR operation total diffusion rate of electrochemically-active species (H_2 and CO) to TPB was considerably enhanced in spite of low concentrations of H_2 and CO. Whereas the surface diffusion of H_2 to TPB is accelerated over O(Ni) species, that of CO could be suppressed by the coverage of H_2O (or O(Ni) species) (refer to Appendix A). Therefore, it can be said that the variation of $R_{mt,a}$ with CH_4/CO_2 ratio is tightly associated with the mass-transfer process of H_2. $R_{ct,a}$ decreased with increasing f_{CO_2} in the fuel stream (see Fig. 2.6-(b)) and converged to the value of humidified H_2, indicating the dominancy of H_2 in the charge-transfer process for the simulated biogas mixture with $CH_4/CO_2 < 1$.

It was revealed that under the working conditions of internal dry reforming of CH_4 CO plays little part in the electrochemical process, and it is governed by the electrochemical oxidation of H_2, even though H_2/CO ratio of reformate gas was as low as 0.3.

2.3.3 *i-V* characteristics

i-V curves for the direct feed of simulated biogas mixtures were plotted in Fig. 2.7, where *i-V* curves for the dry- and humidified-H_2 (3 vol% H_2O) were also shown. Due to higher $p_{O_2,a}$ for humidified-H_2 compared to dry H_2, OCV was 90 mV lower than that of the case of dry H_2 (1.166 V). Below 0.1 A cm^{-2}, an obviously lower slope of the *i-V* curve was observed for humidified H_2 compared to dry H_2, showing the positive effect of H_2O to accelerate the electrochemical oxidation of H_2 [1, 3, 17, 18]. For the simulated biogas mixtures, by increasing f_{CO_2} from 5 to 40 mL min^{-1}, OCV decreased from 1.030 to 0.891 V due to increase in $p_{O_2,a}$. Below 0.1 A cm^{-2}, the slope of *i-V* curves decreased with increase in f_{CO_2}. Further increase in current density, the slopes of *i-V* curves became comparable to H_2. In the range between 0.2 and 0.4 A cm^{-2}, all *i-V* curves had linear tendency against current density with almost the same gradients, suggesting that the cell voltage drop was mainly attributed to ohmic resistances, and insensitive to activation overvoltages.

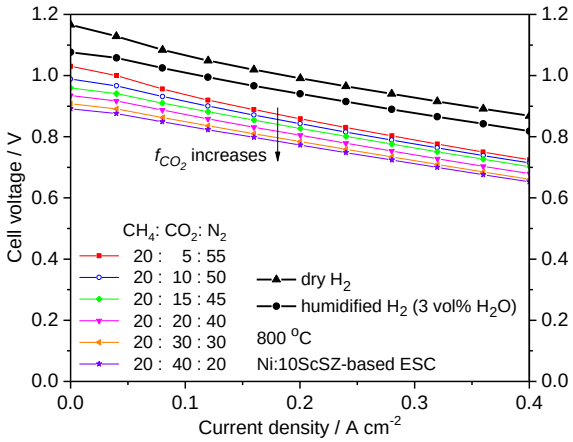

Fig. 2.7: *i-V* curves of ESC with Ni-10ScSZ anode measured at 800 °C with 80 mL min^{-1} of simulated biogas mixtures (CH_4:CO_2:N_2 = 20:f_{CO_2}:(60 – f_{CO_2})). *i-V* curves for dry and humidified H_2 were also plotted for the comparison.

Fig. 2.8 shows anode activation overvoltage ($\eta_{act,a}$) for the feed of simulated biogas mixtures. $\eta_{act,a}$ dramatically decreased as f_{CO_2} was varied from 5 to 15 mL min^{-1}. Further increase in f_{CO_2} to 40 mL min^{-1}, $\eta_{act,a}$ became insensitive to f_{CO_2} change. These observations were consistent with the decrease in $R_{pol,a}$ under open-circuit condition (see Fig. 2.6-(c)).

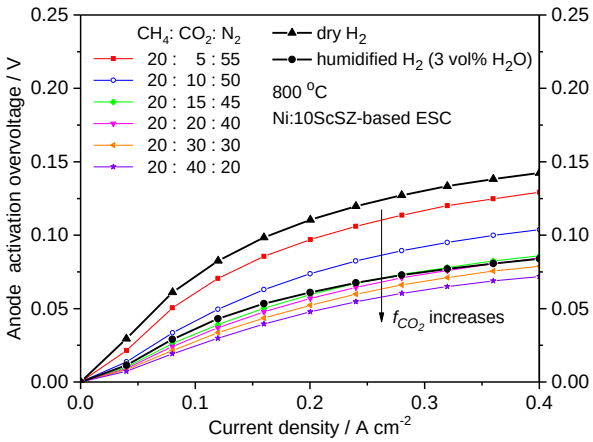

Fig. 2.8: Activation overvoltage ($\eta_{act,a}$) of Ni-10ScSZ measured at 800 °C with 80 mL min^{-1} of simulated biogas mixtures (CH_4:CO_2:N_2 = 20:f_{CO_2}:(60 – f_{CO_2})). $\eta_{act,a}$ for dry and humidified H_2 were also plotted for the comparison.

$\eta_{act,a}$ of simulated biogas mixtures was lower than that of dry H_2 for all CH_4/CO_2 ratios tested in this study due to the promotions of mass-transfer and charge-transfer processes, even though concentrations of H_2 and CO available in the anode were low level. This, again, shows the contribution of O(Ni) species to increase electrode interfacial conductivity, and anodic reaction for the feed of simulated biogas mixtures is governed by H_2 oxidation regardless of H_2/CO ratio as low as 0.3.

2.4 Conclusions

Under DIR operation, the electrochemical oxidations of H_2 and CO simultaneously proceed at the triple-phase boundary (TPB) of anode. The degree of each contribution to power generation must be clearly defined for accurate performance calculations of DIR-SOFCs operating with biogas. To answer this question, in this study, electrochemical experiments using button-type SOFC single cells with Ni-ScSZ anode were conducted at 800 ^{o}C with the direct feed of simulated biogas (CH_4:CO_2:N_2 = 20:f_{CO_2}:(60 – f_{CO_2})).

Reforming data obtained under open-circuit condition showed that the H_2/CO molar ratio of syngas produced internally via CH_4 dry reforming ($CH_4 + CO_2 \leftrightarrows 2H_2 + 2CO$) was less than 1, and continuously decreased with increasing CO_2 flow rate (f_{CO_2}) because of reverse-WGS reaction ($CO_2 + H_2 \leftrightarrows H_2O + CO$). O(Ni) might be present in the anode due to the dissociation of H_2O (by-product of reverse-WGS reaction) on the Ni surface (H_2O + (Ni) $\leftrightarrows$ H_2 + O(Ni)). O(Ni) concentration increased with increase of the partial pressure of H_2O (p_{H_2O}), which rose with the promotion of reverse-WGS reaction as f_{CO_2} increased. Oxygen partial pressure in anode side ($p_{O_2,a}$) also increased with increase of oxygen carrier content (here, CO_2) in the fuel stream, leading to decrease in open-circuit voltage (OCV).

Impedance data measured at anode side revealed that surface diffusion of electrochemically active species to the TPB was significantly accelerated with increasing O(Ni) concentration or $p_{O_2,a}$. At the same time, charge-transfer reactions were noticeably promoted. These electrochemical behaviors were identical with those of Ni-based anodes fuelled by H_2. Because the electrochemical oxidation of CO is known to be suppressed by the presence of H_2O to form O(Ni), it can be concluded that in the

DIR operation H_2 is electrochemically active and electrochemical contribution of CO to power generation is negligibly small, even though H_2/CO ratio is as low as 0.3.

References

[1] S.P. Jiang, S.P.S. Badwal, Hydrogen oxidation at the nickel and platinum electrodes on yttria-tetragonal zirconia electrolyte, J. Electrochem. Soc. 144(11) (1997), 3777–3784.

[2] S. Primdahl, M. Mogensen, Oxidation of hydrogen on Ni/yttria-stabilized zirconia cermet anodes, J. Electrochem. Soc. 144(10) (1997), 3409–3419.

[3] W. Bessler, J. Warnatz, D.G. Goodwin, The influence of equilibrium potential on the hydrogen oxidation kinetics of SOFC anodes, Solid State Ionics 177 (2007), 3371–3383.

[4] A.M. Sukeshini, B. Habibzadeh, B.P. Becker, C.A. Stoltz, B.W. Eichhorn, G.S. Jackson, Electrochemical oxidation of H_2, CO and CO/H_2 mixtures on patterned Ni anodes on YSZ electrolytes, J. Electrochem. Soc. 153(4) (2006) A705–A715.

[5] V. Yurkiv, D. Starukhin, H.-R. Volpp, W.G. Bessler, Elementary reaction kinetics of the CO/CO_2/Ni/YSZ electrode, J. Electrochem. Soc. 158(1) (2011), B5–B10.

[6] G.Ø. Lauvstad, R. Tunold, S. Sunde, Electrochemical oxidation of CO on Pt and Ni point electrodes in contact with an ytrria-stabilized zirconia electrolyte, J. Electrochem. Soc. 149(2) (2002) E497–E505.

[7] Y. Matsuzaki, I. Yasuda, Electrochemical oxidation of H_2 and CO in a H_2-H_2O-CO-CO_2 system at the interface of a Ni-YSZ cermet electrode and YSZ electrolyte, J. Electrochem. Soc. 147(5) (2000) 1630–1635.

[8] P. Holtappels, L.G.J. De Haart, U. Stimming, I.C. Vinke, M. Mogensen, Reaction of CO/CO_2 gas mixtures on Ni-YSZ cermet electrodes, J. Appl. Electrochem. 29 (1999), 561–568.

[9] A. Weber, B. Sauer, A.C. Müller, D. Herbstritt, E.I. Tiffée, Oxidation of H_2, CO and methane in SOFCs with Ni/YSZ-cermet anodes, Solid State Ionics 152–153 (2002), 543–550.

[10] Y. Jiang, A.V. Virkar, Fuel composition and diluent effect on gas transport and performance of anode-supported SOFCs, J. Electrochem. Soc. 150(7) (2003) A942–A951.

[11] H. Sumi, Y.H. Lee, H. Muroyama, T. Matsui, K. Eguchi, Comparison between internal steam and CO_2 reforming of methane for Ni-YSZ and Ni-ScSZ SOFC anodes, J. Electrochem. Soc. 157(8) (2010), B1118–B1125.

[12] D. Mogensen, J.D. Grunwaldt, P.V. Hendriksen, K.D. Johansen, J.U. Nielsen, Internal steam reforming in solid oxide fuel cells: Status and opportunities of kinetics studies and their impact on modeling, J. Power Sources 196 (2011), 25–38.

[13] Y. Lin, Z. Zhan, J. Liu, S.A. Barnett, Direct operation of solid oxide fuel cell with methane fuel, Solid State Ionics 176 (2005), 1827–1835.

[14] M.C.J. Bradford, M.A. Vannice, Catalytic reforming of methane with carbon dioxide over nickel catalysts. II. Reaction kinetics, Appl. Catal., A 142 (1996), 97–122.

[15] V.A. Tsipourari, X.E. Verykios, Kinetic study of the catalytic reforming of methane with carbon dioxide to synthesis gas over Ni/La_2O_3 catalyst, Catal. Today 64 (2001), 83–90.

[16] C. Benndorf, C. Nobl, M. Rusenberg, F. Thieme, Appl. Surf. Sci. 11–12 (1982), 803–811.

[17] J. Mizusaki, H. Tagawa, T. Saito, T. Yamamura, K. Kamitani, K. Hirano, S. Ehara, T. Takagi, T. Hikita, M. Ippommatsu, S. Nakagawa, K. Hashimoto, Kinetics studies of the reaction at the nickel pattern electrode on YSZ in H_2-H_2O atmospheres, Solid State Ionics, 70/71 (1994), 52–58.

[18] S.P. Jiang, S.P.S. Badwal, An electrode kinetics study of H2 oxidation on Ni/Y_2O_3–ZrO_2 cermet electrode of the solid oxide fuel cell, Solid State Ionics 123 (1999), 209–224.

[19] Y. Shiratori, M. Sakamoto, Performance improvement of direct internal reforming solid oxide fuel cell fuelled by H_2S-contaminated biogas with paper-structured catalyst technology, J. Power Sources 332 (2016), 170–179.

CHAPTER 3

Modeling of methane multiple-reforming within the Ni-based anode of an SOFC

Humidification of biogas is effective to suppress coke formation within SOFC anodes. Because CO_2 in biogas stream is an available oxygen-carrier, the degree of humidification should be as low as possible for maximizing overall system efficiency. Under these fuel conditions, simultaneous dry and steam reforming of CH_4, namely methane multiple-reforming (MMR), must be considered in numerical evaluations. In this Chapter, a novel approach using an approximation method based on artificial neural network ((ANN), refer to Appendix B) and fuzzy inference system ((FIS), refer to Appendix C) is described for the modeling of the MMR process, covering important catalytic aspects such as partial pressure dependence, temperature sensitivity, and the concurrent effects of CO_2 and H_2O in the catalytic CH_4 conversion. The overall CH_4 reforming within a Ni-based cermet anode can thus be expressed by a single model for arbitrary temperatures and gas compositions of CH_4, CO_2, H_2O, H_2 and CO.

In Sec. **3.1**, the ANN/FIS-based MMR model is described. Experiments and model-parameters determination are mentioned in Sec. **3.2**. Validity check is presented in Sec. **3.3**. Important findings are summarized in Sec. **3.4**.

3.1 Model description

It is impossible for the conventional approaches such as power-law model fitting, first order reaction kinetics related to CH_4 partial pressure and Langmuir-Hinshelwood kinetics to fully express the catalytic behavior of Ni-stabilized zirconia cermet anodes under DIR operation with biogas.

In this study, a novel approach adopting ANN and FIS for directly calculating net consumption and production rates of all gaseous species (CH_4, CO_2, H_2O, H_2 and CO) involved in the MMR was proposed. Reaction rates of dry and steam reforming of CH_4 (reactions (1.6) and (1.7), respectively, listed in Table 1.5) on Ni-based catalysts have been generally accepted to be tightly involved in the rate of CH_4 decomposition on the Ni surface [1–4]; in this rate-determining step, active carbon and hydrogen adatoms are simultaneously formed (reaction (1.9)). CH_4 dry reforming can thus be considered to be activated with CH_4 pyrolysis, followed by a reverse-Boudouard reaction (reaction (1.10)) [5]. Similarly, CH_4 steam reforming can be expressed as CH_4 dissociation,

followed by coal gasification (reaction (1.11)) [6]. The final H_2/CO ratio is determined by the kinetically fast WGS reaction (reaction (1.8)), which is strongly dependent on the partial pressures of CO, H_2O, H_2, and CO_2 (p_{CO}, p_{H_2O}, p_{H_2} and p_{CO_2}, respectively). Therefore, the MMR within a Ni-based anode can be expressed as a set of the basic reactions (reactions (1.8)–(1.11)). If the carbon accumulation rate is negligible, the net consumption or production rates of CO_2, H_2O, and CO involved in the CH_4 conversion (r_{CO_2}, r_{H_2O} and r_{CO}, respectively) can be given by those of CH_4 and H_2 (r_{CH_4} and r_{H_2}, respectively) from the balance of chemical species as follows:

$$r_{CO_2} = 3r_{CH_4} + r_{H_2} \tag{3.1}$$

$$r_{H_2O} = -2r_{CH_4} - r_{H_2} \tag{3.2}$$

$$r_{CO} = -4r_{CH_4} - r_{H_2} \tag{3.3}$$

Negative and positive values signify net consumption and production rates, respectively. r_{CH_4} is always negative, while r_{H_2} is always positive. The thermal energy absorbed by the MMR process (ΔH_{MMR}) can be thermodynamically calculated as

$$\Delta H_{MMR} = \Delta H_{WGS} r_{WGS} + \Delta H_{CP} r_{CP} + \Delta H_{RB} r_{RB} + \Delta H_{CG} r_{CG} \tag{3.4}$$

where ΔH_{WGS}, ΔH_{CP}, ΔH_{RB}, and ΔH_{CG} are the enthalpy changes, and r_{WGS}, r_{CP}, r_{RB}, and r_{CG} are the net reaction rates of basic reactions (1.8), (1.9), (1.10) and (1.11), respectively, estimated as

$$r_{WGS} = \begin{cases} r_{CO_2} & ;\ r_{CO_2} > 0 \\ -r_{H_2O} & ;\ r_{H_2O} > 0 \\ 0 & ;\ r_{CO_2}, r_{H_2O} < 0 \end{cases} \tag{3.5}$$

$$r_{CP} = -r_{CH_4} \tag{3.6}$$

$$r_{RB} = \begin{cases} -r_{CO_2} & ;\ r_{CO_2} < 0 \\ 0 & ;\ r_{CO_2} > 0 \end{cases} \tag{3.7}$$

$$r_{CG} = \begin{cases} -r_{H_2O} & ;\ r_{H_2O} < 0 \\ 0 & ;\ r_{H_2O} > 0 \end{cases} \tag{3.8}$$

Consequently, the net kinetics of the MMR process can be estimated with a pair of r_{CH_4} and r_{H_2} values. The dependences of r_{CH_4} and r_{H_2} on temperature and gas

compositions were expressed in the following general form to consider the concurrent effects of CO_2 and H_2O. The calculation steps used to obtain r_{CH_4} and r_{H_2} are illustrated in Fig. 3.1.

$$r_X = interpolation\left(T, \left[r_X^{T_1}, .., r_X^{T_{N_T}}\right]\right) \tag{3.9}$$

where X is either CH_4 or H_2, T_i is the ith temperature, N_T is the number of T_i, and T is an arbitrary temperature within the temperature range between T_1 and T_{N_T}. '$interpolation(.)$' is the interpolating function determining r_X from the set of $\left[r_X^{T_1}, .., r_X^{T_{N_T}}\right]$ with respect to T (see Fig. 3.1-(a)).

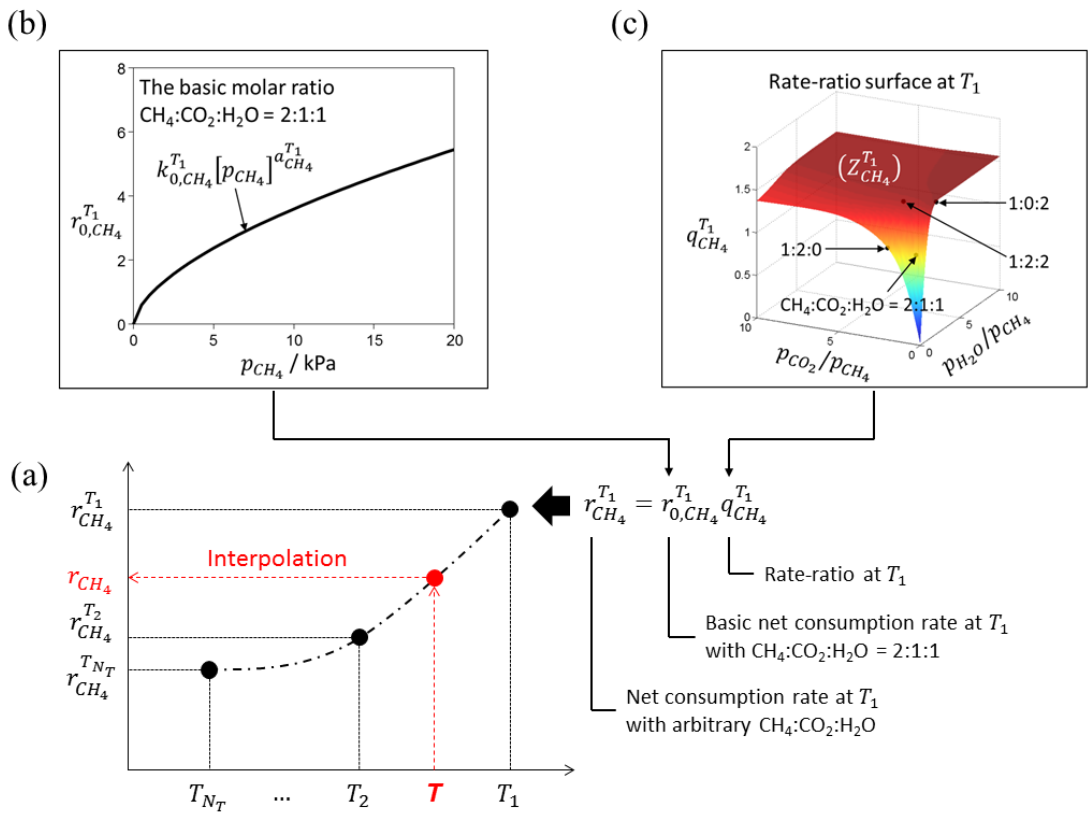

Fig. 3.1: Calculation flow to obtain the net consumption rate of CH_4 (r_{CH_4}) at arbitrary temperatures and gas compositions (CH_4-CO_2-H_2O-H_2-CO) in MMR.

The net consumption or production rate of X at T_i for an arbitrary gas composition, $r_X^{T_i}$, can be calculated using Eq. (3.10):

$$r_X^{T_i} = r_{0,X}^{T_i} q_X^{T_i} \tag{3.10}$$

where $r_{0,X}^{T_i}$ is the basic net consumption or production rate of X at T_i for the basic gas composition (partial pressures of CH_4, CO_2, H_2O, H_2, and CO are p_{CH_4}, p_{CO_2} (= 0.5 p_{CH_4}), p_{H_2O} (= 0.5 p_{CH_4}), p_{H_2} and p_{CO}, respectively, i.e. CH_4:CO_2:H_2O = 2:1:1), and $q_X^{T_i}$ is the rate-ratio of $r_X^{T_i}$ to $r_{0,X}^{T_i}$ at T_i. $r_{0,X}^{T_i}$ is expressed as a function of p_{CH_4} (see Fig. 3.1-(b)).

$$r_{0,X}^{T_i} = k_{0,X}^{T_i} \left[p_{CH_4}\right]^{a_{0,X}^{T_i}} \tag{3.11}$$

where $k_{0,X}^{T_i}$ and $a_{0,X}^{T_i}$ are the rate constant and power factor, respectively. $q_X^{T_i}$ can be expressed as a function of both p_{CO_2}/p_{CH_4} and p_{H_2O}/p_{CH_4} (see Fig. 3.1-(c)).

$$q_X^{T_i} = Z_X^{T_i}\left(p_{CO_2}/p_{CH_4}, p_{H_2O}/p_{CH_4}\right) \tag{3.12}$$

where $Z_X^{T_i}(.)$ is the function generating the surface of $q_X^{T_i}$, expressing the concurrent effects of CO_2 and H_2O on the MMR process at T_i. The p_{H_2} and p_{CO} have little influence on the CH_4 conversion in the internal reforming process [4, 7, 8]; therefore, they are neglected in calculation. Consequently, at each T_i, the net kinetics of the MMR is characterized by $k_{0,X}^{T_i}$, $a_{0,X}^{T_i}$, and $Z_X^{T_i}$.

Because the mathematical form of $Z_X^{T_i}$ is not clearly defined, and, more importantly, the correlation between $r_X^{T_i}$ and T is dependent on the gas composition, in this study, the flexible, non-linear ANN-based approximator and FIS-based interpolator were applied for $Z_X^{T_i}(.)$ and $interpolation(.)$, respectively, to build an empirical model calculating r_{CH_4} and r_{H_2} in the MMR (model outputs) from T, p_{CH_4}, p_{CO_2}, and p_{H_2O} (model inputs). The mathematical form of the approximator is:

$$\left[q_{CH_4}^{T_i}, q_{H_2}^{T_i}\right] = ANN^{T_i}\left(p_{CO_2}/p_{CH_4}, p_{H_2O}/p_{CH_4}\right). \tag{3.13}$$

(a)

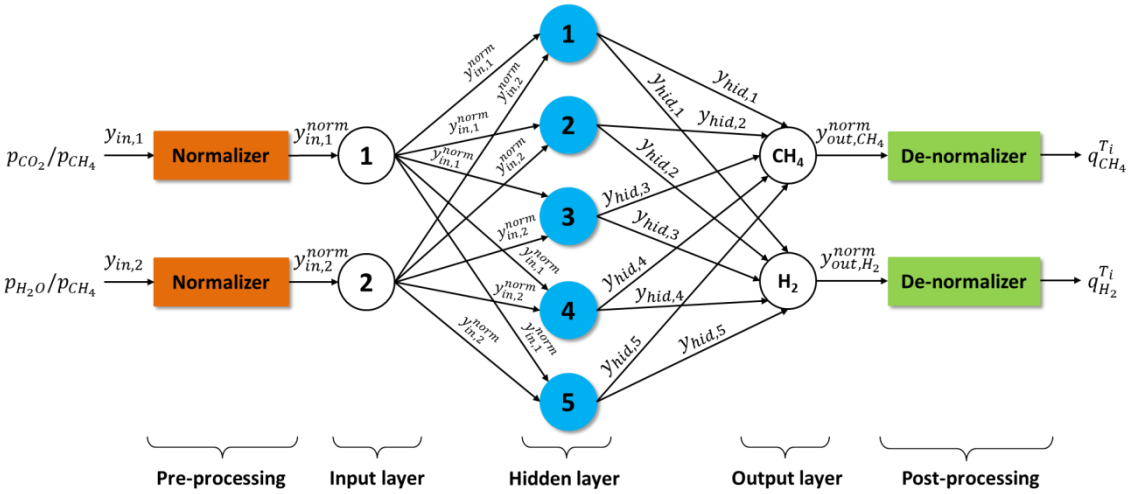

(b)

$$y_{hid,k} = tansig(U_{hid,k}) = \frac{2}{1+exp(-2U_{hid,k})} - 1$$

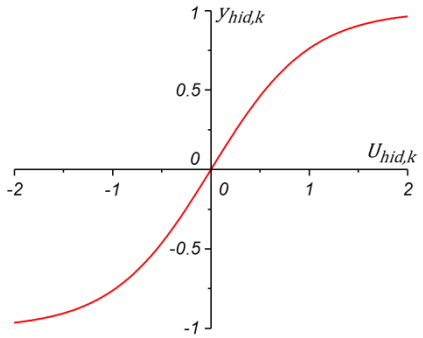

Fig. 3.2: Schematic illustration of ANN^{T_i} ($N_n = 5$) for generating $q_{CH_4}^{T_i}$ and $q_{H_2}^{T_i}$ at an arbitrary gas composition: (a) a schematic of the network, and (b) illustration of $tansig(.)$ function.

At each T_i, an ANN (denoted as ANN^{T_i}) is trained to generate both $Z_{CH_4}^{T_i}$ and $Z_{H_2}^{T_i}$ surfaces. ANN^{T_i}, schematically shown in Fig. 3.2-(a), is a feed-forward network composed of input (composed of two neurons: $y_{in,1}$ (= p_{CO_2}/p_{CH_4}) and $y_{in,2}$ (= p_{H_2O}/p_{CH_4})) and hidden (N_n neurons) and output (two neurons: $q_{CH_4}^{T_i}$ and $q_{H_2}^{T_i}$) layers. The mathematical expressions driving ANN^{T_i} are summarized below. The input values are normalized to range from –1 to 1 as follows:

$$y_{in,1}^{norm} = \left[y_{in,1} - \frac{1}{2}\left(y_{in,1,max} + y_{in,1,min}\right)\right]\left[\frac{1}{2}\left(y_{in,1,max} - y_{in,1,min}\right)\right]^{-1} \quad (3.14)$$

$$y_{in,2}^{norm} = \left[y_{in,2} - \frac{1}{2}\left(y_{in,2,max} + y_{in,2,max}\right)\right]\left[\frac{1}{2}\left(y_{in,2,max} - y_{in,2,max}\right)\right]^{-1} \quad (3.15)$$

where the subscripts max and min indicate the maximum and minimum values, respectively.

In ANN theory, signals processing mimics that of a biological neuron [9], the output signal produced from the kth hidden neuron, $y_{hid,k}$, is given by a nonlinear transform of $U_{hid,k}$, which is a linear combination of $y_{in,1}^{norm}$ and $y_{in,2}^{norm}$ with bias b_k.

$$y_{hid,k} = tansig\left(U_{hid,k}\right) = 2\left[1 + exp\left(-2U_{hid,k}\right)\right]^{-1} - 1 \quad (3.16)$$

$$U_{hid,k} = w_{k,1}y_{in,1}^{norm} + w_{k,2}y_{in,2}^{norm} + b_k. \quad (3.17)$$

Here, $w_{k,1}$ and $w_{k,2}$ are the weights of the kth hidden neuron. Among conventional transfer functions applicable to ANN, for approximation purposes, a continuous tan-sigmoid function ($tansig(.)$) (see Fig. 3.2-(b)) is commonly selected to maximize the smoothness of the network response. The nonlinear transform process for the output neurons can be omitted for simplicity. Therefore, the output signals of the output neurons, y_{out,CH_4}^{norm} and y_{out,H_2}^{norm}, which correspond to the rate-ratios of CH_4 consumption and H_2 production, respectively, are given by the linear combination of $y_{hid,k}$.

$$y_{out,CH_4}^{norm} = \sum_{k=1}^{N_n} w_{CH_4,k}y_{hid,k} + b_{CH_4} \quad (3.18)$$

$$y_{out,H_2}^{norm} = \sum_{k=1}^{N_n} w_{H_2,k}y_{hid,k} + b_{H_2} \quad (3.19)$$

where $w_{CH_4,k}$ and $w_{H_2,k}$ are the weights of the output neurons of CH_4 and H_2, respectively, for the kth hidden neuron, and b_{CH_4} and b_{H_2} are the biases of two output neurons. Both y_{out,CH_4}^{norm} and y_{out,H_2}^{norm} are normalized between –1 and 1, and $q_{CH_4}^{T_i}$ and $q_{H_2}^{T_i}$ are finally obtained through the de-normalizations of y_{out,CH_4}^{norm} and y_{out,H_2}^{norm}, respectively.

$$q_{CH_4}^{T_i} = y_{out,CH_4}^{norm}\left[\frac{1}{2}\left(q_{CH_4,max}^{T_i} - q_{CH_4,min}^{T_i}\right)\right] + \frac{1}{2}\left(q_{CH_4,max}^{T_i} + q_{CH_4,min}^{T_i}\right) \quad (3.20)$$

$$q_{H_2}^{T_i} = y_{out,H_2}^{norm}\left[\frac{1}{2}\left(q_{H_2,max}^{T_i} - q_{H_2,min}^{T_i}\right)\right] + \frac{1}{2}\left(q_{H_2,max}^{T_i} + q_{H_2,min}^{T_i}\right). \quad (3.21)$$

The number of hidden neurons, N_n, must be carefully selected to obtain good approximations of the $Z_{CH_4}^{T_i}$ and $Z_{H_2}^{T_i}$ surfaces. The connection weights ($w_{k,1}$, $w_{k,2}$, $w_{CH_4,k}$ and $w_{H_2,k}$) and biases (b_k, b_{CH_4} and b_{H_2}) of the network are determined through a training process based on input, $y_{in,1}$ and $y_{in,2}$, and corresponding output values, $q_{CH_4}^{T_i}$ and $q_{H_2}^{T_i}$, derived from experimental MMR kinetic data. In the present approach, r_{CH_4} and r_{H_2} at an arbitrary temperature T are determined from the set of $\left[r_{CH_4}^{T_1},..,r_{CH_4}^{T_{N_T}}\right]$ and $\left[r_{H_2}^{T_1},..,r_{H_2}^{T_{N_T}}\right]$, respectively, using the FIS-based interpolator, as shown in Eq. (3.22). This calculation procedure includes the fuzzification, processing, and defuzzification steps, as illustrated in Fig. 3.3.

$$\left[r_{CH_4},r_{H_2}\right]=FIS\left(T,\left[r_{CH_4}^{T_1},..,r_{CH_4}^{T_{N_T}}\right],\left[r_{H_2}^{T_1},..,r_{H_2}^{T_{N_T}}\right]\right) \tag{3.22}$$

The temperature range between T_1 and T_{N_T} is divided into N_T temperature levels, $Level_{T_i}$ ($i=1..N_T$). Each temperature level is centered at T_i and characterized by a triangular fuzzy set, denoted $L_{T_i}^f$, expressing the possibility of $T\in Level_{T_i}$ (or the partial truth of $T=T_i$). As shown in Fig. 3.3, in the fuzzification step, the value of T is mapped into $L_{T_i}^f$ to have corresponding fuzzy value $\mu_{T_i}(T)$ ($0\le\mu_{T_i}(T)\le 1$). $\mu_{T_i}(T)=1$, so T is equal to T_i, while $\mu_{T_i}(T)=0$ implies that T is not T_i, and $0<\mu_{T_i}(T)<1$ indicates that $T=T_i$ is partially true. In the processing step, values of r_{CH_4} and r_{H_2} associated with each $Level_{T_i}$ are inferred from the following fuzzy rule,

$$IF\left(T\in Level_{T_i}\right)THEN\left(r_{CH_4}=r_{CH_4}^{T_i}\right)and\left(r_{H_2}=r_{H_2}^{T_i}\right). \tag{3.23}$$

r_{CH_4} and r_{H_2} are computed in the defuzzification step as the weighted averages of the $IF-THEN$ rule outputs (Eqs. (3.24) and (3.25), respectively). μ_{T_i} is thus regarded as the temperature dependent coefficient of the interpolation.

$$r_{CH_4}=\left[\sum_{i=1}^{N_T}\mu_{T_i}(T)r_{CH_4}^{T_i}\right]\left[\sum_{i=1}^{N_T}\mu_{T_i}(T)\right]^{-1} \tag{3.24}$$

$$r_{H_2}=\left[\sum_{i=1}^{N_T}\mu_{T_i}(T)r_{H_2}^{T_i}\right]\left[\sum_{i=1}^{N_T}\mu_{T_i}(T)\right]^{-1} \tag{3.25}$$

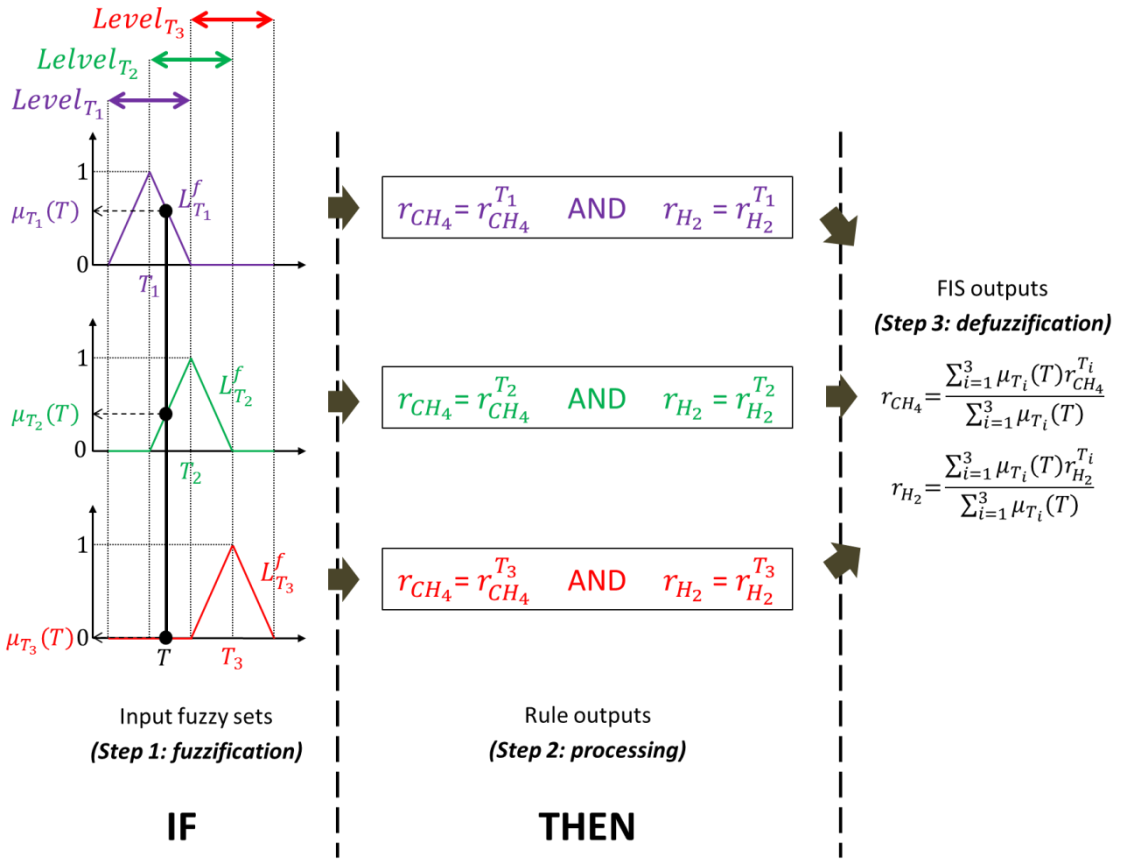

Fig. 3.3: Schematic illustration of the interpolating process to determine the net consumption rate of CH_4 (r_{CH_4}) from the set of $\left[r^{T_1}_{CH_4}, r^{T_2}_{CH_4}, r^{T_3}_{CH_4}\right]$ and the net production rate of H_2 (r_{H_2}) from the $\left[r^{T_1}_{H_2}, r^{T_2}_{H_2}, r^{T_3}_{H_2}\right]$ set at an arbitrary temperature (T) between T_1 and T_3 by FIS.

3.2 Determination of model parameters

In the present approach, the temperature dependence of the MMR kinetics is determined by interpolation using the reaction rates measured for N_T temperature values (T_i) in a pre-defined temperature range between T_1 and T_{N_T}. The accuracy can be improved by properly selecting N_T and the distribution of T_i in the defined range. In this study, $N_T = 3$ and T_i = 700, 750, and 800 °C were selected, and, at these temperatures, CH_4 reforming tests were performed using a button-type SOFC single cell. Subsequently, data processing was carried out to determine $k^{T_i}_{0,CH_4}$, $a^{T_i}_{0,CH_4}$, $k^{T_i}_{0,H_2}$, and

$a_{0,H_2}^{T_i}$ through power-law fitting (Step-I) and $Z_{CH_4}^{T_i}$ and $Z_{H_2}^{T_i}$ through ANN^{T_i} training (Step-II).

3.2.1 Experiments

3.2.1.1 Experimental setup

An anode-supported half-cell based on the porous Ni-8YSZ (NiO:8YSZ (8 mol% Y_2O_3-ZrO_2) = 56 wt%:44 wt%) with a diameter of 20 mm, a thickness of 870 μm, and a porosity of about 32% provided by Saga Ceramic Research Laboratory was used for CH_4 reforming experiments. The half-cell was sandwiched between two alumina rings, and subsequently, a ceramic bonding agent (Aron Ceramic, TOAGOSEI Co. Ltd.) was pasted around inner and outer perimeters of the cell to make it gastight (see Fig. 3.4-(a)). Then, as shown in Fig. 3.4-(b), the half-cell was mounted on the top of the outer alumina tube using ceramic paste, so that the gastight electrolyte and reforming catalysts (here, the porous anode support) became the outside and inside of the cell, respectively.

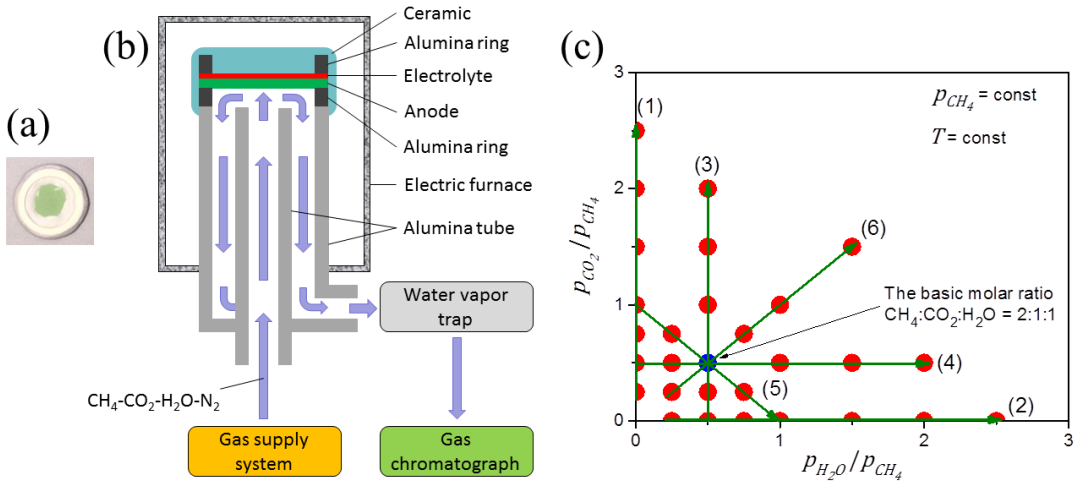

Fig. 3.4: CH_4 reforming tests using a Ni-8YSZ anode-supported half-cell (20 mm in diameter): (a) a picture of the catalyst material (anode side), (b) schematic drawing of the experimental setup, and (c) the experimental matrix showing six testing programs indicated by green arrows. CH_4 reforming tests were performed for the compositions, as indicated by the blue (basic molar ratio) and red dots.

After heating to 900 °C in 4.5 h in an electric furnace, a 100 mL min^{-1} flow of pure N_2 was supplied through the inner alumina tube to purge the anode compartment. After 30 min purging, the anode gas was switched from pure N_2 to a 100 mL min^{-1} flow of pure H_2 (dry), and this reducing atmosphere was maintained for 2.5 h to form a Ni metal catalyst. After the reduction treatment, the gas stream was switched to a 100 mL min^{-1} flow of H_2/N_2 = 10/90, and the temperature was reduced to the testing temperature (700, 750, or 800 °C).

3.2.1.2 Experimental procedure

In Step-I, the consumption or production rate of X (CH_4 or H_2), $r_{0,X}^{T_i}$, was measured at p_{CH_4} values of 6, 9, 12, 15, and 18 kPa with a constant partial pressure ratio of p_{CO_2} = p_{H_2O} = 0.5p_{CH_4} (CH_4:CO_2:H_2O = 2:1:1). In Step-II, to determine $Z_X^{T_i}$, both CO_2 and H_2O were varied at a constant p_{CH_4} of 12 kPa along the six testing programs shown in Fig. 3.4-(c): program 1: CO_2 dependence without H_2O (reforming agent in the fuel is CO_2 only), program 2: H_2O dependence without CO_2 (reforming agent in the fuel is H_2O only), program 3: CO_2 dependence at p_{H_2O}/p_{CH_4} = 0.5, program 4: H_2O dependence at p_{CO_2}/p_{CH_4} = 0.5, program 5: shifting from dry to steam reforming, and program 6: MMR with p_{CO_2} = p_{H_2O}.

For each fuel composition, after the porous anode was exposed to the fuel stream for 1 h, off-gas analysis was carried out. Before moving to the next testing program, the fuel stream was switched to a 100 mL min^{-1} flow of 12% humidified H_2 to remove carbonaceous species deposited on the Ni surface. After this treatment for 8–10 h, the anode compartment was purged with a 100 mL min^{-1} flow of H_2/N_2 = 10/90 for 1 h to remove steam. Catalyst degradation was periodically checked by carrying out reforming tests with a flow gas composition of CH_4:CO_2:H_2O = 2:1:1.

3.2.2 Data post-processing

Several studies on the reaction kinetics of dry and steam reforming of CH_4 for Ni-loaded catalysts have reported that CH_4 conversion is not composition dependent when

p_{CO_2}/p_{CH_4} and p_{H_2O}/p_{CH_4} are greater than two [3, 10–12]. The experimental matrix in this study to measure $r_{CH_4}^{T_i}$ and $r_{H_2}^{T_i}$ covers p_{CO_2}/p_{CH_4} and p_{H_2O}/p_{CH_4} ranges up to 2.5, and when either p_{CO_2}/p_{CH_4} or p_{H_2O}/p_{CH_4} (or both) exceeded 2.5, $r_{CH_4}^{T_i}$ and $r_{H_2}^{T_i}$ were determined by extrapolation using a power-law. The experimentally obtained rate ratios, $q_X^{T_i}$, were assigned to the output values of ANN^{T_i}. A wide range of fuel compositions can be covered by this approach with a minimum number of experiments.

Table 3.1: Parameters determined by power-law fitting and ANN training to describe MMR.

Parameters	T = 700 °C	T = 750 °C	T = 800 °C
$\begin{bmatrix} k_{0,CH_4} & a_{0,CH_4} \\ k_{0,H_2} & a_{0,H_2} \end{bmatrix}$	$\begin{bmatrix} -0.783 & 0.6 \\ 2.066 & 0.6 \end{bmatrix}$	$\begin{bmatrix} -0.649 & 0.7517 \\ 1.703 & 0.7517 \end{bmatrix}$	$\begin{bmatrix} -0.597 & 0.8692 \\ 1.525 & 0.8692 \end{bmatrix}$
$\begin{bmatrix} z_{1,min} & z_{1,max} \\ z_{2,min} & z_{2,max} \end{bmatrix}$	$\begin{bmatrix} 0 & 8.266 \\ 0 & 8.209 \end{bmatrix}$	$\begin{bmatrix} 0 & 8.266 \\ 0 & 8.209 \end{bmatrix}$	$\begin{bmatrix} 0 & 8.266 \\ 0 & 8.209 \end{bmatrix}$
$\begin{bmatrix} q_{CH_4,min} & q_{CH_4,max} \\ q_{H_2,min} & q_{H_2,max} \end{bmatrix}$	$\begin{bmatrix} 0 & 1.587 \\ 0 & 2.238 \end{bmatrix}$	$\begin{bmatrix} 0 & 1.587 \\ 0 & 2.238 \end{bmatrix}$	$\begin{bmatrix} 0 & 1.587 \\ 0 & 2.238 \end{bmatrix}$
$\begin{bmatrix} w_{1,1} & w_{1,2} \\ w_{2,1} & w_{2,2} \\ w_{3,1} & w_{3,2} \\ w_{4,1} & w_{4,2} \\ w_{5,1} & w_{5,2} \end{bmatrix}$	$\begin{bmatrix} 2.779 & -0.566 \\ 0.569 & -1.909 \\ -1.721 & 0.076 \\ -2.453 & -2.974 \\ 1.91 & 2.926 \end{bmatrix}$	$\begin{bmatrix} 1.607 & 0.005 \\ 0.109 & -1.386 \\ -1.445 & 0.089 \\ -3.13 & -4.959 \\ 3.163 & 5.223 \end{bmatrix}$	$\begin{bmatrix} 2.499 & -0.155 \\ 0.189 & -1.979 \\ -1.445 & 0.09 \\ -3.736 & -5.615 \\ 3.838 & 5.68 \end{bmatrix}$
$\begin{bmatrix} b_1 \\ b_2 \\ b_3 \\ b_4 \\ b_5 \end{bmatrix}$	$\begin{bmatrix} 2.089 \\ -1.672 \\ -6.713 \\ -4.726 \\ 4.694 \end{bmatrix}$	$\begin{bmatrix} 1.825 \\ -1.673 \\ -6.932 \\ -7.086 \\ 7.573 \end{bmatrix}$	$\begin{bmatrix} 2.057 \\ -2.364 \\ -6.932 \\ -8.386 \\ 8.759 \end{bmatrix}$
$\begin{bmatrix} w_{CH_4,1} & w_{H_2,1} \\ w_{CH_4,2} & w_{H_2,2} \\ w_{CH_4,3} & w_{H_2,3} \\ w_{CH_4,4} & w_{H_2,4} \\ w_{CH_4,5} & w_{H_2,5} \end{bmatrix}$	$\begin{bmatrix} -0.02 & -0.197 \\ -0.11 & -0.86 \\ 0.663 & 0.378 \\ 1.466 & 1.036 \\ 3.682 & 2.556 \end{bmatrix}$	$\begin{bmatrix} -0.069 & -0.625 \\ 0.066 & -0.86 \\ 0.0006 & 0.01 \\ 2.281 & 1.618 \\ 3.401 & 2.385 \end{bmatrix}$	$\begin{bmatrix} -0.066 & -0.344 \\ 0.034 & -0.69 \\ 0.105 & 0.183 \\ 2.446 & 1.62 \\ 3.451 & 2.32 \end{bmatrix}$
$\begin{bmatrix} b_{CH_4} \\ b_{H_2} \end{bmatrix}$	$\begin{bmatrix} -0.718 \\ -1.179 \end{bmatrix}$	$\begin{bmatrix} -0.409 \\ -0.804 \end{bmatrix}$	$\begin{bmatrix} -0.514 \\ -0.977 \end{bmatrix}$

At all tested fuel compositions, the amounts of carbon-based gaseous species at the inlet and outlet were almost balanced (the average deviation was found to be less than 5%), suggesting that the carbon accumulation rate is slow, and the influence of coking

on the MMR is negligible under the conditions selected in this study. Parameters involved in the present approach were determined using a power-law fitting and ANN training process using MATLAB code, and these values are listed in Table 3.1.

As shown in Fig. 3.5-(a), at the basic molar ratio (CH_4:CO_2:H_2O = 2:1:1), both r_{0,CH_4}^{700} and r_{0,H_2}^{700} could be expressed by a power-law function of p_{CH_4}, as indicated in the general empirical MMR expression (Eq. (3.11)). The results of Fig. 3.5 indicate that the calculated $r_{CH_4}^{700}$ and $r_{H_2}^{700}$ using the parameters of Table 3.1 can reproduce the experimental values with the coefficients of determination (R^2) greater than 0.98, indicating that these parameters describe the complex MMR reaction well.

As shown in Figs. 3.5-(b), (c), (d), and (e), which correspond to programs 1, 2, 3, and 4, respectively, at p_{CH_4} = 12 kPa, the dependences of $r_{CH_4}^{700}$ on p_{CO_2} and p_{H_2O} were weak above p_{CO_2} and p_{H_2O} values of about 24 kPa, i.e. p_{CO_2}/p_{CH_4} and p_{H_2O}/p_{CH_4} > 2. At the same time, in programs 1 and 3, suppression of $r_{H_2}^{700}$ was initiated because of its promotion of the reverse WGS-reaction. In contrast, in programs 2 and 4, $r_{H_2}^{700}$ was slightly increased by the forward-WGS reaction.

The slope of $r_{CH_4}^{700}$ in the range of p_{H_2O}/p_{CH_4} < 2 in program 2 (where the only reforming agent in the fuel is H_2O) compared to that in the range of p_{CO_2}/p_{CH_4} < 2 in program 1 (where the only reforming agent in the fuel is CO_2) is steeper. Moreover, the value of $r_{CH_4}^{700}$ at saturation in program 2 was greater than that in program 1, reflecting the faster kinetics of steam reforming compared to dry reforming. Similarly, CH_4 consumption was promoted as p_{H_2O} increased (program 4) to a greater extent than as p_{CO_2}increased (program 3) in the presence of CO_2 and H_2O, respectively, at 6 kPa in the fuel stream. The profile of $r_{CH_4}^{700}$ as a function of (p_{CO_2} + p_{H_2O}) under p_{CO_2} = p_{H_2O} (program 6) was found to be closer to that of program 2 than that of program 1 because of the larger contribution from steam reforming.

For the partial replacement of CO_2 with H_2O under the constant total pressure and $p_{CO_2} + p_{H_2O} = p_{CH_4}$ (program 5, Fig. 3.5-(f)), $r_{CH_4}^{700}$ varied linearly with p_{H_2O} (or p_{CO_2}). Therefore, when $p_{CO_2} + p_{H_2O} = p_{CH_4}$, MMR can be regarded as a linear combination of dry and steam reforming reactions.

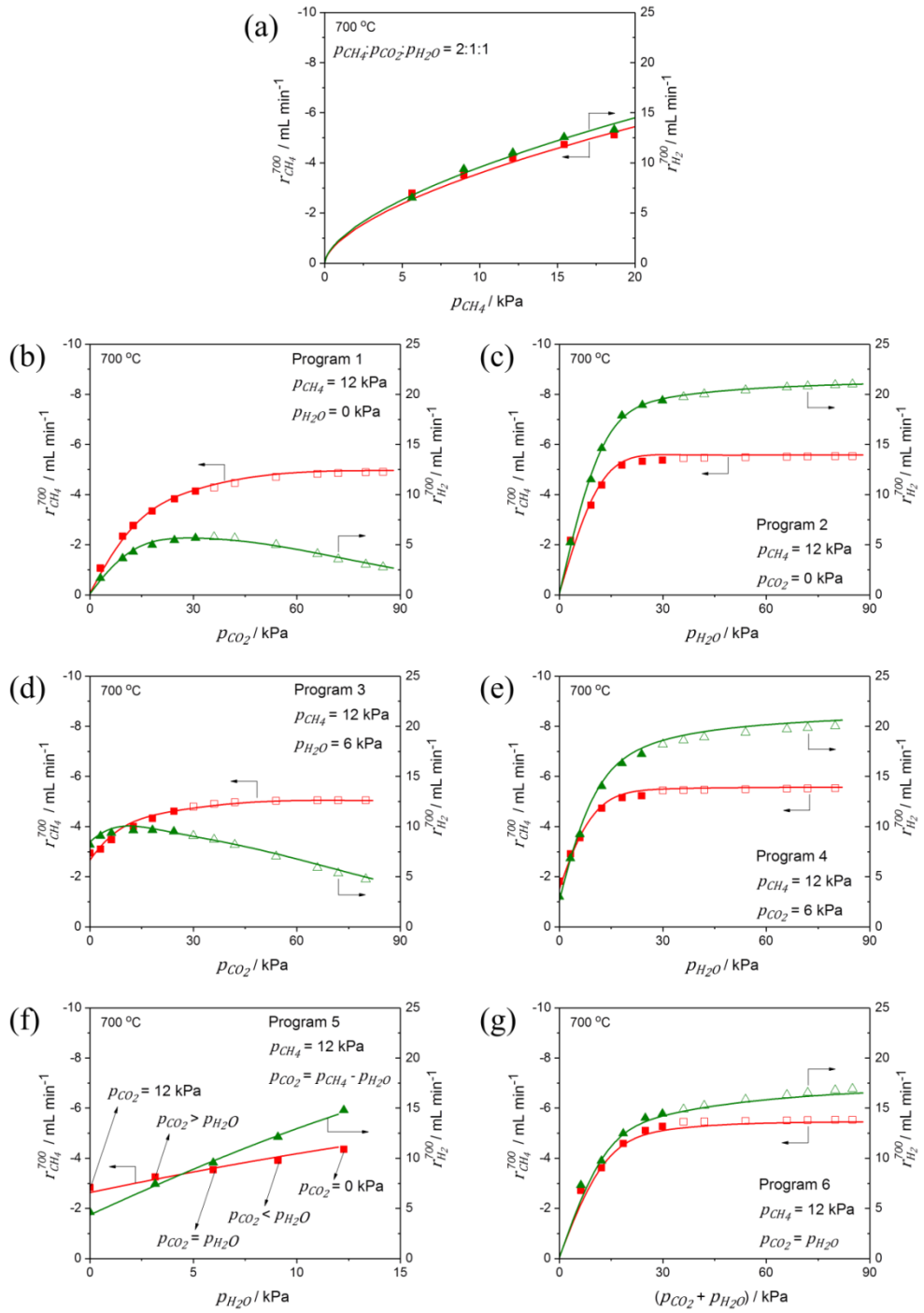

Fig. 3.5: Net reaction rates of MMR within the porous Ni-YSZ anode material at 700 °C for a fuel flow rate of 100 mL min^{-1} (fuel is the CH_4-CO_2-H_2O-N_2 mixture). (a): The profile of $r_{0,X}^{700}$ as a function of p_{CH_4} obtained in Step-I. (b–g): Profiles of r_X^{700} as a function of p_{CO_2} or p_{H_2O} obtained in Step-II. ■ and ▲ are measured $r_{CH_4}^{700}$ and $r_{H_2}^{700}$, respectively. □ and △ are $r_{CH_4}^{700}$ and $r_{H_2}^{700}$ estimated from the experimental trends by extrapolation using a power law. Solid lines are the net reaction rates predicted by the black-box model using ANN^{700}; for (a) a power function was applied.

The concurrent effect of CO_2 and H_2O in the MMR can be shown by the continuum surfaces of the rate ratios, $Z_{CH_4}^{700}$ and $Z_{H_2}^{700}$, generated by ANN^{700} (see Figs. 3.6-(a) and (b)). The estimated net rates based on this ANN^{700} well matched the measured values in all programs, as shown in Figs. 3.5-(b–g).

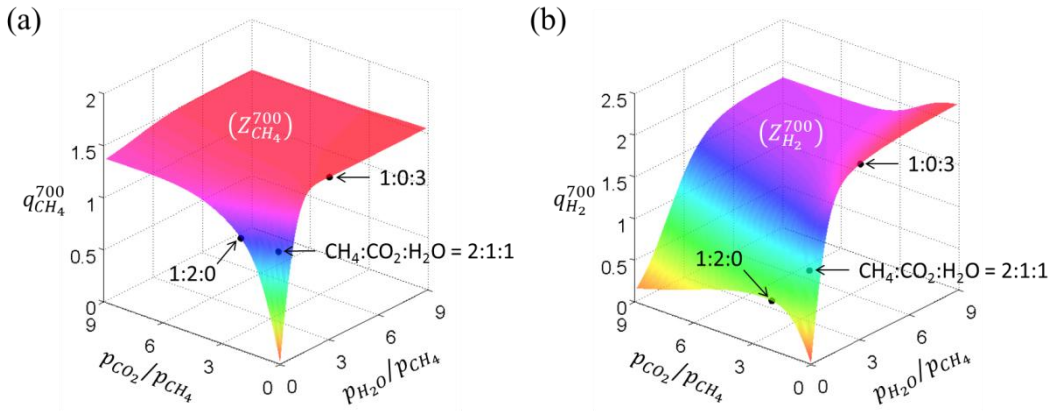

Fig. 3.6: The rate ratio surfaces of (a) CH_4 and (b) H_2 generated by ANN^{700}, characterizing the concurrent effects of CO_2 and H_2O in the MMR within the porous Ni-YSZ anode material at 700 °C.

Similar reforming tendencies were also obtained at 750 and 800 °C as shown in Figs. 3.7 and 3.8, respectively. The surfaces of the rate ratios at 750 and 800 °C are shown in Fig. 3.9 and 3.10, respectively.

Comparing Figs. 3.5, 3.7 and 3.8, temperature dependence of reforming kinetics was apparent. At the basic molar ratio (CH_4:CO_2:H_2O = 2:1:1), the slopes of $r_{CH_4}^{T_i}$ and $r_{H_2}^{T_i}$ increased with increasing T_i (compare Figs. 3.5-(a), 3.7-(a) and 3.8-(a)), reflecting the thermally activated CH_4 pyrolysis.

As shown in Figs. 3.5-(b), 3.7-(b) and 3.8-(b), corresponding to program 1 (where the only reforming agent in the fuel is CO_2), the slope of $r_{CH_4}^{T_i}$ in the range of p_{CO_2}/p_{CH_4} < 2 became steeper as T_i varied from 700 to 800 °C, indicating that p_{CO_2} dependency of $r_{CH_4}^{T_i}$ became stronger at higher temperature; hence, $r_{CH_4}^{T_i}$ more quickly reached to the maximum, followed by the region insusceptible to p_{CO_2}. The maximum $r_{CH_4}^{T_i}$ increased slightly with increase of T_i. It could be said that in the temperature range of 700–800 °C,

the kinetics of dry reforming in Ni-YSZ anodes was strongly dependent on p_{CO_2} and temperature for p_{CO_2}/p_{CH_4} < 2, whereas less sensitive to p_{CO_2} and temperature for p_{CO_2}/p_{CH_4} > 2. The profile of $r_{CH_4}^{T_i}$ in program 2 (where the only reforming agent in the fuel is H_2O) showed similar trends (see Figs. 3.5-(c), 3.7-(c) and 3.8-(c)). These reforming characteristics reflected the dependencies on temperature and gas composition of the Arrhenius behaviors of dry and steam reforming of CH_4 over Ni-based catalysts [4]. This emphasizes that the kinetics of each reforming process cannot be expressed by a single model for arbitrary temperatures and gas compositions using conventional approaches, moreover, the MMR cannot be considered as the sum of dry and steam reforming, and any calculations adopting this assumption may result in overestimations [13, 14]. Therefore, the ANN/FIS-based model developed in this study is very effective to express the complex kinetics of MMR, especially applicable temperature range can easily be extended by adding appropriate ANN^{T_i}s.

In the range of $(p_{CO_2} + p_{H_2O})/p_{CH_4}$ > 2 under $p_{CO_2} = p_{H_2O}$ (program 6) (see Figs. 3.5-(g) and 3.8-(g)), $r_{H_2}^{700}$ increased while $r_{H_2}^{800}$ decreased with respect to $(p_{CO_2} + p_{H_2O})/p_{CH_4}$, denoting that WGS reaction was thermodynamically shifted to reverse direction with increasing temperature.

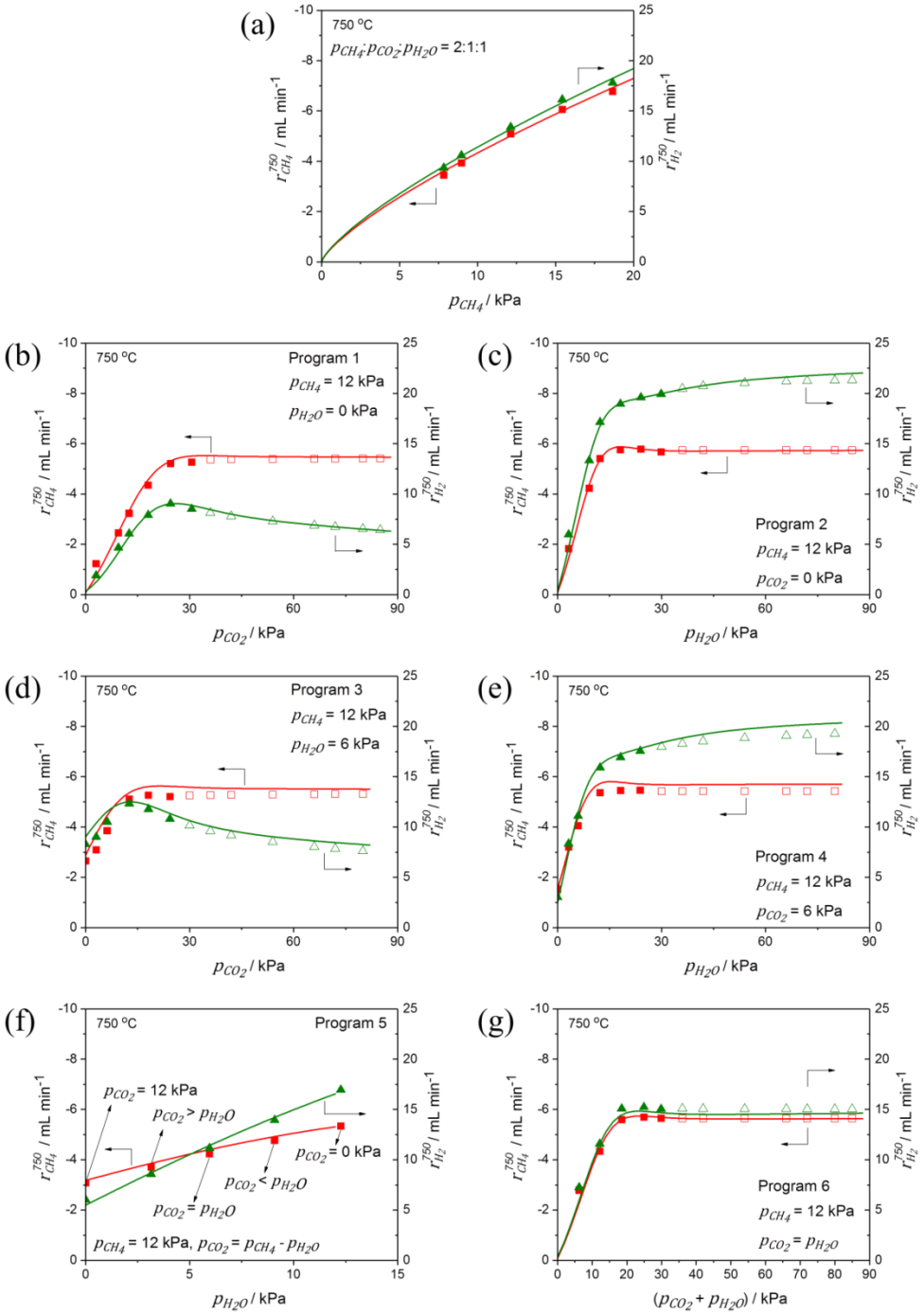

Fig. 3.7: Net reaction rates of MMR within the porous Ni-YSZ anode material at 750 °C for a fuel flow rate of 100 mL min^{-1} (fuel is the CH_4-CO_2-H_2O-N_2 mixture). (a): The profile of $r_{0,X}^{750}$ as a function of p_{CH_4} obtained in Step-I. (b–g): Profiles of r_X^{750} as a function of p_{CO_2} or p_{H_2O} obtained in Step-II. ■ and ▲ are measured $r_{CH_4}^{750}$ and $r_{H_2}^{750}$, respectively. □ and △ are $r_{CH_4}^{750}$ and $r_{H_2}^{750}$ estimated from the experimental trends by extrapolation using a power law. Solid lines are the net reaction rates predicted by the black-box model using ANN^{750}; for (a) a power function was applied.

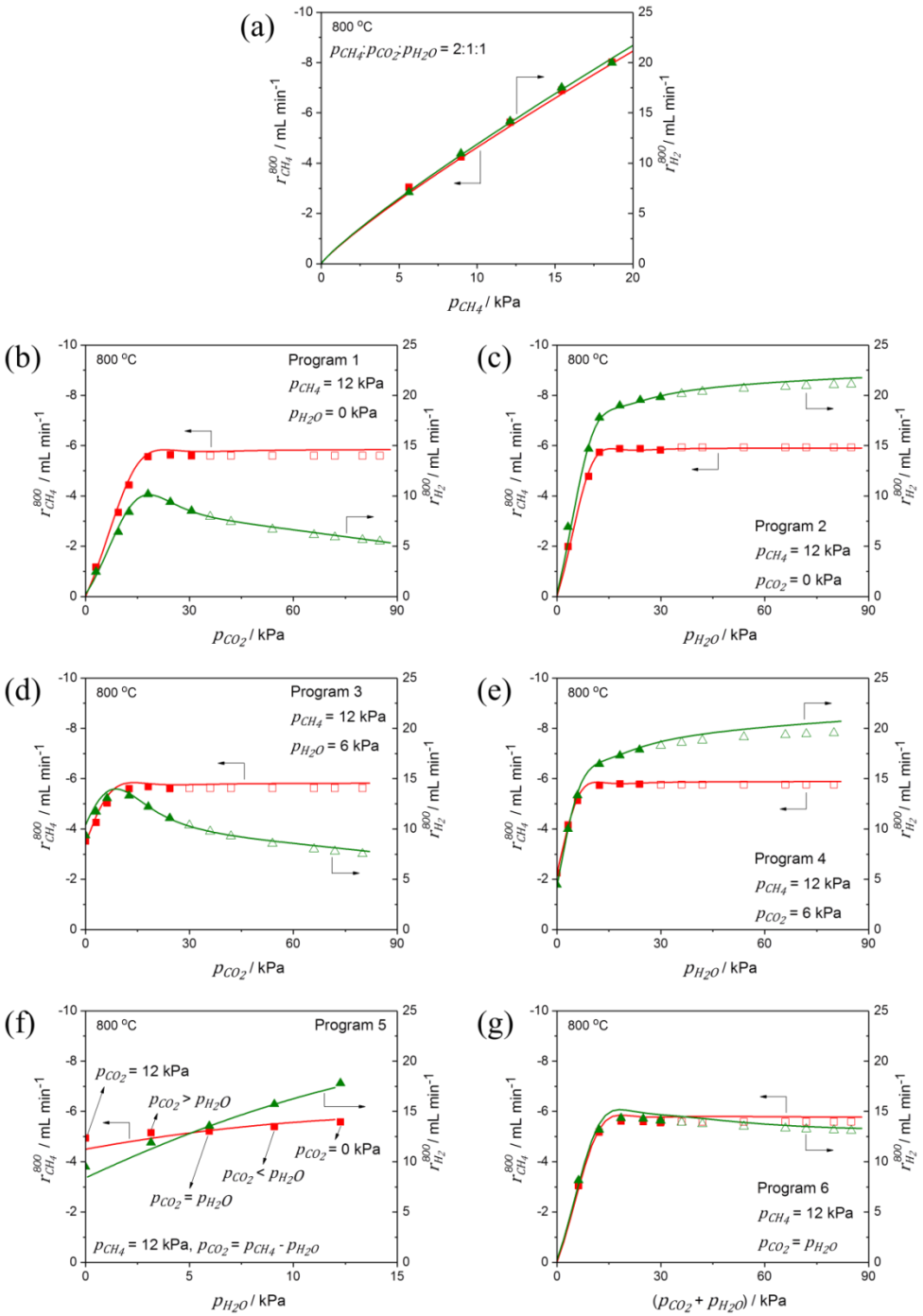

Fig. 3.8: Net reaction rates of MMR within the porous Ni-YSZ anode material at 800 °C for a fuel flow rate of 100 mL min^{-1} (fuel is the CH_4-CO_2-H_2O-N_2 mixture). (a): The profile of $r_{0,X}^{800}$ as a function of p_{CH_4} obtained in Step-I. (b–g): Profiles of r_X^{800} as a function of p_{CO_2} or p_{H_2O} obtained in Step-II. ■ and ▲ are measured $r_{CH_4}^{800}$ and $r_{H_2}^{800}$, respectively. □ and △ are $r_{CH_4}^{800}$ and $r_{H_2}^{800}$ estimated from the experimental trends by extrapolation using a power law. Solid lines are the net reaction rates predicted by the black-box model using ANN^{800}; for (a) a power function was applied.

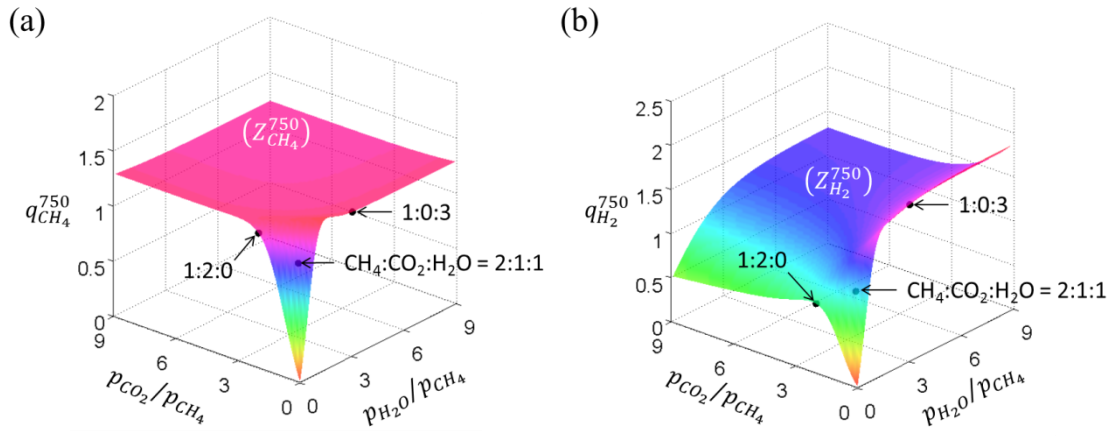

Fig. 3.9: The rate ratio surfaces of (a) CH_4 and (b) H_2 generated by ANN^{750}, characterizing the concurrent effects of CO_2 and H_2O in the MMR within the porous Ni-YSZ anode material at 750 °C.

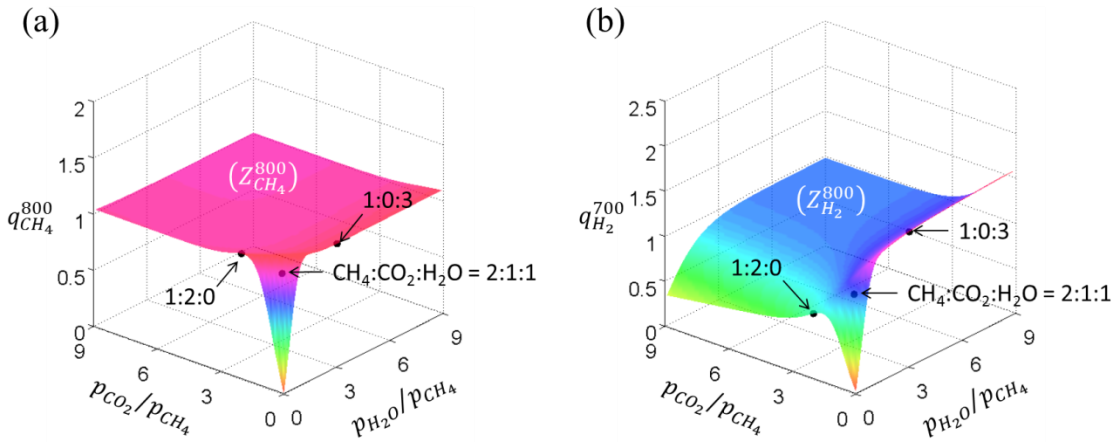

Fig. 3.10: The rate ratio surfaces of (a) CH_4 and (b) H_2 generated by ANN^{800}, characterizing the concurrent effects of CO_2 and H_2O in the MMR within the porous Ni-YSZ anode material at 800 °C.

3.3 Model validation

Validity check of the ANN/FIS-based MMR model was carried out for the measured temperature drop caused by CH_4 dry reforming in a planar-type paper-structured catalyst (PSC) reformer reported in Ref. [15] with the dimension of 50 × 50 × 1.5 mm^3, and porosity and pore diameter of about 90 % and 20 μm, respectively, (see Fig. 3.11-

(a)) was mounted in an alumina housing as shown in Fig. 3.11-(b). A 240 μm-thick YSZ plate was placed on the top of the PSC to separate fuel and air simulating SOFC configuration, and ceramic bond was pasted around the outer perimeter for gas sealing (see Fig. 3.11-(c)). After heating to the testing temperature of 800 ^{o}C, 180 mL min^{-1} simulated biogas (CH_4/CO_2 = 1) was supplied to the PSC, corresponding to a GHSV of 2880 h^{-1}. Temperature distribution caused by CH_4 dry reforming within the area of 40 x 40 mm^2 was captured from the electrolyte side by an infrared camera (Mikron MCS640/IS, LumaSense Technologies Inc., USA). The dry-basis of off-gas was analysed by an automatic gas chromatograph (GC-20B, Shimadzu, Japan).

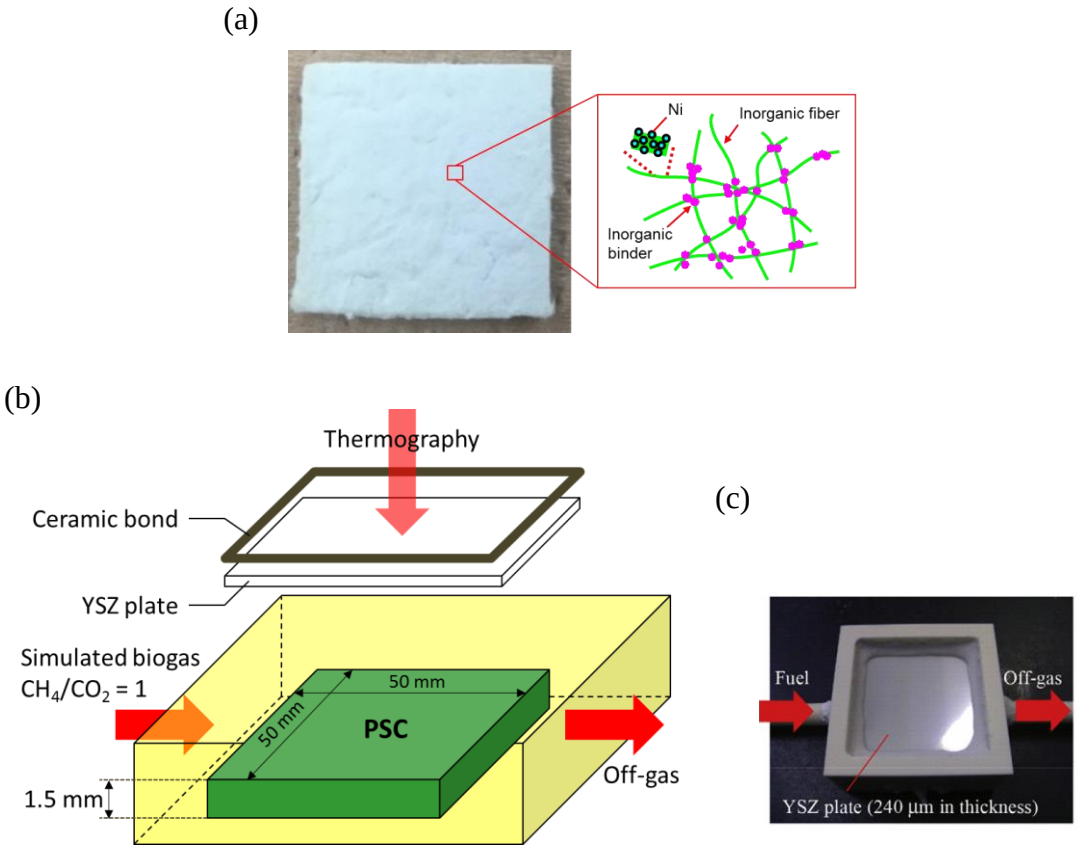

Fig. 3.11: PSC-based planar-type reactor simulating SOFC configuration (visualization system of reforming reaction using infrared camera) [15]: (a) structure of paper-structured catalyst (PSC), (b) schematic illustration and (c) photograph of the test bench.

As shown in Fig. 3.12, a CFD model of the planar-type PSC reformer consisted of three computational domains, PSC, YSZ plate and air channel, was fabricated. The PSC

material was assumed to be homogeneous and isotropic. Its physical parameters are listed in Table 3.2. Details on the CFD model will be described in Chapter 4. Calculation was carried out for the condition of Table 3.3.

Because the ANN/FIS-based MMR model was derived from the catalytic behavior of Ni-8YSZ anode substrate, net consumption and production rates of gaseous species involved in CH_4 conversion calculated by this model, r_X (X = CH_4, CO_2, H_2O, H_2 and CO), were corrected to compensate the difference in catalytically-active surface area between the anode and the PSC as follows,

$$r_{X,cor} = k_{cor} r_X \tag{3.26}$$

,where $r_{X,cor}$ is the corrected net consumption or production rate of X, and k_{cor} is the correction factor determined so that the maximum temperature drop on the YSZ plate in the experiment could be reproduced.

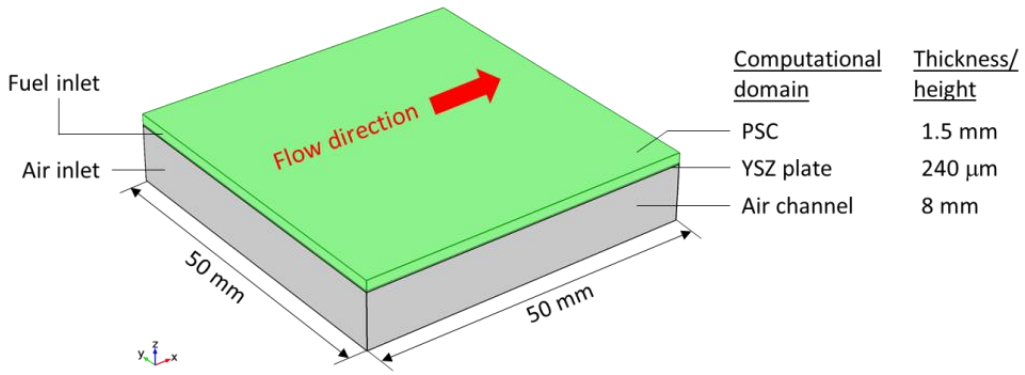

Fig. 3.12: 3D-CFD model of the planar-type PSC reformer.

Table 3.2: Physical properties of the PSC.

Porosity (ε_{PSC}) / -	0.9 [15]
Density (ρ_e) / kg m^{-3}	2500
Specific heat capacity ($C_{p,c}$) / J kg^{-1} K^{-1}	1050 [16]
Thermal conductivity (k_{PSC}) / W m^{-1} K^{-1}	1.6 [15]

Table 3.3: Operating condition.

Fuel (inlet)	
Temperature / °C	800
Fuel composition / %	CH_4: 50, CO_2: 50
Velocity / m s^{-1}	0.144
Air (inlet)	
Temperature / °C	800
Air composition / %	O_2: 21, N_2: 79
Velocity / m s^{-1}	0.144

Measured and calculated temperature profiles ($\Delta T = T$ – 800 ^{o}C) are compared in Fig. 3.13. In the experiment, total CH_4 conversion (χ_{CH_4}) was about 91 %. CH_4 was rapidly converted to syngas within the inlet region, leading to a maximum temperature drop (ΔT_{max}) of about –88 ^{o}C at 6 mm from the inlet (blue). Further downstream, the rate of CH_4 reforming was reduced due to decreases in the concentrations of CH_4 and CO_2, and thus ΔT was lessened. At 25 mm from the inlet, ΔT approached zero, indicating that the local syngas production rate was nearly zero. By adjusting k_{cor} to obtain the same ΔT_{max}, calculated profile of ΔT along fuel flow direction (red) was well-matched with the experimental result. ΔT_{max} was estimated to occur at about 4 mm from the inlet corresponding to χ_{CH_4} of 96%.

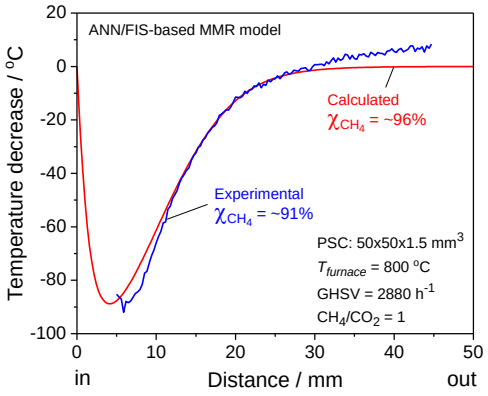

Fig. 3.13: Temperature profile in the planar-type PSC reformer during CH_4 dry reforming at GHSV of 2880 h^{-1}. Blue line is the measured profile [13]. Red line is the calculated one using the MMR-model-incorporated CFD. χ_{CH_4} indicates the total CH_4 conversion rate.

The consistency of the profile estimated by MMR-incorporated CFD model with experimental one for the planar-type PSC reformer proves that the ANN/FIS-based MMR model is applicable for different types of Ni-based catalysts by selecting appropriate k_{cor}.

3.4 Conclusions

Expressing the simultaneous contribution of CH_4 dry and steam reforming (methane multiple-reforming (MMR)) in Ni-based anodes is of great importance in numerical works on DIR-SOFCs operating with biogas. Due to its complex kinetics strongly dependent on gas composition and temperature, MMR could not be fully modeled by conventional approaches based on power-law model fitting, first order reaction kinetics related to CH_4 partial pressure and Langmuir-Hinshelwood kinetics. Therefore, the contribution of dry reforming in syngas production has commonly been ignored in the calculations of consumption and production rates of gaseous species involved in the catalytic CH_4 conversion so far, regardless of high CO_2 quantity in a fuel stream. This simplification can cause inaccuracy in the numerical analysis of DIR-SOFC performance.

This study has developed a new approach to express the complex kinetics of MMR in the Ni-8YSZ anode with a single model adopting artificial neural network (ANN) and fuzzy inference system (FIS), even if either dry or steam reforming is the main reaction pathway. Moreover, applicable temperature range can easily be extended.

Although the ANN/FIS-based MMR model was established for a Ni-8YSZ anode in a temperature range of 700–800 ^{o}C based on the reforming tests using button-type anode-supported half-cells, it was revealed that the MMR model can be applied for different types of Ni-based catalysts by adjusting a correction factor to compensate the differences in catalytically-active surface area.

The validity of the ANN/FIS-based MMR model was verified by comparing calculated and measured temperature profiles for a PSC-embedded reformer operated at 800 ^{o}C with the feed of simulated biogas (CH_4/CO_2 = 1). Further validity checks under practical operating conditions of biogas-fuelled SOFCs will be presented in Chapter 4.

References

[1] J. Wei, E. Iglesia, Isotopic and kinetic assessment of the mechanism of reactions of CH_4 with CO_2 and H_2O to form synthesis gas an carbon on nickel catalysts, J. Catal. 224 (2004) 370–383.

[2] Z.L. Zhang, X.E. Verykios, Carbon dioxide reforming of methane to synthesis gas over supported Ni catalysts, Catal. Today 21 (1994) 589–595.

[3] M.C.J. Bradford, M.A. Vannice, Catalytic reforming of methane with carbon dioxide over nickel catalysts. II. Reaction kinetics, Appl. Catal., A 142 (1996) 97–122.

[4] A.L. Dicks, K.D. Pointon, A. Siddle, Intrinsic reaction kinetics of methane steam reforming on a nickel/zirconia anode, J. Power Sources 86 (2000) 523–530.

[5] M.F. Mark, F. Mark, W.F. Maier, Reaction kinetics of the CO_2 reforming of methane, Chem. Eng. Technol. 20 (1997) 361–370.

[6] T. Takeguchi, Y. Kani, T. Yano, R. Kikuchi, K. Eguchi, K. Tsujimoto, Y. Uchida, A. Ueno, K. Omoshiki, M. Aizawa, Study on steam reforming of CH4 and C2 hydrocarbons and carbon deposition on Ni-YSZ cermets, J. Power Sources 112 (2002) 588–595.

[7] R. Peters, R. Dahl, U. Klüttgen,C. Palm, D. Stolten, Internal reforming of methane in solid oxide fuel cell systems, J. Power Sources 106 (2002) 238–224.

[8] D. Mogensen, J.-D Grunwaldt, P.V. Hendriksen, K. Dam-Johansen, J.U. Nielsen, Internal steam reforming in solid oxide fuel cell: Status and opportunities of kinetics studies and their impact on modeling, J. Power Sources 196 (2011) 25–38.

[9] M.T. Hagan, H.B. Demuth, M.H. Beale, O. De Jesús, Neural Network Design, second ed., Martin Hagan, USA, 2014.

[10] E. Achenbach, E. Riensche, Methane/steam reforming kinetics for solid oxide fuel cells, J. Power Sources 52 (1994) 283–288.

[11] J.H. Edwards, A.M. Maitra, The chemistry of methane reforming with carbon dioxide and its current and potential applications, Fuel Process. Technol. 42 (1995) 269–289.

[12] V.A. Tsipouriari, X.E. Verykios, Kinetic study of the catalytic reforming of methane with carbon dioxide to synthesis gas over Ni/La_2O_3 catalyst, Catal. Today 64 (2001) 83–90.

[13] K. Girona, J. Laurencin, J. Fouletier, F. Lefebvre-Joud, Carbon deposition in CH_4/CO_2 operated SOFC: Simulation and experimentation studies, J. Power Sources 210 (2012) 381–391.

[14] Meng Ni, Is steam addition necessary for the landfill gas fueled solid oxide fuel cells?, Int. J. Hydrogen Energy 38 (2013) 16373–16386.

[15] Y. Shiratori, T. Ogura, H. Nakajima, M. Sakamoto, Y. Takahashi, Y. Wakita, T. Kitaoka, K. Sasaki, Study on paper-structured catalyst for direct internal reforming SOFC fueled by the mixture of CH_4 and CO_2, Int. J. Hydrogen Energy 38 (2013) 10542–10551.

[16] http://www.matweb.com/search/DataSheet.aspx?MatGUID=d3892ce1c0114e5d8b15ca9380d23eb5&ckck=1.

CHAPTER 4

Modeling and simulation of a DIR-SOFC operating with biogas

Numerical simulation is invaluable approach to understand physical and chemical processes occurring within the cell, investigate effectiveness of various cell/stack designs, and evaluate influences of operation parameters on SOFC performance. The estimated results can be applied for optimizing cell/stack designs and operating conditions, as a result, significantly lowering efforts, time and cost for developing SOFC-based power systems. Biogas-fuelled SOFC is one of the most promising environmentally-friendly power generation technologies, and therefore, mathematical modeling of it is of great importance.

In this Chapter, a comprehensive computational-fluid-dynamic (CFD) model of DIR-SOFC running with biogas is described. This numerical model fully couples mass- and heat transport, chemical and electrochemical processes occurring simultaneously inside the cell. If a reaction model in which both steam and dry reforming of CH_4 in the anode are taken into consideration (the methane multiple-reforming (MMR) process) (refer to Chapter 3) is incorporated, the developed CFD model will become more realistic than conventional approaches in literature that commonly neglect the contribution of dry reforming in syngas production regardless of the presence of CO_2 in large quantity.

In Sec. **4.1**, a comprehensive CFD model of DIR-SOFC considering the MMR process is described. Method and procedure of model validation are mentioned in Sec. **4.2**. Numerical investigation on SOFC behavior under DIR operation with simulated biogas is presented in Sec. **4.3**. Sec. **4.4** demonstrates the imperfection of conventional modeling approaches of MMR. Finally, important conclusions are summarized in Section **4.5**.

4.1 A comprehensive CFD model for DIR-SOFCs considering MMR

To establish a numerical model for an SOFC, at first, the cell structure consisting of various computational domains such as channels, electrodes and electrolyte was defined. Then, each phenomenon within each domain was expressed by appropriate governing equations. To reduce computing cost, in this study, the CFD model of SOFC was partially simplified with assumptions commonly approved in the field of SOFC modeling. Details on

the comprehensive CFD model of DIR-SOFC considering the MMR process for steady-state evaluation are presented in the following sub-sections.

4.1.1 Cell description

In this study, only single unit of planar ASC was considered. The CFD model of ASC is schematically illustrated in Fig. 4.1. The cell structure consists of porous electrodes (cathode and anode) separated by a gas impermeable electrolyte film. Each electrode is composed of a functional layer, where charge-transfer reactions ((1.1) for cathode, (1.2) and (1.3) for anode) are promoted, and a current collector layer also acting as gas diffusion layer. The interface between anode current collector layer (ACCL) and fuel channel was considered to be the ground. The potential at the interface between cathode current collector layer (CCCL) and air channel was assumed to be uniform and equal to the cell voltage (V_{cell}). Cell components were assumed to be homogeneous and isotropic.

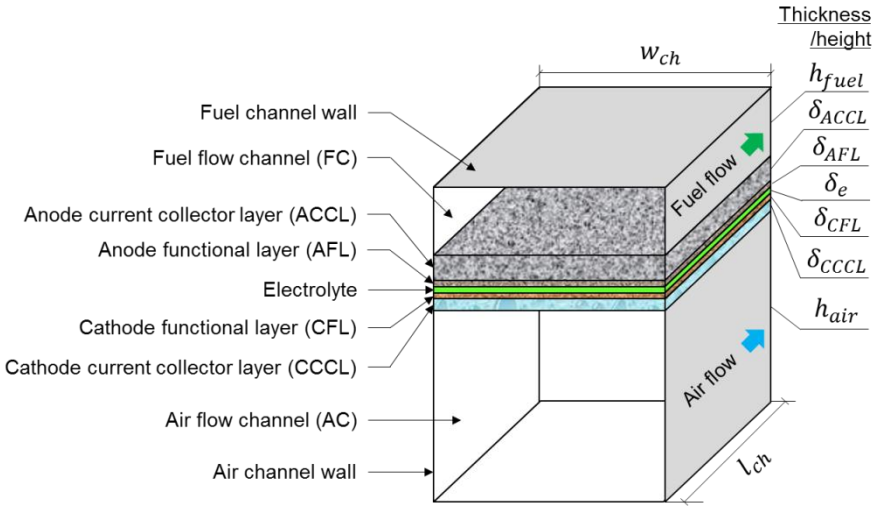

Fig. 4.1: 3D-CFD model of an anode-supported SOFC considered in this study.

In the CFD model, gas composition, fluid flow, velocity, pressure, temperature, current density and overvoltages were evaluated by solving mathematical sub-models expressing the corresponding physical and chemical processes.

4.1.2 Sub-model of mass transport

In the free-spaces of fuel and air channels and porous volume of both electrodes, gaseous species were assumed to be ideal gas, and only laminar flow was considered. For the steady-state evaluation, mass conservation of gaseous species in an infinitesimal free-space volume can be given as

$$u \cdot \nabla(\rho\omega_i) + \nabla \cdot j_i = r_i \tag{4.1}$$

,where i denotes the ith species (i.e. CH_4, CO_2, H_2O, H_2 and CO in the anode side, and O_2 and N_2 in the cathode side), ω is the mass fraction, u is the fluid velocity, ρ is the weight density, j is the mass diffusive flux and r is the net rate of production or consumption. The first and second terms in the left-hand side of Eq. (4.1) are the convective and diffusive terms in the flux, respectively, where the former expresses the contribution of the movement of the gas mixture to the flux of the ith species, and the latter describes mass transfer phenomenon driven by concentration gradients. The term in the right hand side indicates the total mass variation of the ith species as the results of the chemical and electrochemical reactions related to this species.

In fuel and air channels, u is usually low (Mach number < 0.3) [1], thus density of gas mixture is dependent on gas components, temperature and pressures and is not affected by fluid velocity. The following simplified version of Navier-Stokes momentum equation, where time dependence, gravity force and inertial terms are neglected, can be applied

$$\nabla p = \mu\nabla^2 u \tag{4.2}$$

,where p is the absolute pressure. In porous domains where the contributions of shear stresses to the momentum transport within a fluid is of importance, u was calculated by the Brinkman momentum equation

$$\nabla p = \nabla \cdot \left[\frac{1}{\varepsilon}\left\{\mu(\nabla u + (\nabla u)^{\mathrm{T}}) - \frac{2}{3}\mu(\nabla \cdot u)I\right\}\right] - \frac{\mu}{\kappa}u \tag{4.3}$$

,where ε is the porosity and κ is the permeability of a porous medium.

For the DIR-operation, anode gas is always a mixture of H_2, CO, CH_4, H_2O and CO_2, and therefore, diffusion of an individual gaseous species was coupled with others as described by the Stefan-Maxwell interdiffusion model

$$j_i = -\rho_i \sum_{k=1}^{N} D_{ik}\left(\nabla x_k + (x_k - \omega_k)\frac{\nabla p}{p}\right) \tag{4.4}$$

,where N is the number of gaseous species in the fluid, x_k is the mole fraction of the kth species, D_{ik} is the binary diffusivity between ith and kth gaseous species, which can be defined by the empirical Fuller-Schettler-Giddings formula

$$D_{ik} = \frac{10^{-3}T^{1.75}}{p}\left(V_i^{\frac{1}{3}} + V_k^{\frac{1}{3}}\right)^{-2}\left(\frac{1}{M_i} + \frac{1}{M_k}\right)^{\frac{1}{2}} \tag{4.5}$$

,where T is the absolute temperature, V is the diffusion volume and M is the molecular weight. In porous domains, D_{ik} was replaced by the effective diffusivity $D_{ik}^{eff} = (\varepsilon/\tau)D_{ik}$ to consider the influence of the tortuosity (τ) of the pore-network on the diffusion flux.

4.1.3 Sub-model of chemical reactions

Calculation flow to obtain the net consumption and production rates of CH_4, CO_2, H_2O, H_2 and CO (r_{CH_4}, r_{CO_2}, r_{H_2O}, r_{H_2} and r_{CO}, respectively) involved in chemical reactions occurring within SOFC anode is illustrated in Fig. 4.2. The MMR process was expressed by the ANN/FIS-based model (refer to Chapter 3) and the rate of WGS reaction was determined with the kinetics reported by Haberman and Young [2] for Ni-YSZ material as follows

$$r_{WGS,add} = k_{0,WGS}\left(p_{H_2O}p_{CO} - \frac{p_{H_2}p_{CO_2}}{K_{eq,WGS}}\right) \tag{4.6}$$

,where $k_{0,WGS}$ and $K_{eq,WGS}$ are the rate-constant and the equilibrium constant of WGS, respectively, given by Eqs. (4.7)–(4.9).

$$k_{0,WGS} = 0.0171exp(-103191/RT) \quad (4.7)$$

$$K_{eq,WGS} = exp(-0.2935Z^3 + 0.6351Z^2 + 4.1788Z + 0.3169) \quad (4.8)$$

$$Z = \frac{1000}{T(\mathrm{K})} - 1 \quad (4.9)$$

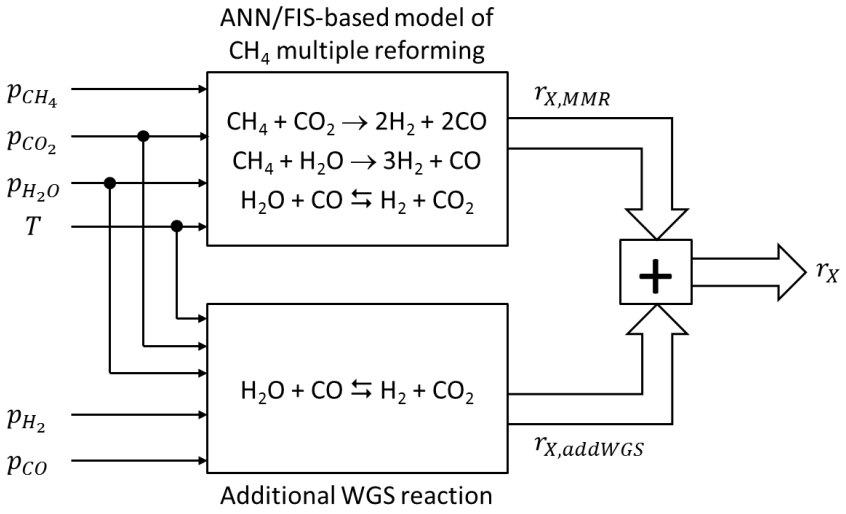

Fig. 4.2: Calculation flow to obtain net consumption and production rates of gaseous species (X = CH_4, CO_2, H_2O, H_2 and CO) involved in chemical reactions occurring within SOFC anode.

4.1.4 Sub-model of electrochemical reactions

Although both H_2 and CO are active species for anodic reactions, in the case of biogas-fuelled SOFCs, the electrochemical oxidation of H_2 is predominant as discussed in Chapter 2. Hence, electromotive force (Nernst voltage), E_{Nernst}, was determined for H_2 oxidation as

$$E_{Nernst} = E_0 + \frac{RT}{2F} ln\left(\frac{p_{H_2}}{p_{H_2O}}\right) + \frac{RT}{4F} ln\left(p_{O_2}\right) \quad (4.10)$$

,where E_0 is the electromotive force at standard pressure, R is the universal gas constant, and F is the Faraday constant. As current flows, the cell voltage (V_{cell}) is dropped from

E_{Nernst} due to various irreversible losses such as activation and ohmic losses. Using Kirchhoff's law, V_{cell} of a single cell is expressed as

$$V_{cell} = E_{Nernst} - \eta_{act,a}(i) - \eta_{act,c}(i) - \eta_{ohm}(i) \tag{4.11}$$

,where the subscripts a and c indicate anode and cathode, respectively, i is the current density, η_{act} is the activation overvoltage and η_{ohm} is the ohmic overvoltage. It should be noted that p_{H_2}, p_{H_2O} and p_{O_2} vary with respect to i, and concentration losses are included in the calculation of E_{Nernst}.

The correlation between current density and activation overvoltages can be expressed by Butler-Volmer equation. For the anodic reaction, it is written as

$$i = i_{0,a}\left[exp\left(\frac{2\alpha_a F}{RT}\,\eta_{act,a}\right) - exp\left(-\frac{2(1-\alpha_a)F}{RT}\,\eta_{act,a}\right)\right] \tag{4.12}$$

and for the cathodic reaction

$$i = i_{0,c}\left[exp\left(\frac{4\alpha_c F}{RT}\,\eta_{act,c}\right) - exp\left(-\frac{4(1-\alpha_c)F}{RT}\,\eta_{act,c}\right)\right] \tag{4.13}$$

,where α is the charge-transfer coefficient, i_0 is the exchange current density as a function of temperature and partial pressures of reactants and products as follows

$$i_{0,a} = k_{0,a}\left(\frac{p_{H_2}}{p_{H_2,ref}}\right)^{\gamma_{1,a}}\left(\frac{p_{H_2O}}{p_{H_2O,ref}}\right)^{\gamma_{2,a}} exp\left(-\frac{E_{a,a}}{RT}\right) \quad [3] \tag{4.14}$$

and

$$i_{0,c} = k_{0,c}\left(\frac{p_{O_2}}{p_{O_2,ref}}\right)^{\gamma_c} exp\left(-\frac{E_{a,c}}{RT}\right) \quad [3] \tag{4.15}$$

,where k_0 is the pre-exponential factor, γ is the power factor indicating the dependence of i_0 on the partial pressures of reactants and products and E_a is the activation energy for the charge-transfer process.

Ohmic overvoltage is caused by the electrical resistances of the component materials. Using Ohm's law, it is expressed as

$$\eta_{ohm} = R_{tot} i \tag{4.16}$$

,where R_{tot} is the total area specific resistance of a single cell.

4.1.5 Sub-model of heat transport

For the steady-state evaluation, general heat equation solving temperature field is expressed in the following form

$$\rho C_p u \cdot \nabla T + \nabla \cdot \mathbf{q} = Q_{total} \tag{4.17}$$

,where C_p is the specific heat capacity at a constant pressure, **q** is the heat flux vector and Q_{total} is the total heat source (a negative value corresponds to an endothermic process). The first term in the left hand side of Eq. (4.17) is the heat convection term due to the movement of the fluid, and therefore, vanished in the computational domain of electrolyte. **q** varies corresponding to computational domain. In the free-spaces of fuel and air channels and in the solid electrolyte, **q** can be calculated by the Fourier's law of heat conduction

$$\mathbf{q} = -k\nabla T \tag{4.18}$$

,where k is the thermal conductivity of fluid (k_f) or electrolyte (k_e). In the porous domains of electrodes, due to the simultaneous heat conductions in a fluid and a solid material, **q** was defined as

$$\mathbf{q} = -\left[\varepsilon k_f + (1-\varepsilon)k_p\right]\nabla T \tag{4.19}$$

,where k_p is the thermal conductivity of an electrode. **q** related to heat transfer through cell wall is expressed as

$$-\mathbf{n}.\,\mathbf{q} = h\left(T_{ref} - T\right) \tag{4.20}$$

,where **n** is the normal vector of the wall surface, h is the heat transfer coefficient and T_{ref} is the operating temperature. In addition, because the temperature of a channel wall, which was assumed to behave as a blackbody, is usually fixed at T_{ref} in CFD calculations, **q** associated with heat radiation between an electrode surface and a channel wall was determined by

$$-\mathbf{n}.\,\mathbf{q} = \epsilon\sigma\left(T_{ref}^4 - T^4\right) \tag{4.21}$$

,where ϵ is the emissivity of electrode surface and σ is the Stefan-Boltzmann constant.

Considering conservation of energy, Q_{total} is defined as

$$Q_{total} = Q_{chem} + Q_{elec} \tag{4.22}$$

,where Q_{chem} is the chemical heat source resulting from the MMR process and the additional WGS reaction and is given by

$$Q_{chem} = -\left[\Delta H_{WGS}\left(r_{WGS} + r_{WGS,add}\right) + \Delta H_{CP} r_{CP} + \Delta H_{RB} r_{RB} + \Delta H_{CG} r_{CG}\right] \tag{4.23}$$

,where r_{WGS}, r_{CP}, r_{RB} and r_{CG} are the net rate of WGS, CH_4 pyrolysis, reverse-Boudouard and coal gasification reactions, respectively, simultaneously occur in the MMR process (refer to Chapter 2), $r_{WGS,add}$ is the net rate of the additional WGS reaction (Eq. (4.6)) and ΔH is the enthalpy change of a reaction. Electrical heat source, Q_{elec}, is calculated under closed-circuit condition as

$$Q_{elec} = Q_{thermo} + Q_{act} + Q_{Joule} \tag{4.24}$$

where, Q_{thermo} and Q_{act} are the thermodynamic heat and the heat release caused by the activation losses of anodic and cathodic reactions, respectively, determined by Eqs. (4.25) and (4.26), respectively,

$$Q_{thermo} = \frac{T\Delta S}{2F} i \tag{4.25}$$

$$Q_{act} = \left(\eta_{act,a} + \eta_{act,c}\right) i \tag{4.26}$$

,where ΔS is the entropy change of H_2 oxidation and Q_{Joule} is the Joule heating given as

$$Q_{Joule} = \eta_{ohm} i \tag{4.27}$$

The sub-models assigned for computational domains in the comprehensive CFD model of biogas-fuelled SOFC are summarized in Table 4.1.

Table 4.1: The numerical sub-models for a biogas-fuelled SOFC considered in this study.

Numerical sub-models	Computational domains						
	FC	ACCL	AFL	EL	CFL	CCCL	AC
Convection							
Navier-Stokes	✓						✓
Brinkman		✓	✓		✓	✓	
Diffusion (Stefan-Maxwell)							
In free-space	✓						✓
In porous domains		✓	✓		✓	✓	
Heat transfer							
In fluid flows	✓						✓
In solid materials				✓			
In porous domains		✓	✓		✓	✓	
Heat sinks							
MMR process		✓	✓				
WGS reaction		✓	✓				
Heat sources							
Thermodynamics			✓				
Activation losses			✓		✓		
Ohmic losses		✓	✓	✓	✓	✓	
Heat radiation	✓						✓
Chemical reactions							
MMR process		✓	✓				
WGS reaction		✓	✓				
Electrochemical reactions							
Current-voltage		✓	✓	✓	✓	✓	
Anodic reaction			✓				
Cathodic reaction					✓		

Notes: FC fuel channel; AC air channel; AFL anode functional layer; ACCL anode current collector layer; CFL cathode functional layer; CCCL cathode current collector layer; EL electrolyte layer; MMR methane multiple-reforming; WGS water-gas shift

4.2 Model validation

4.2.1 Strategy of model validation

It is necessary to verify whether the MMR-incorporated CFD model being developed can be a good approximation of a DIR-SOFC or not. Generally, the experimentally-

obtained i-V curves reflecting the combined effects of various processes in a DIR-SOFC were used as references for the CFD model validations. However, validity of the CFD model has to be further evaluated by checking the consistencies with measured i-V curve for the feed of H_2 (non-DIR operation), ohmic and activation overvoltages, temperature distribution and reforming data.

During the sampling period of anode off-gas analysis using gas chromatograph, in-cell pressure usually tends to increase due to an elevated backpressure in an anode exhaust pipe, and this significantly influences cell performance. On the other hand, the pressure at the anode outlet of the CFD model is always fixed at 1 atm during calculation, resulting in mismatch between calculated and measured results. Besides, temperature distributions in electrode and electrolyte cannot be precisely measured due to the presence of metallic meshes for current collecting placed on the electrode surfaces of the reference SOFC. Therefore, experimentally-obtained polarization curves can become good references for the model validation. The flow of the model validation method proposed in this study (Three-step strategy) is shown in Fig. 4.3.

Step-I: Model-parameter tuning for non-DIR operation. Polarization curve of a reference SOFC was measured for the feed of humidified H_2 (Case-I). Parameters of exchange current densities ($k_{0,a/c}$, $\gamma_{a/c}$ and $E_{a,a/c}$) were adjusted to obtain a good agreement between the measured polarization curve of Case-I and the calculated one. To simplify the adjustment process, $\gamma_{a/c}$ and $E_{a,a/c}$ were pre-selected from literature, and only $k_{0,a/c}$ were adjusted.

Step-II: Model-parameter tuning for DIR operation. Polarization curve of a reference SOFC was measured for the feed of simulated biogas mixture (CH_4/CO_2 = 1) with a certain fuel flow rate (Case-II). Calculated net consumption and production rates of gaseous species involved in the MMR process (r_X) were corrected as follows

$$r_{X,cor} = k_{cor} r_X \tag{4.27}$$

,where $r_{X,cor}$ is the corrected net consumption or production rate of X and k_{cor} is the correction factor to minimize the deviation between the measured polarization curve of Case-II and the calculated one in which the adjustments of Step-I were already reflected.

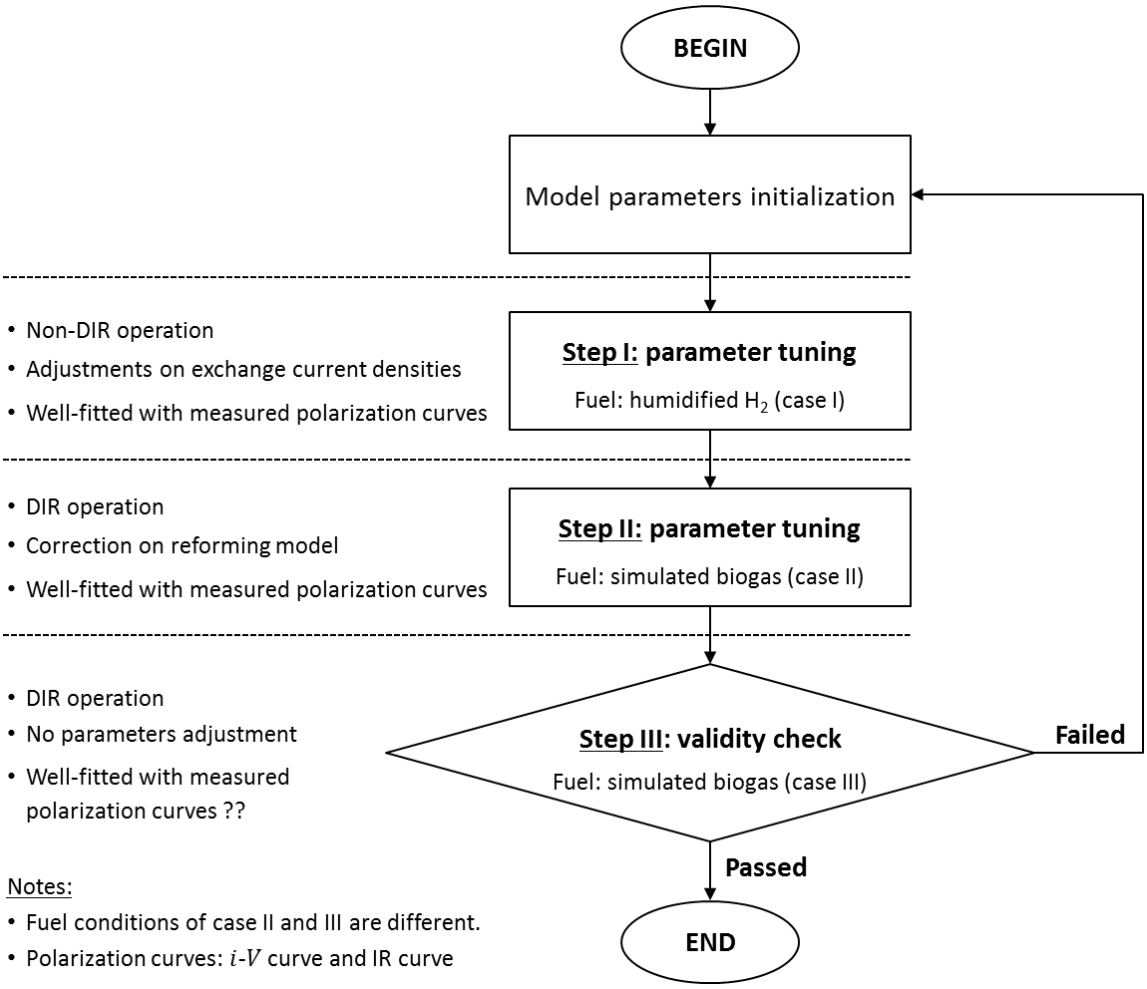

Fig. 4.3: Three-step strategy of model validation for the comprehensive CFD model of DIR-SOFC applied in this study.

Step-III: Validity check under DIR operation. Polarization curve of a reference SOFC was measured for the feed of simulated biogas mixture (CH_4/CO_2 = 1) with a different fuel flow rate from Case-II (Case-III). The validity of the CFD model revised through Step-I and Step-II is approved only if it can reproduce the experimentally-obtained polarization curve

of Case-III without any further adjustments on model parameters. If it cannot reproduce the measured polarization curve of Case-III, further adjustments of the parameters are necessary, and the three-step model validation process is restarted from Step-I.

Reliability of the MMR-incorporated CFD model to simulate DIR-SOFC developed in this study was evaluated by the above-mentioned validation strategy. In the following sub-sections, experimental procedures to measure the polarization curves of a reference SOFC, SOFC parameters pre-selected from literature and numerical methods to solve the CFD model are described.

4.2.2 Experiments

Cell Fabrication

An anode-supported cell (ASC) shown in Fig. 4.4 was fabricated using a 20×20 mm^2 squared-shaped half-cell based on Ni-8YSZ (8 mol% Y_2O_3-ZrO_2) anode substrate, same type as that used in the reforming tests (refer to Chapter 3), provided by Saga Ceramic Research Laboratory (Japan). Thicknesses of the component materials are listed in Table 4.2. To fabricate an ASC, at first, the paste of barrier layer made from $Gd_{0.10}Ce_{0.90}O_2$ (GDC) was screen printed on the surface of the electrolyte and dried. Next, the paste of NiO:10ScSZ (10 mol% Sc_2O_3-1 mol% CeO_2-ZrO_2) with a weight ratio of 80:20 was screen printed on the surface of the anode support as an anode current collector layer, followed by sintering at 1200 ^oC for 5 h. The paste of cathode functional layer (CFL), which is the mixture of $(La_{0.60}Sr_{0.40})_{0.95}(Co_{0.20}Fe_{0.80})O_{3-x}$ and $Gd_{0.10}Ce_{0.90}O_{1.95}$ (LSCF-GDC) (fuelcellmaterials, USA), was screen printed on the sintered GDC layer and dried. Then, the LSCF paste (fuelcellmaterials, USA) was printed on the dried LSCF-GDC layer as a cathode current collector layer (CCCL), subsequently sintered at 900 ^oC for 5 h to obtain the porous cathode. The resulting ASC has a straight active area of 14×14 mm^2.

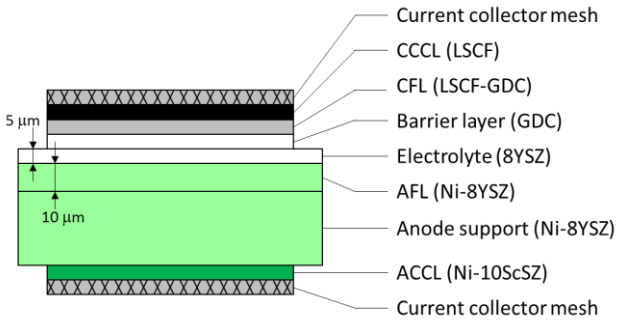

Firgure 4.4: Schematic illustration of ASC fabricated in this study.

Table 4.2: Materials and thicknesses of the ASC components used in this study.

Cell component	Material	Thickness / µm
ACCL	Ni-10ScSZ	30
Anode support	Ni-8YSZ	850
AFL	Ni-8YSZ	10
Electrolyte	8YSZ	5
Barrier layer	GDC	3
CFL	LSCF-GDC	30
CCCL	LSCF	35

Experimental Setup

The test bench for measuring the electrochemical performance of the prepared ASC is shown in Fig. 4.5. The ASC was placed in an alumina cell housing, and then, ceramic bond (Aron Ceramic, TOAGOSEI Co. Ltd., Japan) was pasted around the outer perimeter of the cell for gas sealing, followed by heating from room temperature to the operating temperature of 800 ^{o}C in 4 h. After the anode compartment was completely purged by flowing 50 mL min^{-1} of pure N_2 in plane direction, the anode gas was switched from pure N_2 to 50 mL min^{-1} of pure H_2 for the reduction treatment for 15 h.

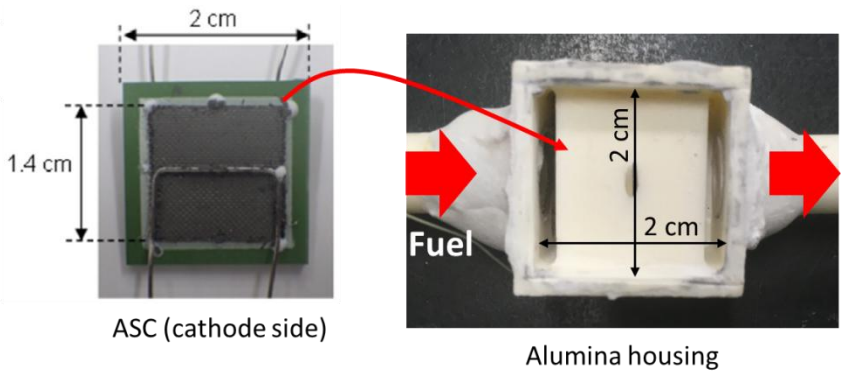

Fig. 4.5: Test bench for the electrochemical measurement of DIR-SOFC fuelled by simulated biogas.

Electrochemical Measurement

Electrochemical performances of the reference ASC at 800 ^{o}C were measured using an automatic SOFC testing system (TOYO Corporation, Japan) for the three different fuel flows (Case-I: 100 mL min^{-1} of humidified H_2 (3 vol% H_2O), Case-II: 80 mL min^{-1} of simulated biogas (CH_4/CO_2 = 1), Case-III: 40 mL min^{-1} of CH_4/CO_2 = 1). In each case, cell voltage, activation and ohmic overvoltages were measured by current interruption method within 2 A cm^{-2}. During these tests, 1 L min^{-1} of air was supplied to the cathode side in the same direction of the fuel flow (i.e. fuel-air co-flow configuration).

4.2.3 SOFC parameters

Dimensions of Cell Components

In the CFD modeling, dimensions of the cell components of the reference ASC listed in Table 4.3 were referred. The depth of electrochemical reaction zone from the electrolyte/electrode interface (i.e. the thicknesses of the AFL and the CFL in the CFD model) was assumed to be 20 μm. The rest of the electrode substrate was regarded as the current collector layer in the CFD model, that is, the thicknesses of the ACCL and the CCCL were set to 870 and 40 μm, respectively.

Table 4.3: Dimensions of the cell components.

Cell length (l_{ch}) / mm	14
Cell width (w_{ch}) / mm	14
Air channel height (h_{air}) / mm	8
Fuel channel height (h_{fuel}) / mm	1
Anode current collector layer thickness (δ_{ACCL}) / μm	870
Anode functional layer thickness (δ_{AFL}) / μm	20
Electrolyte thickness (δ_e) / μm	5
Cathode functional layer thickness (δ_{CFL}) / μm	20
Cathode current collector layer thickness (δ_{CCCL}) / μm	40

Table 4.4: Physical properties of the cell components.

Porosity	Anode (ε_a) / -	0.35 [4]	
	Cathode (ε_c) / -		
Tortuosity	Anode (τ_a) / -	3.8 [4]	
	Cathode (τ_c) / -		
Density	Anode (ρ_a) / kg m^{-3}	3310 [4]	
	Cathode (ρ_c) / kg m^{-3}	3030 [4]	
	Electrolyte (ρ_e) / kg m^{-3}	5160 [4]	
Specific heat capacity	Anode ($C_{p,a}$) / J kg^{-1} K^{-1}	450 [4]	
	Cathode ($C_{p,c}$) / J kg^{-1} K^{-1}	430 [4]	
	Electrolyte ($C_{p,e}$) / J kg^{-1} K^{-1}	470 [4]	
Thermal conductivity	Anode (k_a) / W m^{-1} K^{-1}	1.86 [4]	
	Cathode (k_c) / W m^{-1} K^{-1}	5.84 [4]	
	Electrolyte (k_e) / W m^{-1} K^{-1}	2.16 [4]	
Ionic conductivity	Electrolyte ($\sigma_{ion,e}$) / S m^{-1}	33400exp(–10300/T) [4]	
Electronic conductivity	Anode ($\sigma_{elec,a}$) / S m^{-1}	30300 [4]	
	Cathode ($\sigma_{elec,c}$) / S m^{-1}	12800 [4]	
Charge transfer coefficient	Anode (β_a) / -	0.5 [4]	
	Cathode (β_c) / -		
Exchange current density	Anode ($i_{0,a}$) / A cm^{-2} $k_{0,a}\left(\frac{p_{H_2}}{p_{H_2,ref}}\right)^{0.1}\left(\frac{p_{H_2O}}{p_{H_2O,ref}}\right)^{0.5} exp\left(-\frac{70000}{RT}\right)$	[5]	(4.28)
	Cathode ($i_{0,c}$) / A cm^{-2} $k_{0,c}\left(\frac{p_{O_2}}{p_{O_2,ref}}\right)^{0.5} exp\left(-\frac{130000}{RT}\right)$	[6]	(4.29)

($k_{0,a}$ and $k_{0,c}$ were both determined in Step-I of the three-step model validation process)

Physical Properties of the Cell Components

Although the physical properties of the cell components were not experimentally-measured from the reference ASC, during model-parameter tuning (Step-I), the solution of the CFD model was found to be more sensitive with respect to $k_{0,a/c}$ and k_{cor} than others. Therefore, general physical properties of the cell components listed in Table 4.4 were adopted in this study.

4.2.4 Numerical methods

In this study, the CFD model was discretized and solved by the commercial code of COMSOL Multiphysics (COMSOL Group, Sweden) based on the FEM technique. Fineness of the calculating mesh was adjusted so that the solution of the CFD model was converged. The resulting calculating mesh of the CFD model used for the model validation is illustrated in Fig. 4.6, and the numbers of mesh elements for the respective computational domains are listed in Table 4.5.

Initial values and boundary conditions for the calculation corresponding to the operating conditions were summarized in Table 4.6. Initial temperature and pressure of the system were set to 800 ^{o}C and 1 atm, respectively. For the fluid flow calculations, inlet temperatures of the fuel and the air streams were set to 800 ^{o}C as initial conditions. At the outlets of the fuel and the air channels, pressure was assumed to be 1 atm. A constant laminar-flow velocity was adopted as a boundary condition at the inlet of the fuel channel. Corresponding to the total mass flow rate of a fuel, an appropriate magnitude of laminar-flow velocity was pre-determined. The similar boundary setting strategy was applied to the inlet and the outlet of the air channel.

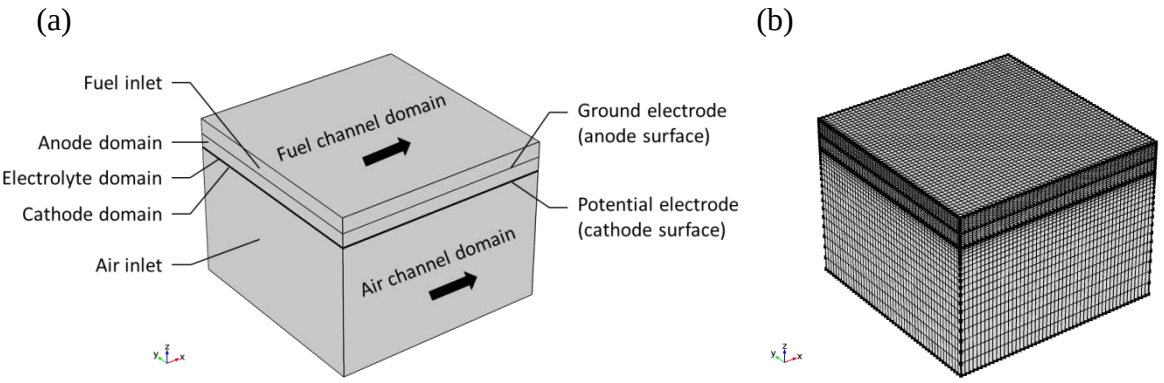

Fig. 4.6: Illustrations of (a) geometry and (b) calculating mesh for the MMR model-incorporated CFD calculation used in the model validation.

Table 4.5: Numbers of mesh elements in computational domains for a 14 × 14 mm^2 planar ASC.

Domains	No. of mesh elements
Fuel channel	25000
ACCL	17500
AFL	7500
Electrolyte	7500
CCL	7500
CFL	12500
Air channel	50000
Total	127500

For the heat transport calculations, temperatures of the channel walls and the surrounding walls of the cell were all fixed to 800 ^{o}C as boundary conditions.

Potential of the ground (the interface between ACCL and fuel channel) was fixed at 0 V. V_{cell} (the potential at the interface between CCCL and air channel) can be calculated as

$$V_{cell} = OCV - V_{pol} \tag{4.30}$$

,where OCV is the open-circuit voltage and V_{pol} is the total polarization. The following Nernst expression was used for incorporating the measured OCV to the CFD calculation

$$E_{Nernst} = OCV_{exp} + \frac{RT}{2F} ln\left(\frac{p_{H_2}}{p_{H_2,OCV}} \frac{p_{H_2O,OCV}}{p_{H_2O}}\right) + \frac{RT}{4F} ln\left(\frac{p_{O_2}}{p_{O_2,OCV}}\right) \tag{4.31}$$

,where the subscript OCV indicates the open-circuit condition and OCV_{exp} is the experimentally-obtained OCV. The second and the third terms in the right hand side of the Eq. (4.31) represent concentration losses in anode and cathode sides, respectively.

Table 4.6: Operating conditions.

Fuel (inlet)	
Temperature / °C	800
Fuel composition / %	H_2: 97, H_2O: 3 (Case-I)
	CH_4: 50, CO_2: 50 (Case-II and -III)
Velocity / m s^{-1}	0.435 (Case-I)
	0.348 (Case-II)
	0.174 (Case-III)
Air (inlet)	
Temperature / °C	800
Air composition / %	O_2: 21, N_2: 79
Velocity / m s^{-1}	0.505

For each V_{pol}, iterative calculation was carried out to obtain the converged results of current density, overvoltages, gas compositions, fluid flows, velocity, pressure, and temperature. From the sub-models of chemical and electrochemical reactions, gas compositions, reaction rates, current density and overvoltages were solved using temperature and the partial pressures of reactants and products. Then, these obtained results were used to determine the source terms in the sub-models of mass and heat transports to update the distributions of fluid flow, velocity, pressure and temperature. After the calculations of the sub-models of mass and heat transports, convergence check was carried out by checking whether the relative deviation between the current and previous solutions (relative tolerance (Eq. (4.32)) was less than 1e–3 or not. This calculation loop was repeated until convergences of all results were satisfied.

$$\text{Relative tolerance} = \left|\frac{X_n - X_{n-1}}{X_{n-1}}\right| \tag{4.32}$$

,where X_{n-1} and X_n are the previous and current solutions, respectively.

4.3 Results and Discussion

4.3.1 Model validation

Measured *i-V* curves of the 14 × 14 mm^2 reference ASC fuelled by 100 mL min^{-1} flow of H_2 (3 vol% H_2O) (Case-I) and 80 mL min^{-1} flow of CH_4/CO_2 = 1 (Case-II) are shown in Fig. 4.7-(a), where the calculated curves after the adjustments of $k_{0,a}$ and $k_{0,c}$ (Step-I) and k_{cor} (Step-II) for Case-I and Case-II, respectively, were also plotted for the comparison. The calculated performances well fitted to the measured performances. As the fuel stream was switched from H_2 to CH_4/CO_2 = 1, the cell performance was lowered. Cell performance is, of course, strongly dependent on the fuel composition and temperature, here determined by the MMR process and WGS reaction. Decrease in cell temperature, resulting from the endothermic MMR, increased ohmic resistance of the electrolyte components and the charge transfer resistances at both anode/electrolyte and cathode/electrolyte interfaces.

The consistency of the results obtained from the MMR model-incorporated 3D-CFD calculations with the experimental results for Case-III (see Fig. 4.7-(b)) proves that the developed method for the modeling of MMR can be used for the precise prediction of the electrochemical performance of DIR-SOFCs (In Step-III (validity check), parameter adjustments were not made.). This indicates that the assumptions used in the MMR modeling are reasonable, and the realistic distributions of the fuel composition, temperature, and current density during DIR operation can be estimated.

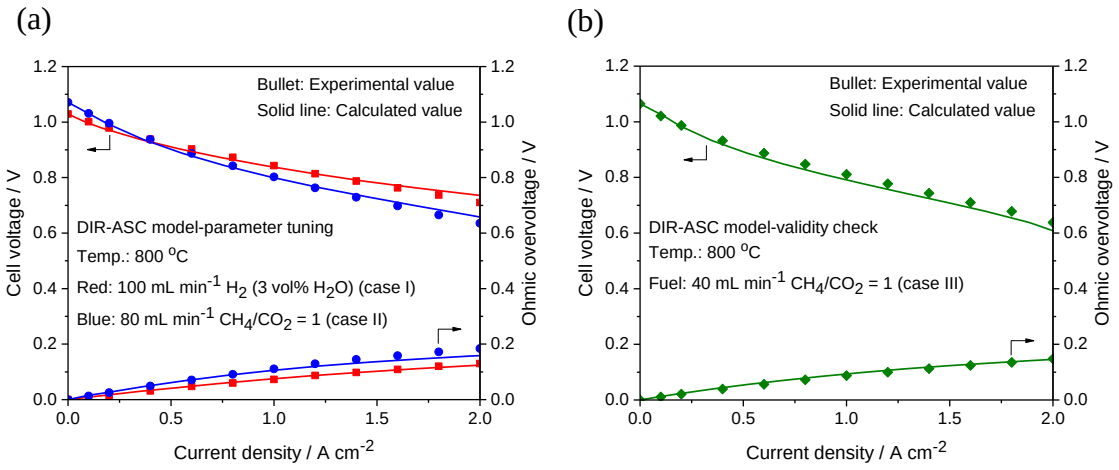

Fig. 4.7: i-V curves of the 14 × 14 mm^2 reference ASC under the operating conditions listed in Table 4.6. (a) 100 mL min^{-1} flow of H_2 (3 vol% H_2O) (Case-I (red)), 80 mL min^{-1} flow of CH_4/CO_2 = 1 (Case-II (blue)), and (b) 40 mL min^{-1} flow of CH_4/CO_2 = 1 (Case-III). Scatter and line plots show the measured and calculated results, respectively.

Validity check was further conducted for another reference ASC with a surface area of 20 × 50 mm^2 shown in Fig. 4.8. This rectangular-shaped ASC was also based on a Ni-8YSZ anode-supported half-cell provided by Saga Ceramic Research Laboratory composed of a 920 μm-thick anode substrate and a 5 μm-thick electrolyte. The complete ASC was fabricated through the procedure described in Sec. **4.4**. Sizes of the computational domains of the CFD model were adjusted to the geometry of this rectangular-shaped reference ASC, that is, cell length (l_{ch}) and channel width (w_{ch}) were set to 20 and 50 mm, respectively, and the thicknesses of ACCL (δ_{ACCL}) were set to 930 μm.

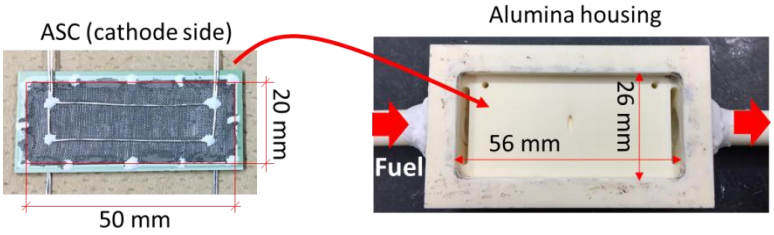

Fig. 4.8: Test bench of the electrochemical measurement for the 20 × 50 mm^2 DIR-SOFC fuelled by simulated biogas. The prepared ASC was placed on the alumina housing to, and then, the outer perimeter of the cell was sealed with ceramic bond.

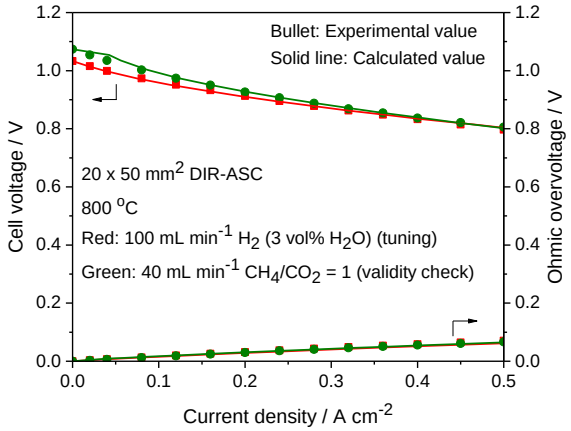

Fig. 4.9: *i-V* curves of the 20 × 50 mm^2 reference ASC at 800 ^{o}C with 100 mL min^{-1} flow of H_2 (3 vol% H_2O) (red) and 40 mL min^{-1} flow of CH_4/CO_2 = 1 (blue). Scatter and line plots show the measured and calculated results, respectively.

By the size enlargement from 14 × 14 to 20 × 50 mm^2, ohmic resistance tended to increase because of the difficulty of uniform current collection. Therefore, model-tuning in Step-I was required to compensate this discrepancy, and was carried out by adjusting $k_{0,a/c}$ so that the CFD model can reproduce the polarization curve of Case-I (100 mL min^{-1} of humidified H_2 (3 vol% H_2O)). Then, without adjustment of k_{cor} of the MMR model, fuel flow condition was switched from Case-I to Case-III (40 mL min^{-1} of CH_4/CO_2 = 1 mixture). As shown in Fig. 4.9, again, a good agreement between the calculation and the experiment was confirmed, demonstrating the validity of the ANN/FIS-based MMR model-incorporated CFD calculation in this study.

4.3.2 Behavior of a DIR-SOFC fuelled by biogas

Behavior of the 14 × 14 mm^2 reference ASC for Case-III (40 mL min^{-1} of CH_4/CO_2 = 1 mixture) was estimated by the experimentally-verified CFD model. Here, distributions of chemical species, temperature and thermally-induced stress will be presented. Although carbon formation is thermodynamically expected for the mixture of CH_4/CO_2 = 1, carbon

accumulation was kinetically slow as observed in the reforming tests (Chapter 3), and therefore, the formation of solid carbon was not considered.

4.3.2.1 Distribution of gaseous species

Distributions of gaseous species for the anode side under DIR operation with the direct feed of biogas (CH_4/CO_2 = 1) are shown in Figs. 4.10.

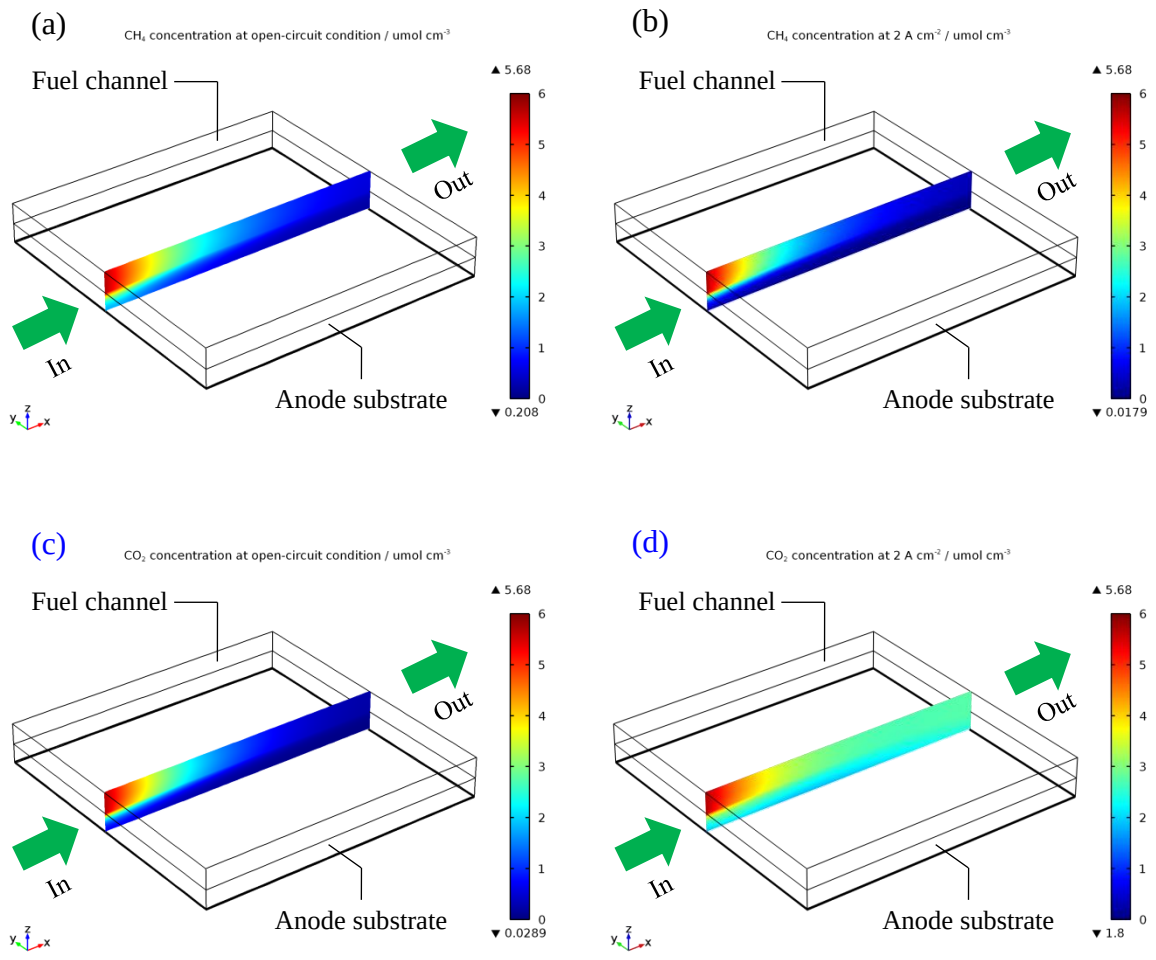

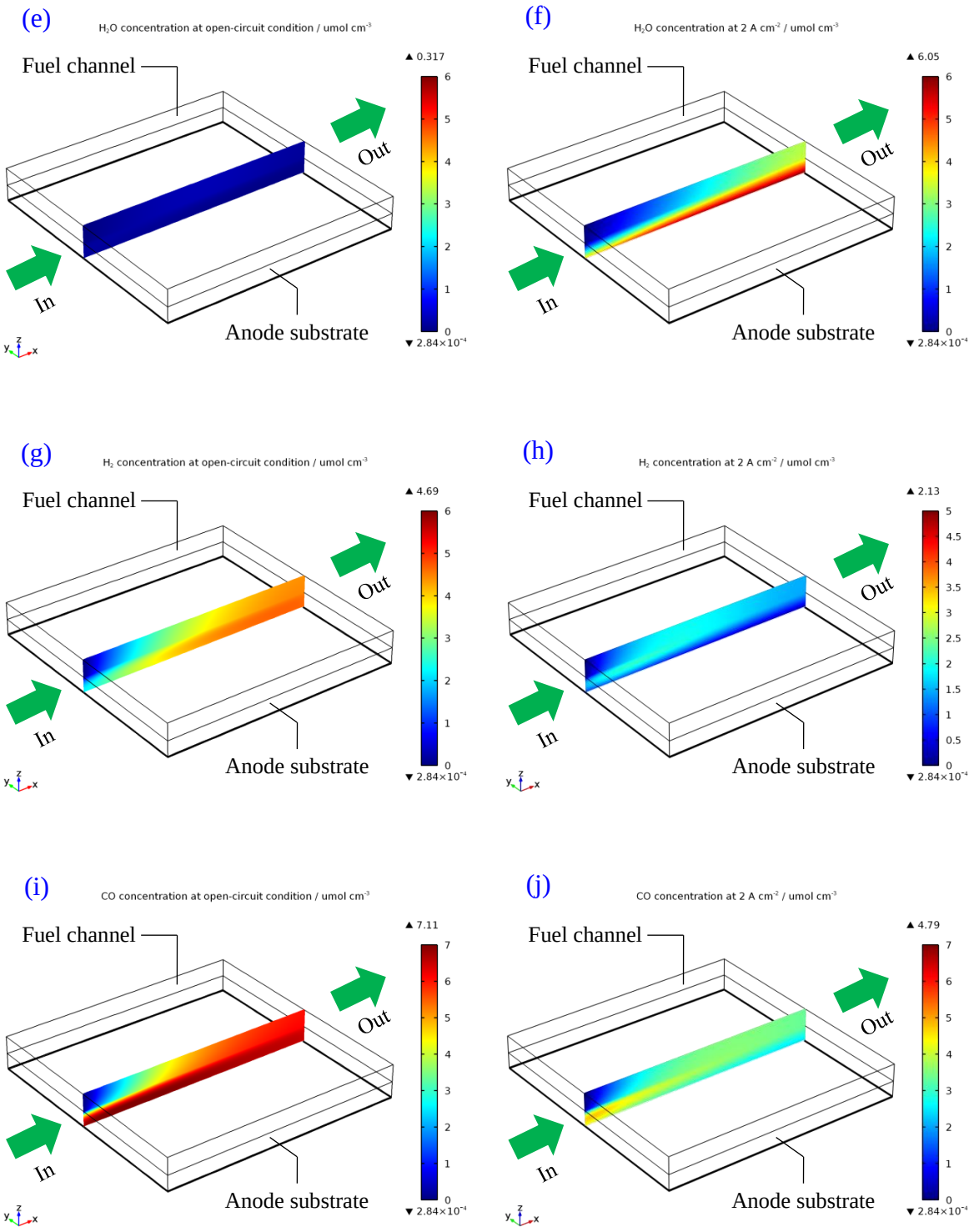

Fig. 4.10: Cross sectional distributions of (a,b) CH_4, (c,d) CO_2, (e,f) H_2O, (g,h) H_2, (i,j) CO concentrations along the center-line of the fuel flow for the 14 × 14 mm^2 reference ASC of Case-III (40 mL min^{-1} of CH_4/CO_2 = 1); (a,c,e,g,i) under open-circuit condition and

(b,d,f,h,j) at 2 A cm^{-2}. ▼ and ▲ indicate the minimum and maximum values of mole fraction, respectively.

As shown in Fig. 4.10-(a), under open-circuit condition, CH_4 conversion was almost completed within the front half of the cell mainly by the dry reforming process (reaction (1.6) listed in Table 1.5) in the anode substrate. Current load (here 2 A cm^{-2}) promoted CH_4 conversion (see Fig. 4.10-(b)) because oxygen is supplied from cathode side through electrolyte during power generation. H_2 produced by CH_4 dry reforming is electrochemically oxidized by this oxygen to generate electricity and H_2O as by-product (reaction (1.2)) which contributes to CH_4 conversion through steam reforming reaction (reaction (1.7)). Under open-circuit condition, profile of the CO_2 concentration was similar to that of CH_4 (compare (a) and (c)). However, under current load, that ((d)) was completely different from CH_4 profile ((b)). This indicates the contribution of forward-WGS reaction (reaction (1.8). CO produced by MMR (reactions (1.6) and (1.7)) reacts with H_2O derived from reaction (1.2) to reproduce CO_2 and H_2.

Under open-circuit condition, H_2O was slightly produced. This is due to the reverse-WGS reaction ((e)). At 2 A cm^{-2}, H_2O mole fraction increased along fuel flow direction ((f)), indicating that H_2O production by reaction (1.2) overcomes H_2O consumption by reactions (1.7) and (1.8).

CH_4 conversion under open-circuit condition was localized at the fuel inlet side ((a)), however H_2 production started from a little downstream position ((g)) because of reverse-WGS. In the rear half of the cell, H_2 concentration within the anode was over 4 μmol cm^{-3}, and nearly no contrast between anode and fuel channel was observed at the outlet, indicating high diffusivity of H_2 within the porous anode material. During DIR operation at 2 A cm^{-2}, H_2 was readily consumed, and H_2 depletion was observed especially within the rear half of the anode substrate ((h)), suggesting that H_2 starvation may occur at higher current density to cause fuel cell breakdown.

At the OCV, CO concentration was higher than that of H_2 (compare (g) and (i)) due to reverse-WGS reaction, and thus reformate gas was attributed to molar ratio of $H_2/CO < 1$.

At 2 A cm^{-2}, within the entrance region of the anode substrate the rate of shifting CO to CO_2 was superior to the rate of CO production from MMR process; as a result, CO concentration decreased to less than 5 μm cm^{-3} ((j)). Toward downstream, syngas production rate was quickly dropped, resulting in further decrease of CO concentration.

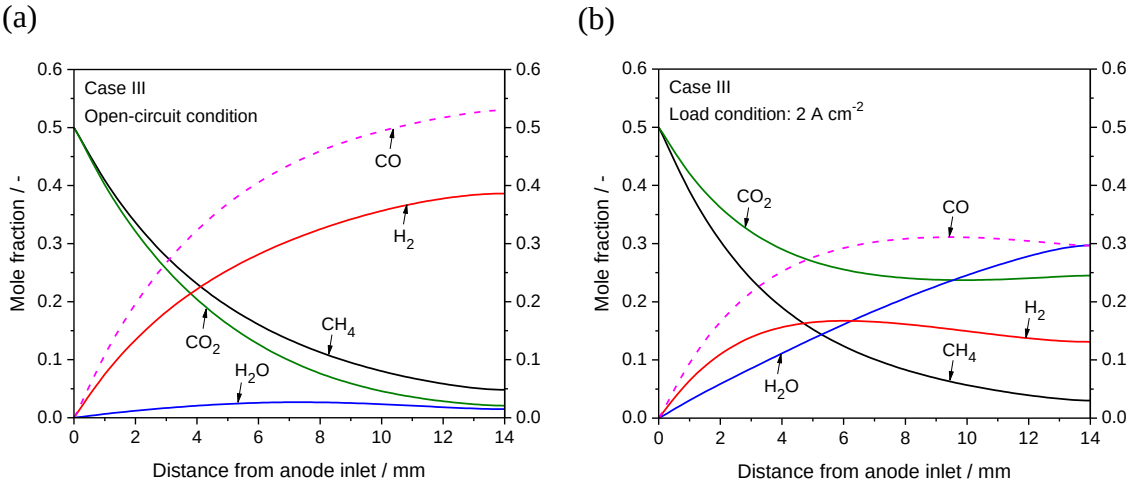

Fig. 4.11: Calculated distribution of fuel composition along fuel flow direction in the 14 × 14 mm^2 reference ASC for Case-III. (a) and (b) are the mole fraction profiles of gaseous species under open-circuit condition and at 2 A cm^{-2}, respectively.

The mole fraction profiles of gaseous species along the fuel flow channel under open-circuit condition for Case-III are shown in Fig. 4.11-(a). The results indicate that the supplied CH_4 is not totally reformed (CH_4 conversion (χ_{CH_4}) is 84.3%). Due to the high p_{CO_2}, the WGS reaction is shifted to the reactant side (reverse-WGS), resulting in a higher net rate of CO_2 consumption than that of CH_4 and a higher net CO production rate than that of H_2. Thus, the gas compositions are $CH_4/CO_2 > 1$ and $H_2/CO < 1$ over the channel length. Dry reforming and the reverse-WGS reactions clearly predominate under open-circuit conditions. Meanwhile, under the load condition of 2 A cm^{-2}, corresponding to a fuel utilization of about 37% (see Fig. 4.11-(b)), a lower CH_4 mole fraction at the channel outlet (0.03) than that for open-circuit condition (0.048) was observed, indicating that syngas production was promoted by H_2O produced internally by the electrochemical oxidation of

H_2, and slightly increasing χ_{CH_4} from 84.3 to 89.8%. At a distance of 9 mm from the inlet, the CO mole fraction gradually drops in the fuel flow direction, accompanied an almost constant CO_2 mole fraction, reflecting that the WGS reaction is shifted to the product side by the large quantity of H_2O. The consumption of CO_2 by dry reforming is compensated with CO_2 production by the WGS.

4.3.2.2 Heat balance

Chemical heat source (Q_{chem}), electrical heat source (Q_{elec}) and total heat source ($Q_{total} = Q_{chem} + Q_{elec}$) are plotted as a function of current density in Fig. 4.12. Under open-circuit condition, dry reforming and reverse-WGS reactions are predominant, resulting in Q_{chem} of about –3.8 W corresponding to χ_{CH_4} of 84.3 %. With increasing current density from 0 to 0.2 A cm^{-2}, Q_{chem} increased to about –4 W (+5.3 %) where χ_{CH_4} was 91.1 % (+8 %) due to the contribution of steam reforming in syngas production. Further increase in current density to 2 A cm^{-2}, Q_{chem} decreased to –3.3 V (–17.5%) mainly related to the partial substitution of steam reforming (ΔH_{298K}= 206 kJ mol^{-1}) for dry reforming (ΔH_{298K}= 247 kJ mol^{-1}) and the slightly exothermic forward-WGS reaction (ΔH_{298K}= –41 kJ mol^{-1}). At 2 A cm^{-2}, the backflows of H_2O (by-product of the anodic reaction of H_2) and CO_2 (by-product of the forward-WGS reaction) could suppress the flow of CH_4 entering the catalyst volume, in consequence, χ_{CH_4} slightly decreased to 89.9% (–1.3%), also weakly contributing to the decrease in Q_{chem}. With increasing current density from 0 to 2 A cm^{-2}, Q_{elec} increased to about 2.7 W. As Q_{total} was always negative within 2 A cm^{-2} (see Fig. 4.12-(b)), it can be said that the cell should be operated at higher current density so that thermally self-sustained operation can be achieved. DIR operation under this condition is the most efficient way to collect thermal energy required for CH_4 reforming.

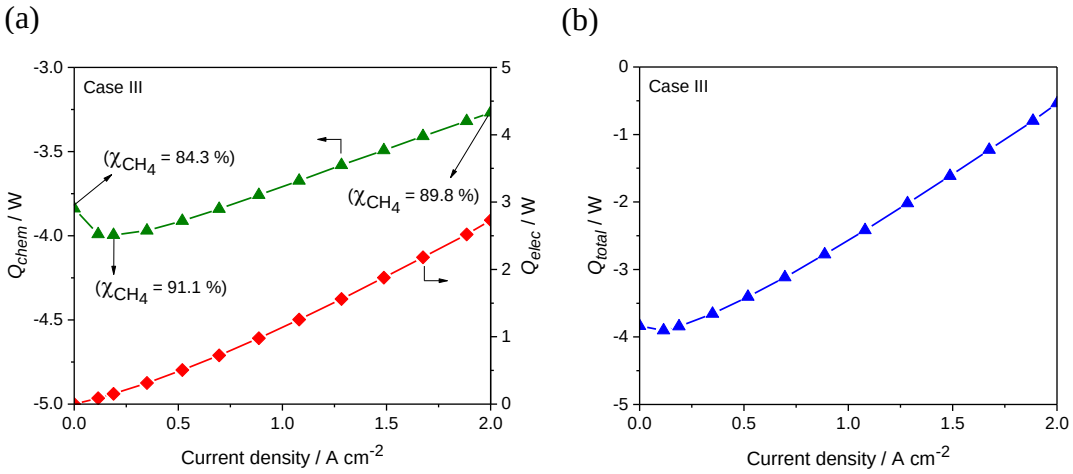

Fig. 4.12: Heat source as a function of current density for the 14 × 14 mm^2 reference ASC for Case-III: (a) chemical and electrical heat sources (Q_{chem} and Q_{elec}, respectively) and (b) total heat source (Q_{total} = Q_{chem} + Q_{elec}). Negative value of heat source indicates endothermicity. χ_{CH_4} indicates CH_4 conversion.

4.3.2.3 Distributions of temperature and thermal stresses

Figs. 4.13 and 14 provide the distributions of temperature inside the cell and thermally-induced stress (first principal stress) in electrolyte, respectively, for the DIR operation with the direct feed of biogas. Under open-circuit condition, considerably large temperature drop of 119 ^oC and maximum thermally-induced stress of 165 MPa occurred within the front half of the cell along fuel flow direction, because CH_4 conversion rapidly proceeds in this region. At 2 A cm^{-2}, large portion of Q_{elec} was recycled for endothermic CH_4 reforming (see Fig. 4.12), and therefore, temperature drop was remarkably suppressed to have uniform stress distribution in the electrolyte.

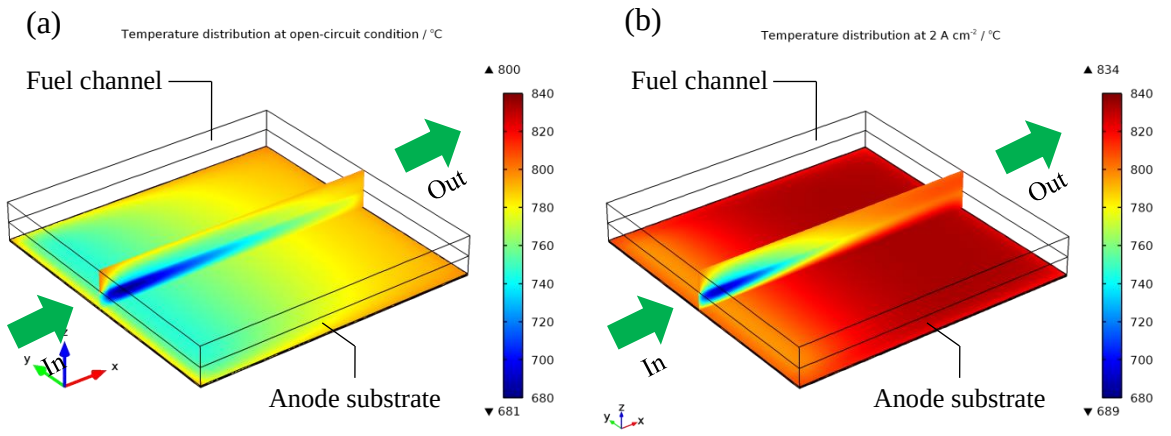

Fig. 4.13: Calculated spatial variation of temperature within the anode side of the 14 × 14 mm^2 reference ASC of Case-III (40 mL min^{-1} of CH_4/CO_2 = 1) (a) under open-circuit condition and (b) at 2 A cm^{-2}, showing temperature distributions in the electrolyte surface and in the direction vertical to the electrolyte surface along fuel flow direction. ▼ and ▲ indicate the minimum and maximum values of temperature, respectively.

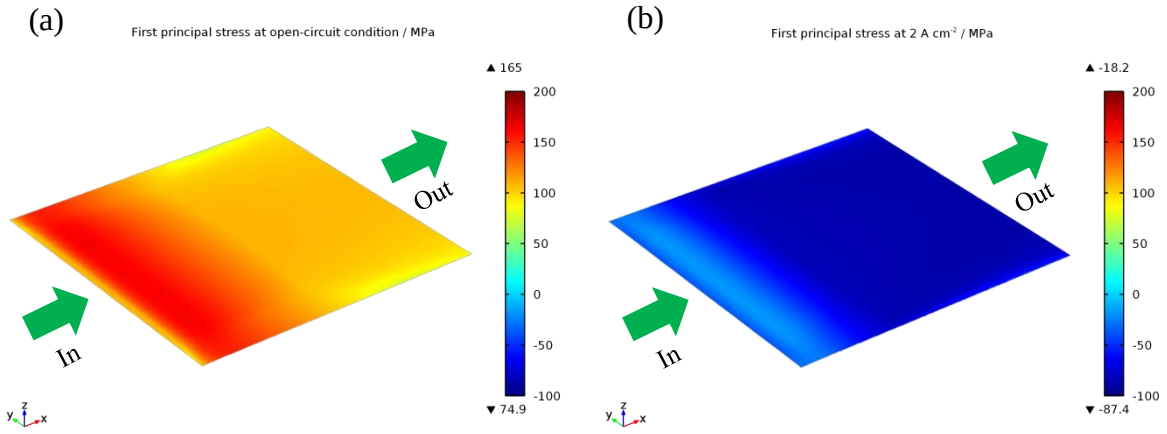

Fig. 4.14: Calculated distributions of thermally-induced stress (first principal stress (σ_e^T)) generated in the electrolyte plane of the 14 × 14 mm^2 reference ASC of Case-III (40 mL min^{-1} of CH_4/CO_2 = 1) (a) under open-circuit condition and (b) at 2 A cm^{-2}. ▼ and ▲ indicate the minimum and maximum values of σ_e^T, respectively.

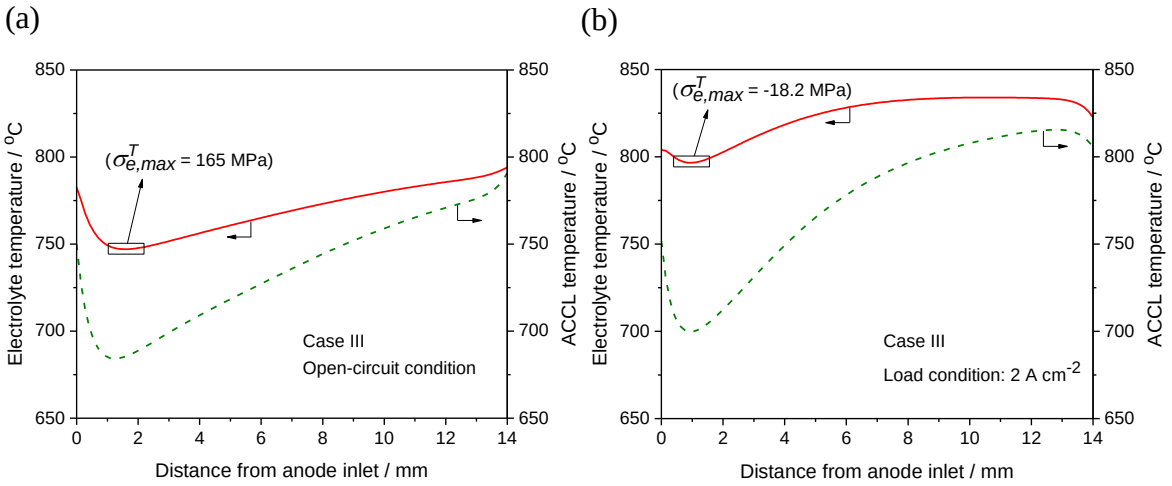

Fig. 4.15: Calculated temperature profiles of the electrolyte and the ACCL along fuel flow direction of the 14 × 14 mm^2 reference ASC of Case-III (40 mL min^{-1} of CH_4/CO_2 = 1) (a) under open-circuit condition and (b) at 2 A cm^{-2}. Rectangle indicates the position where the maximum thermally-induced stress (first principal stress ($\sigma^T_{e,max}$)) occurs.

Temperature profiles of the electrolyte (T_e) and the ACCL (main reforming zone) (T_{ACCL}) in the fuel flow direction under open-circuit condition and at 2 A cm^{-2} for Case-III are shown in Fig. 4.15. Under open-circuit condition, T_{ACCL} significantly decreased by a maximum of 119 °C, because of the endothermicities of the dry reforming and reverse-WGS reactions, resulting in T_e drop of about 53 °C at 1.5 mm from the inlet, where CH_4 consumption was strongly enhanced by the high reactant partial pressures. Towards downstream, the CH_4 consumption rate was reduced due to the decrease in the reactant partial pressures, and therefore, the T_e drop was lessened. The maximum thermally-induced tensile stress (as first principal stress) in the electrolyte, $\sigma^T_{e,max}$, was calculated to be 165 MPa in the lowest T_e region. Although the predicted $\sigma_{1,max}$ was smaller than the fracture strength of conventional electrolyte materials (about 236–275 MPa) [1, 7], if additional stresses are generated, the total stress generated in the electrolyte may exceed the cracking threshold of the dense electrolyte thin film. At 2 A cm^{-2}, the maximum T_e drop was 3 °C, significantly lower than that under the open-circuit condition, and the value of $\sigma^T_{e,max}$ was

calculated to be −18.2 MPa (compressive stress). As a result, the risk of electrolyte fracture was strongly reduced during operation.

Above calculated results confirmed that under the DIR operation syngas production is enhanced by steam reforming which is promoted with respect to load condition. Under operating conditions considered in this study, complete CH_4 conversion could not be obtained even at high current densities because backflows of H_2O and CO_2 could suppress CH_4 transport to the anode substrate. Moreover, inevitably low H_2 mole fraction at the fuel inlet region essentially reduces local electromotive force. These suggest that, in order to enhance power characteristics, almost complete CH_4 conversion and rapidly-rising rate of H_2 mole fraction at the fuel inlet region should be obtained. Calculated results also confirmed that CH_4 conversion mostly proceeds within the fuel inlet region and so drastically inducing thermal stresses in electrolyte, suggesting that the trade-off between thermo-mechanical stability and power generation must be carefully compromised in the development of biogas-fuelled SOFC systems.

4.4 Imperfection of conventional modeling approaches of MMR

Distributions of fuel composition and temperature inside the DIR-SOFCs fulled by biogas have been reported in many numerical works which considered only CH_4 steam reforming as the main syngas production pathway [8–18].

Some works have considered MMR as the sum of dry and steam reforming processes ignoring the concurrent effects of CO_2 and H_2O in the catalytic CH_4 conversion (hereafter called parallel-reforming approach) [19, 20]. To investigate the risk of carbon deposition under DIR operation with biogas, Girona *et al.* assumed that kinetic parameters, pre-exponential factor and activation energy, for dry reforming within Ni-based cermet anodes were exactly identical to those of steam reforming [19]. In their work, although *i-V* curve of an ASC (anode thickness of 1.5 mm and surface area of 12.5 cm^2) operated at 800 ^oC with 210 mL min^{-1} humidified biogas (CH_4/CO_2 = 1 (6 vol% H_2O)) could be reproduced, it was unrealistic to apply this approach for general cases. Meng Ni evaluated the effect of

methane humidification on the performance of landfill gas-fuelled SOFCs by applying dry reforming kinetics experimentally-derived from Ru/γ-Al_2O_3/Ni-Cr-Al catalyst (Eqs. (4.33)–(4.36)) and that of steam reforming reported by Haberman and Young (Eqs. (4.37)–(4.41)), which have been commonly used in numerical works of DIR-SOFCs running with humidified CH_4 fuels [20].

Table 4.7: Kinetic model used in the Meng Ni's parallel-reforming approach [20].

Reaction rate of CH_4 dry reforming (r_{MDR}) on Ru/γ-Al_2O_3/Ni-Cr-Al catalyst [21]	
$$r_{MDR} = \frac{k_{CO_2} K_{CO_2} K_{CH_4} p_{CO_2} p_{CH_4}}{\left(1 + K_{CO_2} p_{CO_2} + K_{CH_4} p_{CH_4}\right)^2}$$	(4.33)
$$k_{CO_2} = 1.17 \cdot 10^7 exp\left(-\frac{83498}{RT}\right)$$	(4.34)
$$K_{CO_2} = 3.11 \cdot 10^{-3} \exp\left(\frac{49220}{RT}\right)$$	(4.35)
$$K_{CH_4} = 0.653 exp\left(\frac{16054}{RT}\right)$$	(4.36)
Reaction rate of CH_4 steam reforming (r_{MSR}) on Ni-based SOFC anodes [2]	
$$r_{MSR} = k_{f,MSR}\left(p_{CH_4} p_{H_2O} - \frac{p_{CO} p_{H_2}^3}{K_{eq,MSR}}\right)$$	(4.37)
$$k_{f,MSR} = \frac{2395}{3} exp\left(-\frac{231266}{RT}\right)$$	(4.38)
$$K_{eq,MSR} = 1.0267 \cdot 10^{10} exp\big(A(Z)\big)$$	(4.39)
$$A(Z) = -0.2513Z^4 + 0.36651Z^3 + 0.5810Z^2 - 27.134Z + 3.277$$	(4.40)
$$Z = \frac{1000}{T} - 1$$	(4.41)
Consumption and production rates of gaseous species	
$$r_{CH_4} = -r_{MDR} - r_{MSR}$$	(4.42)
$$r_{CO_2} = -r_{MDR}$$	(4.43)
$$r_{H_2O} = -r_{MSR}$$	(4.44)
$$r_{H_2} = 2r_{MDR} + 3r_{MSR}$$	(4.45)
$$r_{CO} = 2r_{MDR} + r_{MSR}$$	(4.46)

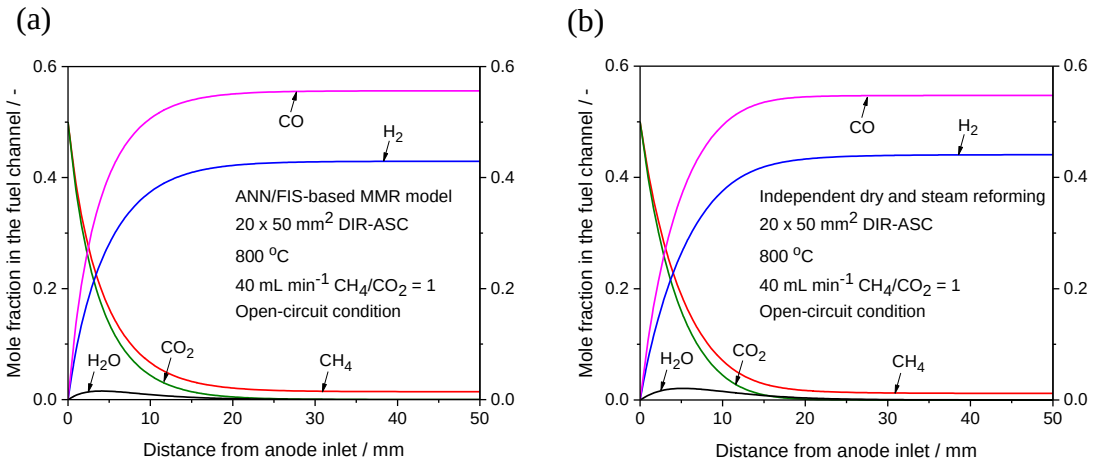

Fig. 4.16: Distribution of fuel composition in fuel channel along fuel flow direction under open-circuit condition in the 20 × 50 mm^2 reference ASC operating at 800 ^oC with 40 mL min^{-1} simulated biogas (CH_4/CO_2 = 1) calculated with (a) the ANN/FIS-based MMR model (this study) and (b) the parallel-reforming approach [20].

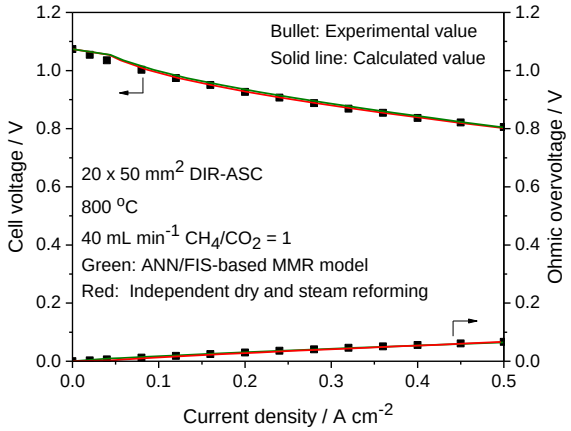

Fig. 4.17: Comparison of calculated and measured i-V curves for the 20 × 50 mm^2 reference ASC operating at 800 ^oC with 40 mL min^{-1} simulated biogas (CH_4/CO_2 = 1); Green: Calculated i-V curve with the ANN/FIS-based MMR model, Red: Calculated i-V curve with the parallel-reforming approach [20]. Scatter plots: Measured i-V curve.

Distributions of fuel composition in fuel channel along fuel flow direction under open-circuit condition obtained by the ANN/FIS-based MMR model (this study) and the parallel-reforming approach are compared in Fig. 4.16. Under open-circuit condition, both modeling approaches provided almost same profiles. χ_{CH_4} of about 95% was calculated and

syngas production through dry reforming was almost completed within 20 mm from the inlet. As shown in Fig. 4.17, within 0.5 A cm^{-2} no differences between i-V curves obtained by both MMR models can be seen. However, in the mole fraction profiles of CH_4, CO_2 and CO in the AFL obtained at 0.5 A cm^{-2}, difference was obvious. The ANN/FIS-based MMR model could give a smooth profile (Fig. 4.18-(a)), whereas the parallel-reforming model resulted in discontinuous profile (Fig. 4.18-(b)), indicating that the present approach adopting ANN/FIS-based MMR can be applicable for the complex system where both CO_2 and H_2O contributions to CH_4 reforming are rather large.

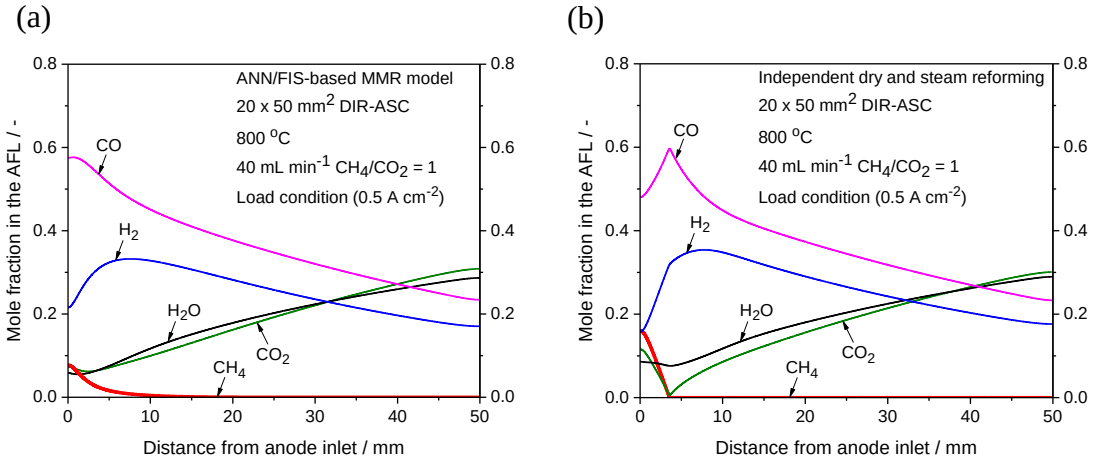

Fig. 4.18: Distribution of fuel composition in AFL along fuel flow direction at 0.5 A cm^{-2} in the 20 × 50 mm^2 reference ASC operating at 800 °C with 40 mL min^{-1} simulated biogas (CH_4/CO_2 = 1) calculated with (a) the ANN/FIS-based MMR model (this study) and (b) the parallel-reforming approach [20].

During i-V calculation with the parallel-reforming approach, r_{MDR} and r_{MSR} were simultaneously solved with the same p_{CH_4}, and thus the r_{CH_4} calculated by (Eq. 4.42) caused overestimation under the condition in which both CO_2 and H_2O are major components, leading to negative CH_4 concentration within a local catalyst volume. In the CFD calculations adopting the parallel-reforming approach for the Case-II and -III (14 × 14 mm^2 reference ASC), i-V curves could not be given because of divergence of calculation. These comparisons emphasized that CFD calculations incorporating the ANN/FIS-based MMR model can provide meaningful and realistic estimations at arbitrary operating conditions.

4.5 Conclusions

With the aim of achieving a powerful numerical tool to find an optimal operating condition and a cell design for the stable operation of DIR-SOFCs fuelled by biogas, a comprehensive CFD model composed of the following sub-models was developed .

- Gas convections in free-spaces of channels and porous electrodes were expressed by Navier-Stokes equations and Brinkmann equations, respectively.
- Mass diffusion in porous electrodes was described by Stefan-Maxwell model.
- The consumption and production rates of gaseous species involved in the simultaneous dry and steam reforming of CH_4 (methane multiple-reforming) in the anode were estimated by ANN/FIS-based model developed in Chapter 3.
- Electromotive force and current density were calculated with Nernst equation and nonlinear Butler-Volmer equation, respectively, with the assumption that H_2 is the predominant reactant for generating electricity as demonstrated in Chapter 2.
- Closed-circuit calculations were conducted using Kirchhoff's law and Ohm's law.
- Temperature filed was determined by general heat transfer equation in conjunction with Fourier's law.

The consistency of the MMR-model-incorporated CFD calculation with the measured performance of DIR-SOFC fuelled by CH_4-CO_2 mixture was confirmed through a three-step model validation process consisting of two model-parameter-tuning steps, model fitting steps with the data experimentally obtained under non-DIR and DIR operations, followed by a validity check whether the established-model can reproduce a performance of DIR-SOFC under an arbitrary operating condition. The ANN/FIS-based MMR model developed in this study can express the complex internal reforming behavior of Ni-YSZ anode during operation. Compared to conventional approaches in literature considering MMR as a sum of CH_4 dry and steam reforming (ignoring the concurrent effect of CO_2 and H_2O on the catalytic CH_4 conversion), the CFD model developed in this study was proved

to be able to provide more reliable and meaningful estimation on behavior of internal reforming SOFCs at any operating conditions.

Using the developed comprehensive CFD model of DIR-SOFC considering MMR, further numerical analyses will be conducted and presented in Chapter 5 for the advanced DIR concepts to control the internal reforming reaction.

References

[1] R. Bove, S. Ubertini, Modeling Solid Oxide Fuel Cell: Methods, Procedures and Techniques, Springer, Netherlands, 2008.

[2] B.A. Haberman, J.B. Young, Three-dimensional simulation of chemically reacting gas flows in the porous support structure of an integrated-planar solid oxide fuel cell, Int. J. Heat Mass Transfer 47 (2004) 3617–3629.

[3] T. Yonekura, Y. Tachikawa, T. Yoshizumi, Y. Shiratori, K. Ito, K. Sasaki, Exchange current density of solid oxide fuel cell electrodes, ECS Transactions 35(1) (2011) 1007–1014.

[4] V.M. Janardhanan, O. Deustchmann, Numerical study of mass and heat transport in solid-oxide fuel cells running on humidified methane, Chem. Eng. Sci. 62 (2007) 5473–5486.

[5] S.P. Jiang, Y. Ramprakash, H_2 oxidation on Ni/Y-TZP cermet electrodes – polarization behavior, Solid State Ionics 116 (1999) 145–156.

[6] S. Nagata, A. Momma, T. Kato, Y. Kasuga, Numerical analysis of output characteristics of tubular SOFC with internal reformer, J. Power Sources 101 (2001) 60–71.

[7] Y. Mizutani, M. Tamura, M. Kawai, O. Yamamoto, Development of high-performance electrolyte in SOFC, Solid State Ionics 72 (1994) 271–275.

[8] E. Achenbach, Three-dimensional and time-dependent simulation of a planar solid oxide fuel cell stack, J. Power Sources 49 (1994) 333–348.

[9] H. Yakabe, T. Ogiwara, M. Hishinuma, I. Yasuda, 3-D model calculation for planar SOFC, J. Power Sources 102 (2001) 144–154.

[10] P. Aguiar, C.S. Adjiman, N.P. Brandon, Anode-supported intermediate temperature direct internal reforming solid oxide fuel cell. I: model-based steady-state performance, J. Power Sources 138 (2004) 120–136.

[11] J.M. Klein, Y. Bultel, S. Georges, P. Pons, Modeling of a SOFC fuelled by methane: From direct internal reforming to gradual internal reforming, Chem. Eng. Sci. 62 (2007) 1636–1649.

[12] K. Nikooyeh, A.A. Jeje, J.M. Hill, 3D modeling of anode-supported planar SOFC with internal reforming of methane, J. Power Sources 171 (2007) 601–609.

[13] C.O. Colpan, I. Dincer, F. Hamdullahpur, Thermodynamic modeling of direct internal reforming solid oxide fuel cells operating with syngas, Int. J. Hydrogen Energy 32 (2007) 787–795.

[14] T.X. Ho, P. Kisinski, A.C. Hoffmann, A. Vik, Transport, chemical and electrochemical processes in a planar solid oxide fuel cell: Detailed three-dimensional modeling, J. Power Sources 195 (2010) 6764–6773

[15] H. Iwai, Y. Yamamoto, M. Saito, H. Yoshida, Numerical simulation of intermediate-temperature direct-internal-reforming planar solid oxide fuel cell, Energy 36 (2011) 2225–2234.

[16] O. Razbani, M. Assadi, M. Andersson, Three-dimensional CFD modeling and experimental validation of an electrolyte supported solid oxide fuel cell fed with methane-free biogas, Int. J. Hydrogen Energy 38 (2013) 10068–10080.

[17] E. Vakouftsi, G.E. Marnellos, C. Athanasiou, F. Coutelieris, CFD modeling of a biogas fuelled SOFC, Solid State Ionics 192 (2011) 458–463.

[18] F.E. Blancas, I.B. Celik, V.R. Hernandez, A.H. Guerrero, J.M.R. Avila, Numerical modeling of SOFCs operating on biogas from biodigesters, Int. J. Hydrogen Energy 28 (2013) 377–384.

[19] K. Girona, J. Laurencin, J. Fouletier, F. Lefebvre-Joud, Carbon deposition in CH_4/CO_2 operated SOFC: Simulation and experimentation studies, J. Power Sources 210 (2012) 381–391.

[20] Meng Ni, Is steam addition necessary for the landfill gas fueled solid oxide fuel cells?, Int. J. Hydrogen Energy 38 (2013) 16373–16386.

[21] N. Gokon, Y. Osawa, D. Nakazawa, T. Kodama. Kinetics of CO_2 reforming of methane by catalytically activated metallic foam absorber for solar receiver-reactors, Int. J. Hydrogen Energy 34(4) (2009) 1787–1800.

CHAPTER 5

Advanced DIR concepts for SOFCs operating with biogas

In order to improve thermo-mechanical stability and enhance output power of DIR-SOFCs operating with biogas, internal reforming rates have to be properly controlled. In this Chapter, two DIR concepts with gas-barrier mask and in-cell reformer are numerically investigated by using the comprehensive CFD model of SOFC considering the simultaneous dry and steam reforming of CH_4 discussed in Chapter 4.

5.1 Introduction

The aim of this study is to numerically evaluate the effectiveness of the proposed DIR concepts for biogas mixtures. Fig. 5.1-(a) shows a schematic of single anode-supported cell (ASC) where CH_4 reforming within the anode substrate is uncontrolled (hereafter called Normal). Fig. 5.1-(b) illustrates a concept with a patterned gas-barrier mask (made from dense yttria-stabilized zirconia (YSZ)) sintered on the anode surface (Concept-I). Depending on the mask pattern, mass fluxes of the reactant gases into the porous anode, in other words, the internal reforming rate can be controlled. In this study, the coverages of the gas-barrier mask were set to 66.7%, 50%, 33.3% and 0% for the 1st, 2nd, 3rd and 4th quarters, respectively, along fuel flow direction. Fig. 5.1-(c) shows an in-cell reformer concept (Concept-II). A sheet of Ni-loaded paper-structured catalyst (PSC) [1] is placed on the anode.

For each case in Fig. 5.1, two types of ASC (Ni-YSZ) that have electrolyte thickness (d_e) of 5 μm and cathode thickness (d_c) of 60 μm but different anode thicknesses (d_a) of 950 (ASC-A) and 200 μm (ASC-B) were considered.

The comprehensive CFD model of DIR-SOFC considering MMR developed in this study (Chapter 4) was used in this evaluation. In Concept-I, the 5 μm-thick gas-barrier mask (patterned YSZ layer) was applied on the anode surface (see Fig. 5.1-(b)). The impact of the gas-barrier mask on collecting current was not considered. In Concept-II, the volume of the fuel channel (1 mm in height) was filled with a Ni-loaded PSC-sheet having porosity of 90%. Component materials of PSC and SOFC were assumed to be homogeneous and

isotropic. Physical parameters of the PSC and the SOFC components are listed in Tables 3.2 and 4.4, respectively.

	Schematic illustration	Photograph
(a)	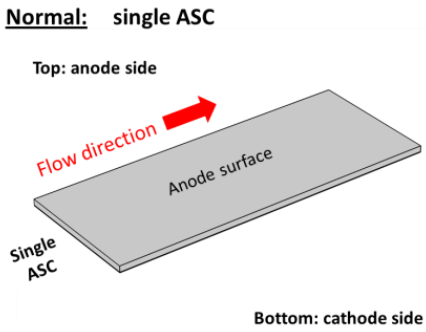	
(b)	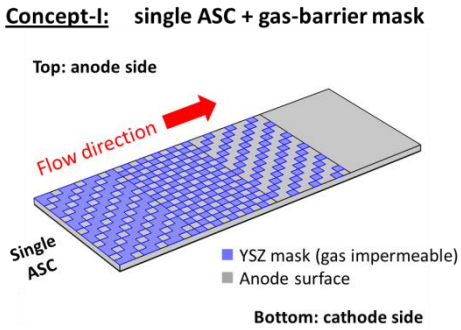	
(c)	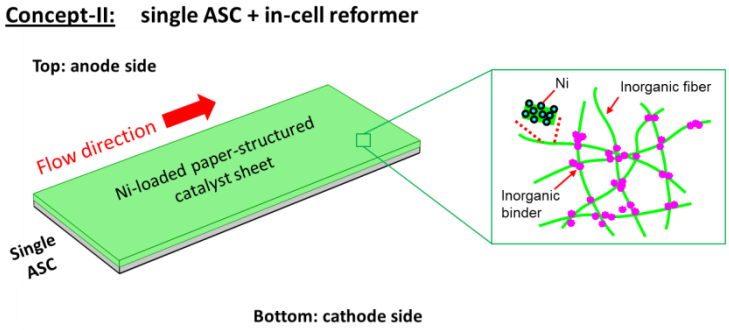	

Fig. 5.1: Schematic illustrations and photographs of DIR-concepts studied in this study.

Initial system temperature and pressure were set to 800 ^{o}C and 1 atm, respectively. CH_4/CO_2 = 1 mixture (800 ^{o}C) was fed to the fuel channel at total molar flow rate in a

range from 2.73×10^{-5} to 1.36×10^{-4} mol s^{-1}, equivalent to volume flow rate (f_{fuel}) in a range of 40–200 mL min^{-1} at 25 ^{o}C. On the other hand, 2.73×10^{-3} mol s^{-1} of N_2/O_2 = 79/21 mixture (800 ^{o}C) was supplied to the air channel.

5.2 Results and discussion

For the proposed DIR concepts (Concept-I and II) with ASC-A and ASC-B, CH_4 conversion, temperature distribution and thermally-induced stresses under open-circuit and load conditions with f_{fuel} = 200 mL min^{-1} were investigated, then, a proper design was discussed.

5.2.1 Case study for the thick anode substrate (ASC-A, d_a = 950 μm)

CH_4 conversion under open-circuit condition

Fig. 5.2 presents the profiles of the calculated r_{CH_4} along fuel flow direction for the ASC-A under open-circuit condition with the feed of 200 mL min^{-1} simulated biogas (CH_4/CO_2 = 1 mixture). Here, the CH_4 conversion in the free-space of the fuel channel was neglected. In the Normal ((a)), CH_4 conversion takes place only in the anode. Maximum r_{CH_4} of about 466 μmol cm^{-3} s^{-1} occurred at the fuel inlet region because of the highest p_{CH_4} and p_{CO_2}, and towards downstream, r_{CH_4} decreased due to the drops of p_{CH_4} and p_{CO_2}. r_{CH_4} decreased from the surface of the anode towards the anode/electrolyte interface, reflecting mass transport limitation of gaseous species within the porous domain.

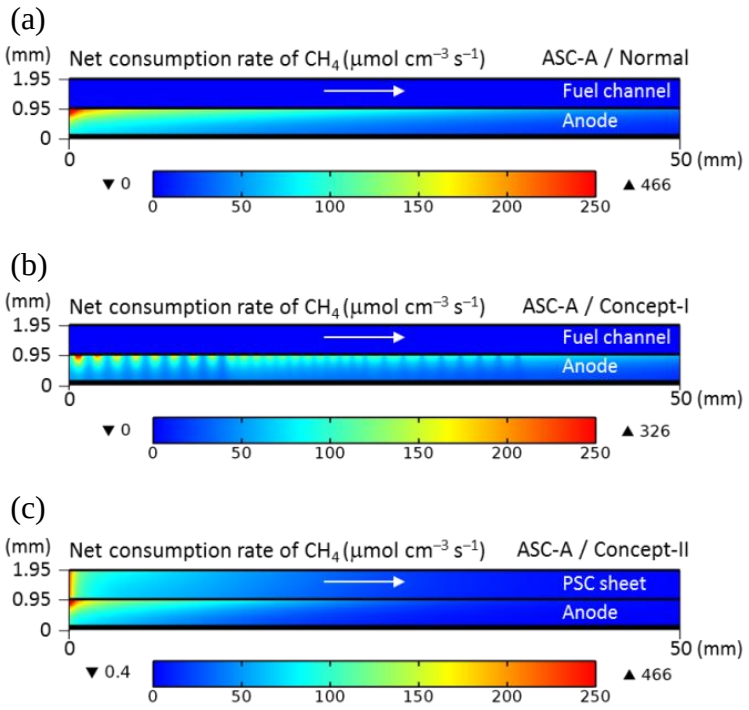

Fig. 5.2: Calculated net consumption rate of CH_4 (r_{CH_4}) for the cases of (a) Normal, (b) Concept-I and (c) Concept-II with ASC-A under open-circuit condition at 800 °C with the feed of 200 mL min^{-1} simulated biogas (CH_4/CO_2 = 1 mixture). ▼ and ▲ in (a)–(c) indicate the minimum and maximum values of r_{CH_4}, respectively.

By applying the gas-barrier mask (Concept-I), mass fluxes of CH_4 and CO_2 entering the porous anode at the fuel inlet side were suppressed, and hence, the maximum r_{CH_4} was reduced to 326 μmol cm^{-3} s^{-1} to have partially equalized r_{CH_4} along fuel flow direction (see Fig. 5.2-(b)). Total CH_4 conversion (χ_{CH_4}) was 78.4% at the fuel outlet for the Concept-I, which was 8.2% less than that for the Normal. In the case of Concept-II, the catalytically-active surface area was significantly increased to remarkably enhance the r_{CH_4} at the fuel inlet region (see Fig. 5.2-(c)), resulting in χ_{CH_4} of 99% (47 and 52% in the 950 μm-thick anode substrate and the 1000 μm-thick PSC, respectively). As a result, the mole fractions of CH_4 and H_2 more rapidly dropped and rose, respectively, compared to the Normal and Concept-I (see Fig. 5.3).

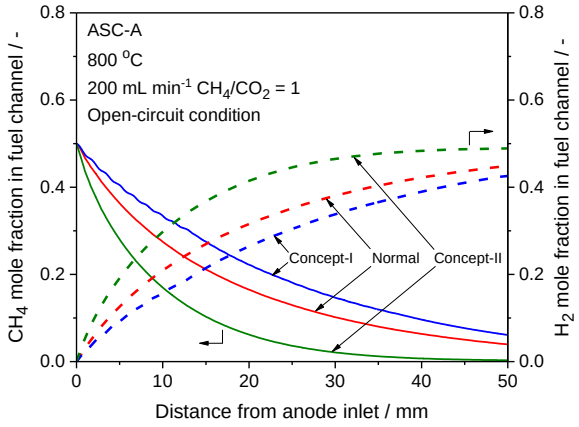

Fig. 5.3: Profiles of CH_4 and H_2 mole fractions in fuel channel along fuel flow direction for the cases of Normal, Concept-I and -II calculated for ASC-A under open-circuit condition at 800 °C with the feed of 200 mL min^{-1} simulated biogas (CH_4/CO_2 = 1 mixture).

Temperature distribution and thermally-induced stresses under open-circuit condition

Due to the endothermicity of CH_4 reforming, temperature drop and inhomogeneous temperature distribution within the ASC-A were confirmed as shown in Figs. 5.4-(a)–(c). With the feed of 200 mL min^{-1} simulated biogas (CH_4/CO_2 = 1 mixture), for the Normal, the maximum temperature drop in the electrolyte ($\Delta T_{e,max}$) was 66 °C at the anode inlet region (see Fig. 5.4-(d)), resulting in the maximum thermally-induced stress (first principal stress ($\sigma_{e,max}^{T}$)) of 167 MPa.

In comparison with the Normal, 26% smaller $\Delta T_{e,max}$ and more homogeneous temperature distribution resulting in 21% smaller $\sigma_{e,max}^{T}$ can be achieved with Concept-I. On the other hand, Concept-II led to severer temperature drop and steeper temperature gradient along fuel flow direction since almost CH_4 in the fuel stream was converted to syngas within the first half of the cell length. Consequently, $\Delta T_{e,max}$ and $\sigma_{e,max}^{T}$ rose 18.2 and 13.8%, respectively, compared to the Normal.

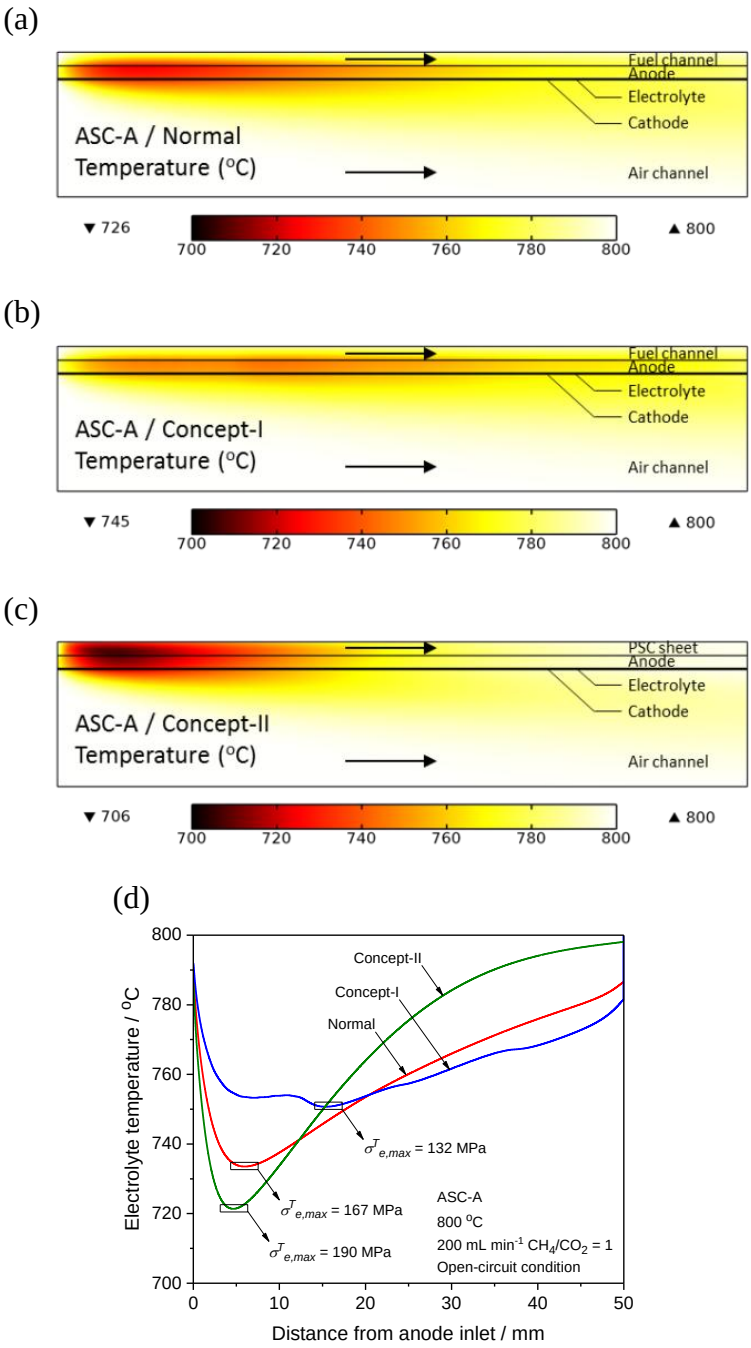

Fig. 5.4: Calculated temperature distribution for the cases of (a) Normal, (b) Concept-I and (c) Concept-II with ASC-A, and (d) the profiles of electrolyte temperature along fuel flow direction under open-circuit condition at 800 ^{o}C with the feed of 200 mL min^{-1} simulated biogas (CH_4/CO_2 = 1 mixture). ▼ and ▲ in (a)–(c) indicate the minimum and maximum temperatures, respectively. Rectangles in (d) indicate the positions where the maximum thermally-induced stress (first principal stress ($\sigma^T_{e,max}$)) occurs.

Power generation characteristics

Current-voltage (I-V) characteristics of the ASC-A for the three cases are plotted in Fig. 5.5. Below 1 A cm^{-2} (fuel utilization (U_f) < 20%), power densities were comparable since the impact of concentration losses are insignificant and cell voltage drop is mainly related to activation and ohmic overvoltages. Further increasing current density, differences became noticeable. Maximum power density (P_{max}) increased in the order of Concept-I (1.08 W cm^{-2}), Normal (1.17 W cm^{-2}) and Concept-II (1.25 W cm^{-2}), reflecting the order of the syngas production rate mentioned in the previous part. In Concept-II, WGS reaction promoted within the PSC-sheet readily shifts CO to H_2 under high current density. This also contributes to the power enhancement.

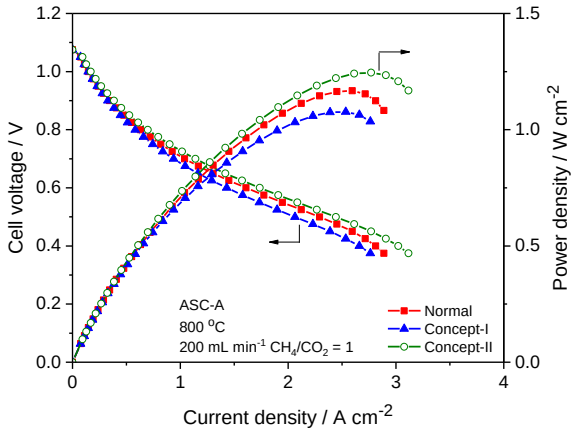

Fig. 5.5: Calculated I-V characteristics for the cases of Normal, Concept-I and -II with ASC-A at 800 °C with the feed of 200 mL min^{-1} simulated biogas (CH_4/CO_2 = 1 mixture).

Proper design for ASC-A

Fig. 5.6 shows the CH_4 conversion (χ_{CH_4}) of internal dry reforming at 800 °C under open-circuit condition for the cases of the Normal, Concept-I and Concept-II. In the f_{fuel} range of 40–120 mL min^{-1}, χ_{CH_4} > 90% close to equilibrium (95.8%) were obtained. Although χ_{CH_4} for the three concepts were comparable, it should be mentioned that the rate

of H_2 production within the fuel inlet region increased in the order of Concept-I, Normal and Concept-II as discussed above. Further increase of f_{fuel} to 200 mL min^{-1}, χ_{CH_4} for the Normal and Concept-I reduced to about 80% because CH_4 conversion was kinetically limited, whereas that for Concept-II did not decrease even with high fuel flow rate over 120 mL min^{-1} due to the positive effect of PSC to promote syngas production (see Fig. 5.7).

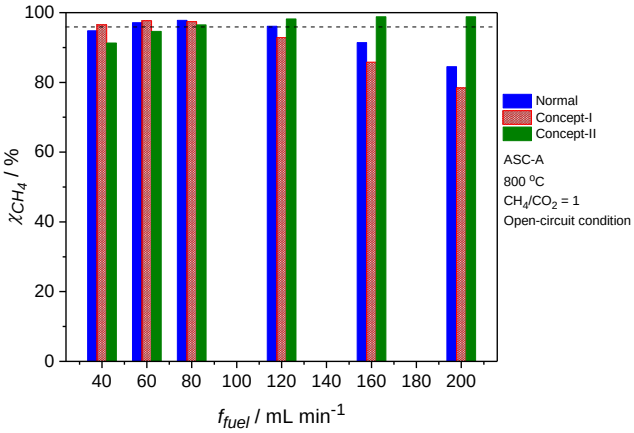

Fig. 5.6: Calculated CH_4 conversion (χ_{CH_4}) of internal dry reforming (Fuel: CH_4/CO_2 = 1 mixture) for the cases of Normal, Concept-I and -II with ASC-A at 800 °C under open-circuit condition in the f_{fuel} range of 40–200 mL min^{-1}. Dash line indicates χ_{CH_4} calculated at equilibrium condition.

(a)

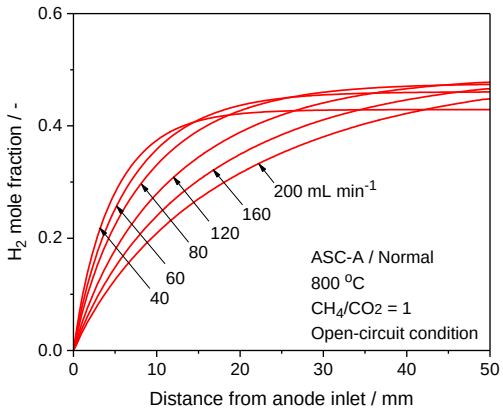

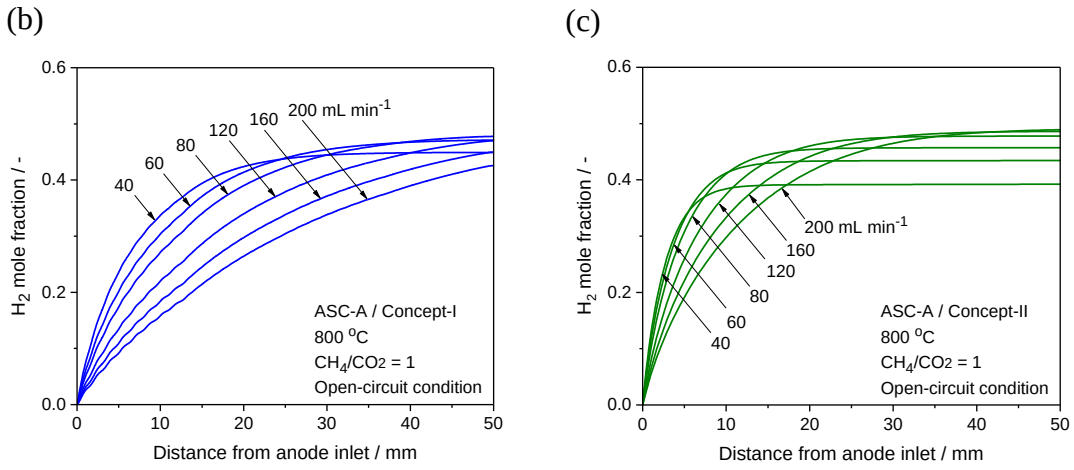

Fig. 5.7: Profiles of H_2 mole fractions in fuel channel along fuel flow direction for the cases of (a) Normal, (b) Concept-I and (c) Concept-II calculated for ASC-A at 800 ^{o}C under open-circuit condition in the f_{fuel} range of 40–200 mL min^{-1}.

Figs. 5.8 shows the profiles of electrolyte temperature along fuel flow direction for the proposed DIR concepts at 800 ^{o}C under open-circuit condition for different f_{fuel}. As f_{fuel} increased from 40 to 200 mL min^{-1}, the Normal ((a)) resulted in $\Delta T_{e,max}$ varying from –41 to –66 ^{o}C. For the Concept-I with gas barrier-mask ((b)), more homogeneous electrolyte temperature distribution could be obtained. $\Delta T_{e,max}$ was drastically reduced, –31 and –49 ^{o}C at 40 and 200 mL min^{-1}, respectively. For the Concept-II ((c)), syngas production was accelerated in the first half of the anode substrate, generating steeper temperature gradient with $\Delta T_{e,max}$ of –45 and –79 ^{o}C at 40 and 200 mL min^{-1}, respectively.

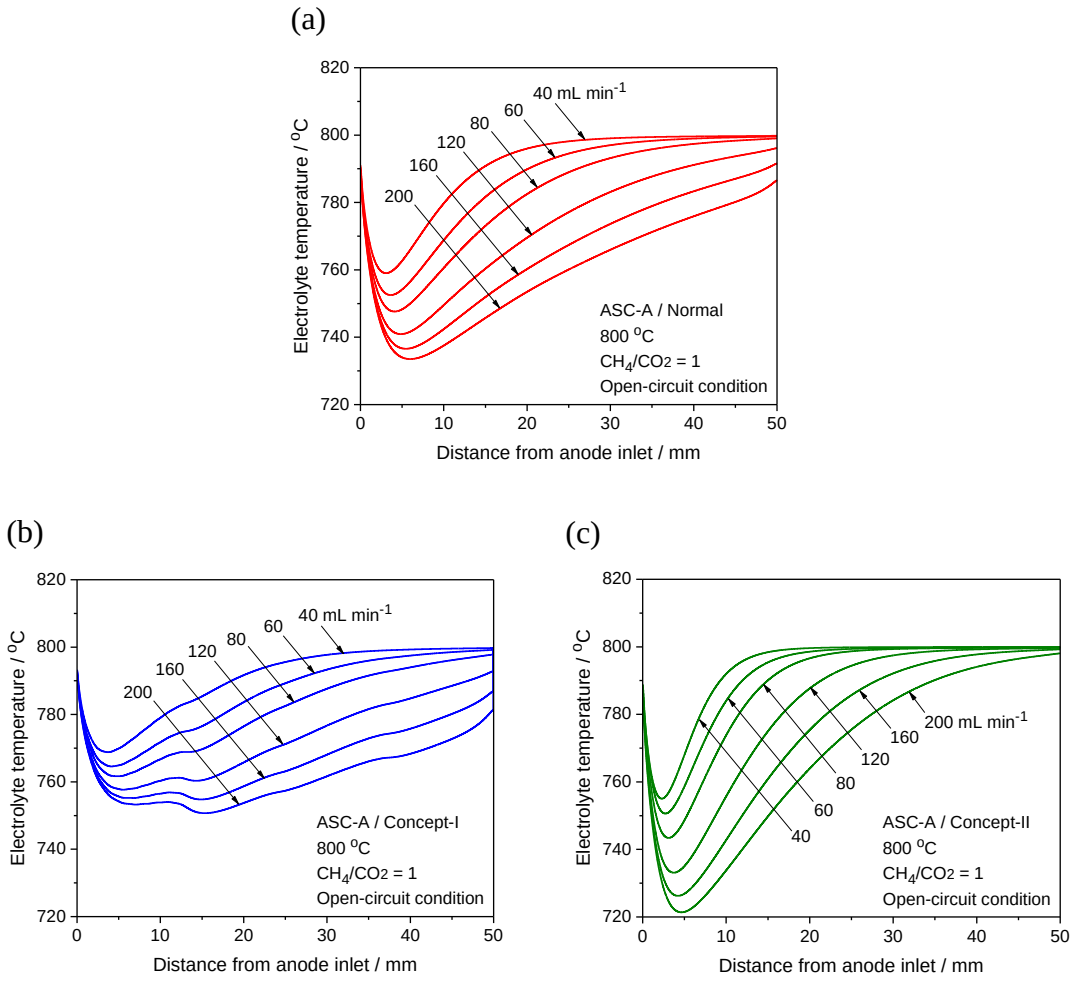

Fig. 5.8: Calculated profiles of electrolyte temperature along fuel flow direction for the cases of (a) Normal, (b) Concept-I and (c) Concept-II with ASC-A under open-circuit condition at 800 °C in the f_{fuel} range of 40–200 mL min^{-1}.

Maximum thermally-induced stress, $\sigma_{e,max}^{T}$, under open-circuit condition was plotted in Fig. 5.9. $\sigma_{e,max}^{T}$ for the Concept-I was 20 % smaller compared to the Normal at the same f_{fuel}, in contrast, 8–14% higher $\sigma_{e,max}^{T}$ was generated for the Concept-II. Although, the estimated $\sigma_{e,max}^{T}$ values were lower than the fracture strength of YSZ (reported as 236 MPa [2]) for all cases, Concept-I was confirmed to be effective to suppress the risk of electrolyte fracture during DIR operation.

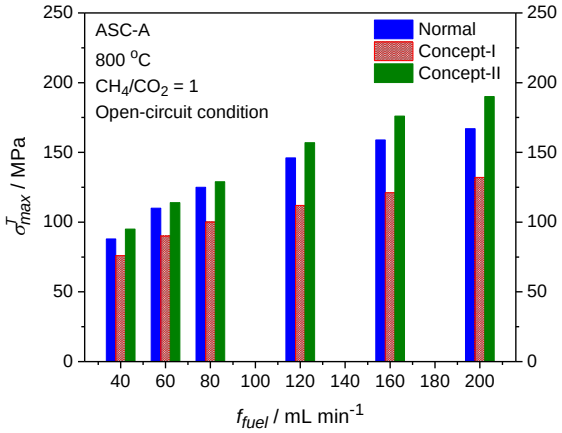

Fig. 5.9: Calculated maximum thermally-induced stress ($\sigma^T_{e,max}$) for the cases of Normal, Concept-I and -II with ASC-A under open-circuit condition at 800 °C in the f_{fuel} range of 40–200 mL min^{-1}.

Fig. 5.10 shows the maximum power density, P_{max}, and corresponding fuel utilization ($U_{f,P_{max}}$) estimated for Normal, Concept-I and Concept-II with the ASC-A at 800 °C. In the f_{fuel} range of 40–80 mL min^{-1}, P_{max} for the three concepts were comparable and increased with increasing f_{fuel} even under $U_{f,P_{max}}$ > 70%, indicating that, in this f_{fuel} region, concentration losses are negligibly small for all cases. Further increase of f_{fuel} to 200 mL min^{-1}, whereas P_{max} for Normal and Concept-II continuously increased, for the Concept-I it was converged.

For the 20 × 50 mm^2 ASC with a 950 μm-thick anode substrate (Normal), χ_{CH_4} was over 80% for all f_{fuel} being studied, and hence, the positive impact of in-cell reformer (Concept-II) on the power enhancement was not pronounced (< 7%). For the stable operation at $U_{f,P_{max}}$ > 70 %, Concept-I is considered to be a good choice due to comparable P_{max} to other concepts (see Fig. 5.10) and lower risk of electrolyte fracture (see Fig. 5.9).

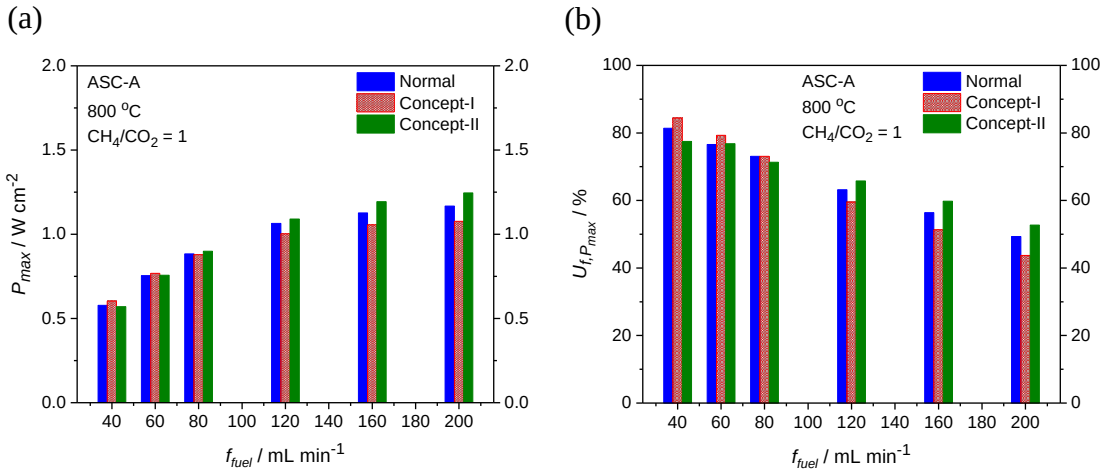

Fig. 5.10: Maximum power density, P_{max}, ((a)) for the cases of Normal, Concept-I and -II calculated for ASC-A under open-circuit condition at 800 °C in the f_{fuel} range of 40–200 mL min^{-1}. (b) is the fuel utilization at P_{max} ($U_{f,P_{max}}$).

There are many approaches in literature to improve thermo-mechanical stability of DIR SOFC such as increasing Ni particle size [3], partially blocking catalytically-active surface with alkaline earth metals [4, 5], substitution of Ni with Cu [6, 7], and controlling mass transport by an additional thick chemically-inert diffusion-layer on the anode surface [8, 9]. However, these technical approaches resulted in the significant reduction of output power. Obviously, the thin gas-barrier layer (Concept-I) in this study is significantly effective and can be adopted for practical applications.

5.2.2 Case study for the thin anode substrate (ASC-B, d_a = 200 μm)

For the ASC-B with thinner anode substrate running with the feed of 200 mL min^{-1} simulated biogas (CH_4/CO_2 = 1 mixture) at 800 °C, as shown in Fig. 5.11-(a), the profile of H_2 mole fraction of Concept-I was comparable to the Normal, and χ_{CH_4} at the anode outlet was 54% similar to 58% for the Normal. Within the first 20 mm of the cell length, the decreasing rate of CH_4 mole fraction of Concept-I was lower than that of the Normal, indicating the suppression of maximum r_{CH_4} with Concept-I, which resulted in more homogenous distribution of the electrolyte temperature than the Normal (see Fig. 5.11-(b))

to have 20% smaller $\sigma_{e,max}^{T}$ (= 88 MPa) in comparison to the Normal (110 MPa). With Concept-II, χ_{CH_4} was remarkably boosted to about 96% (26 and 70% in the 200 μm-thick anode substrate and the 1000 μm-thick PSC, respectively). As a result, the H_2 mole fraction was considerably higher than those with the Normal and Concept-I, potentially providing the enhancement of electrochemical performance.

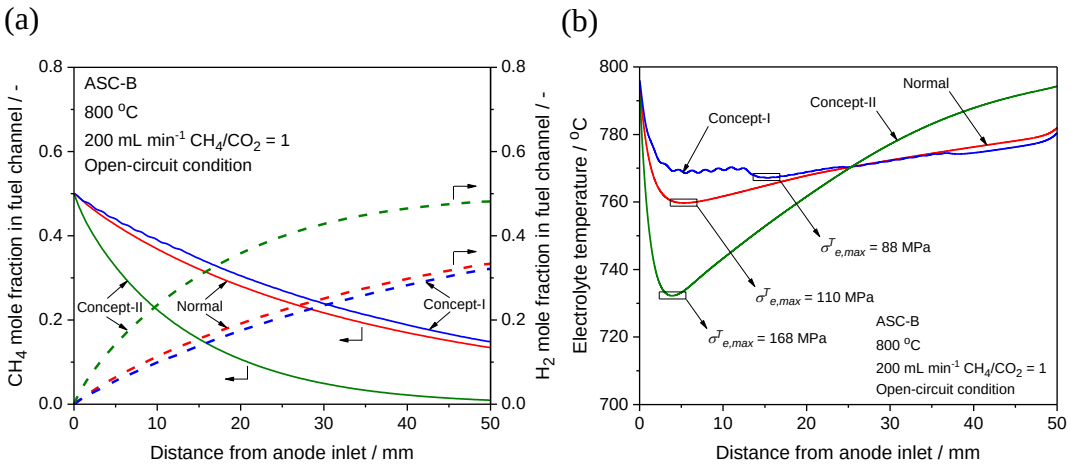

Fig. 5.11: Profiles of (a) CH_4 and H_2 mole fractions and (b) electrolyte temperature along fuel flow direction under open-circuit condition at 800 °C with the feed of 200 mL min^{-1} simulated biogas (CH_4/CO_2 = 1 mixture) calculated for ASC-B. Rectangles in (b) indicate the positions where the maximum thermally-induced stress (first principal stress ($\sigma_{e,max}^{T}$)) occurs.

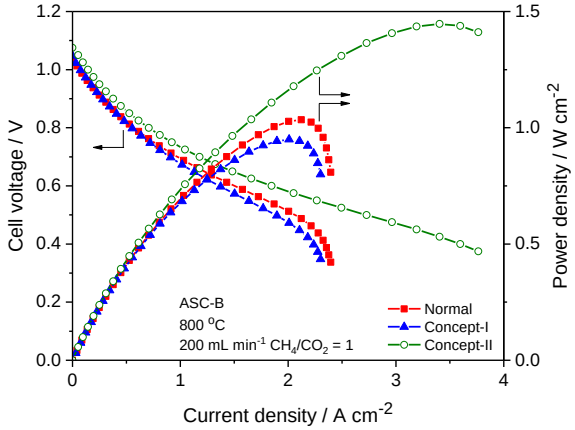

Fig. 5.12: Calculated *I-V* characteristics of ASC-B at 800 °C with the feed of 200 mL min^{-1} simulated biogas (CH_4/CO_2 = 1 mixture).

Power generation characteristics for the three cases with ASC-B were plotted in Fig. 5.12. P_{max} of 1.45 W cm^{-2} for the Concept-II was 41 and 53% higher than those for the Normal and Concept-I, respectively, due to remarkably higher p_{H_2} by the promotion of reforming reaction with Concept-II (see Fig. 5.11-(a)).

Proper design for ASC-B

Fig. 5.13 shows the χ_{CH_4} of internal dry reforming at 800 ^{o}C under open-circuit condition for the cases of the Normal, Concept-I and Concept-II. For the Normal and Concept-I, χ_{CH_4} monotonically decreased from about 90% to less than 60 % with increasing f_{fuel}, indicating that the reforming kinetics becomes the rate determining process. On the other hand, Concept-II exhibited χ_{CH_4} of over 90 % for the whole range of f_{fuel}, showing the considerable contribution of the in-cell reformer (here, PSC) in syngas production (see Figs. 5.13 and 5.14).

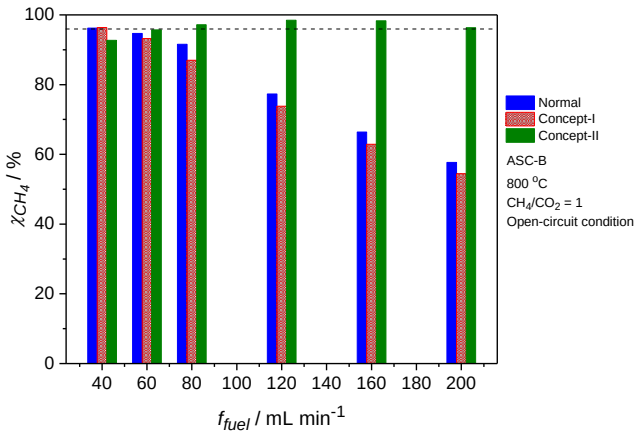

Fig. 5.13: Calculated CH_4 conversion (χ_{CH_4}) of internal dry reforming (Fuel: CH_4/CO_2 = 1 mixture) for the cases of Normal, Concept-I and -II with ASC-B at 800 ^{o}C under open-circuit condition in the f_{fuel} range of 40–200 mL min^{-1}. Dash line indicates χ_{CH_4} calculated at equilibrium condition.

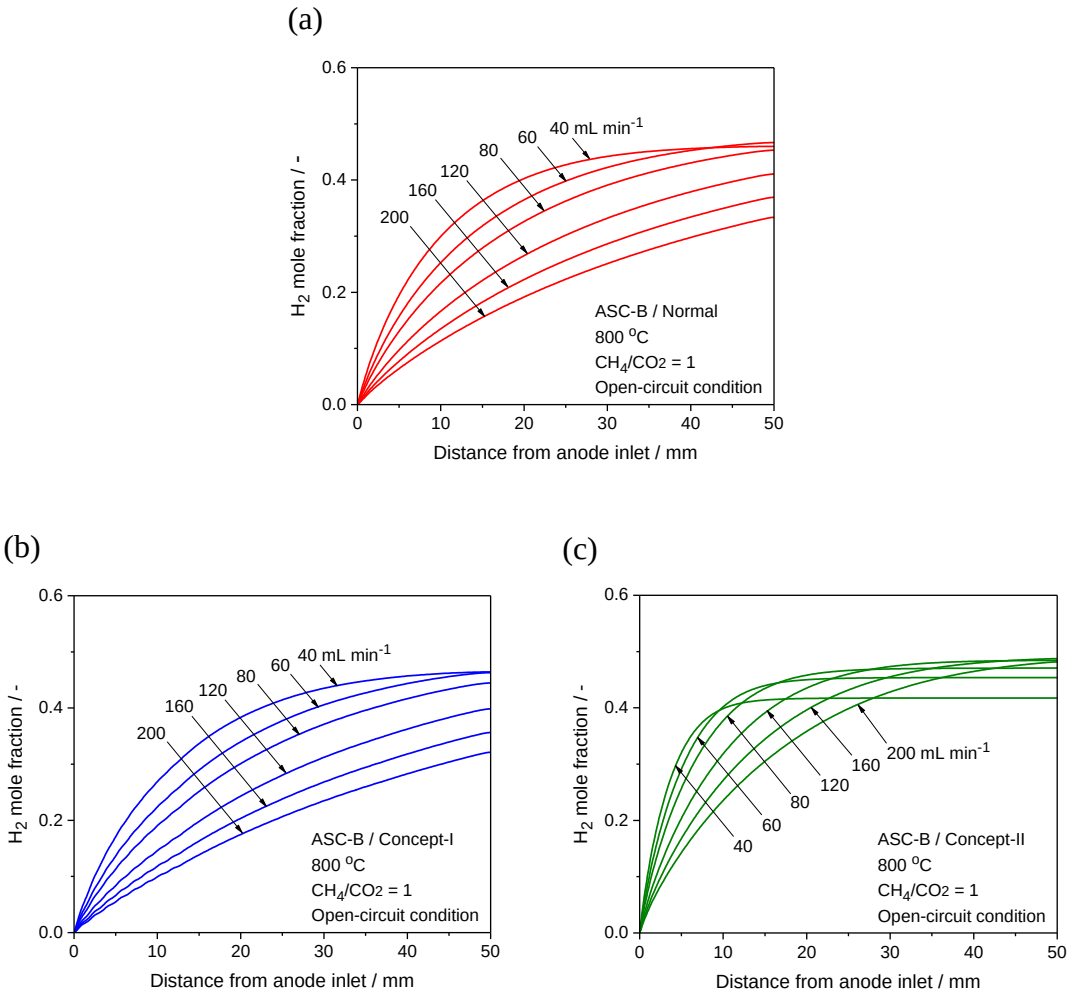

Fig. 5.14: Profiles of H_2 mole fractions in fuel channel along fuel flow direction for the cases of (a) Normal, (b) Concept-I and (c) Concept-II calculated for ASC-B at 800 °C under open-circuit condition in the f_{fuel} range of 40–200 mL min^{-1}.

In the case of Concept-I, again, temperature distribution in the electrolyte became more homogeneous compared to the Normal, resulting in smaller $\Delta T_{e,max}$ (compare Figs. 5.15-(a) and (b)) and 20–25 % less $\sigma_{e,max}^{T}$ (see Fig. 5.16). Concept-II caused larger $\Delta T_{e,max}$ with steeper electrolyte temperature gradient than the other DIR concepts (see Fig. 5.15-(c)), leading to noticeably higher $\sigma_{e,max}^{T}$ (see Fig. 5.16).

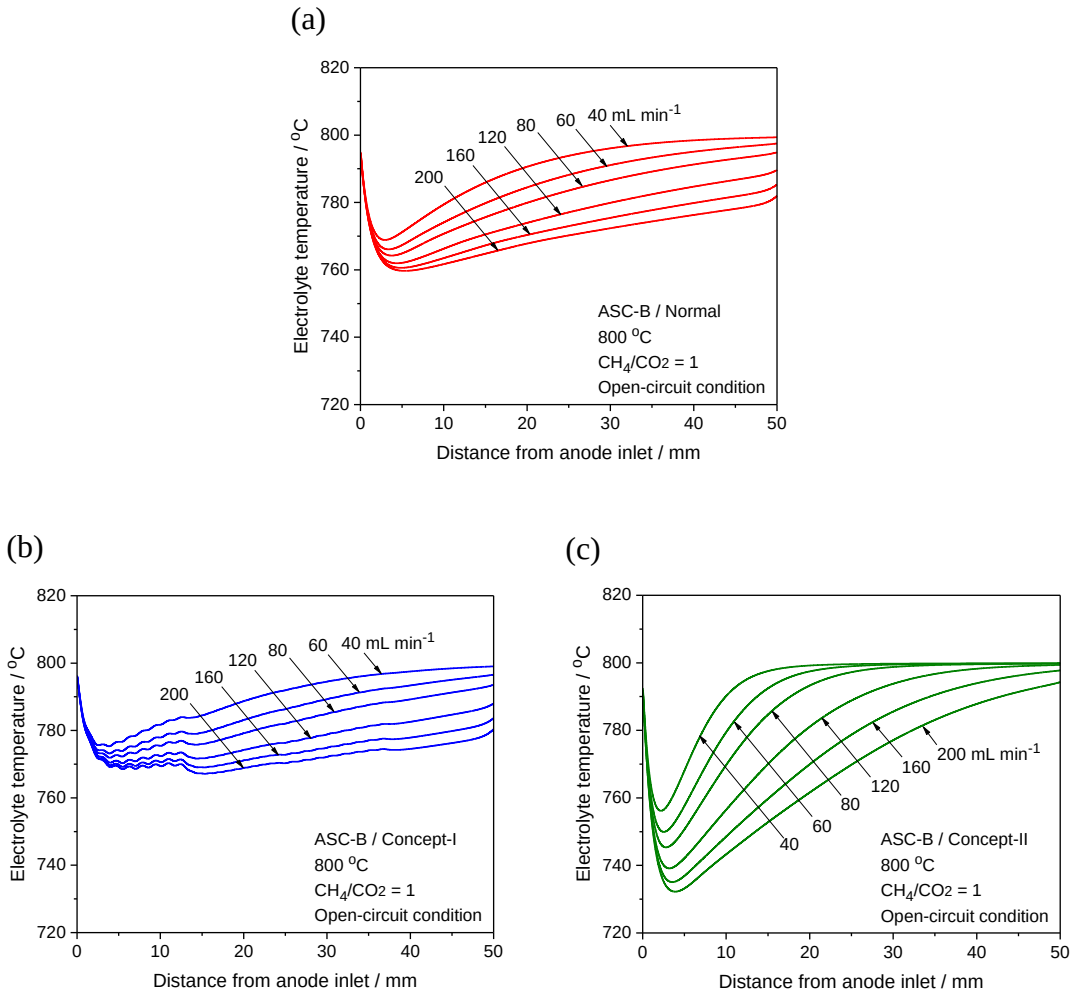

Fig. 5.15: Calculated profiles of electrolyte temperature along fuel flow direction for the cases of (a) Normal, (b) Concept-I and (c) Concept-II with ASC-B under open-circuit condition at 800 °C in the f_{fuel} range of 40–200 mL min^{-1}.

Due to the higher syngas production rate (see Fig. 5.14), Concept-II is superior to the Normal and Concept-I in terms of power generation at f_{fuel} > 80 mL min^{-1} (see Fig. 5.17-(a)), increasing fuel utilization of the cell (see Fig. 5.17-(b)). For the thin anode substrate, in spite of higher $\sigma_{e,max}^{T}$, Concept-II with in-cell reformer was proved to be effective for elevating power generation.

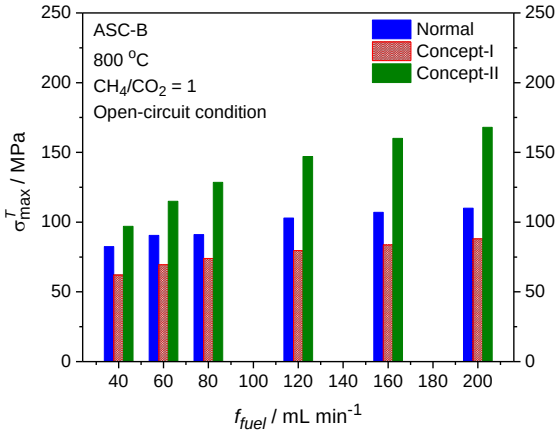

Fig. 5.16: Calculated maximum thermally-induced stress ($\sigma_{e,max}^{T}$) for the cases of Normal, Concept-I and -II with ASC-B under open-circuit condition at 800 °C in the f_{fuel} range of 40–200 mL min^{-1}.

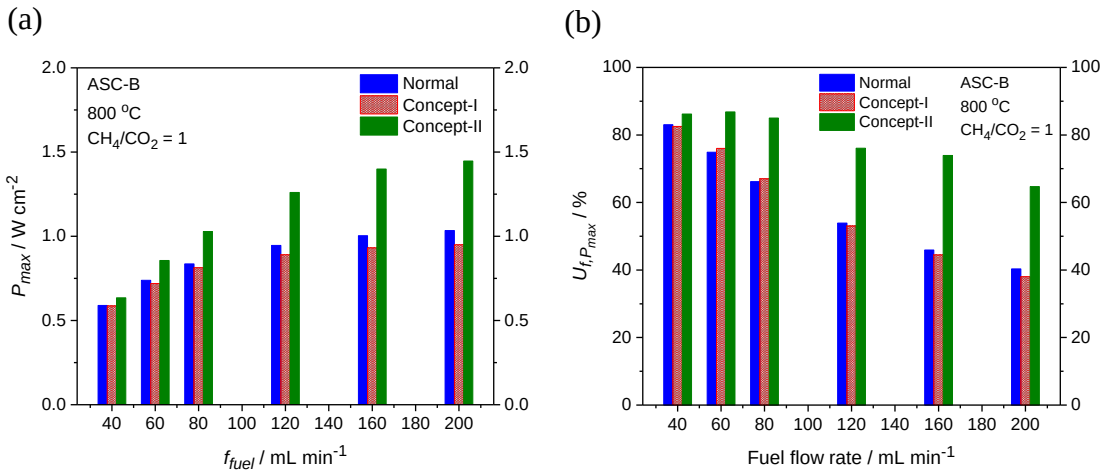

Fig. 5.17: Maximum power density, P_{max}, ((a)) for the cases of Normal, Concept-I and -II calculated for ASC-B under open-circuit condition at 800 °C in the f_{fuel} range of 40–200 mL min^{-1}. (b) is the fuel utilization at P_{max} ($U_{f,P_{max}}$).

5.2.3 Effect of anode thickness

With the feed of 200 mL min – 1 simulated biogas (CH_4/CO_2 = 1 mixture), as shown in Fig. 5.18, in the cases of Normal and Concept-I, P_{max} with thinner anode substrate (ASC-B) became lower than those with thicker one (ASC-A), reflecting that the degree of

catalytic CH_4 conversion is a predominant factor of the performance. Therefore, the application of an additional catalyst layer must have positive impact on the performance enhancement. In fact, for both ASC-A and ASC-B, increase in P_{max} by the application of PSC (Concept-II) was confirmed, however, its effect was more pronounced for the thinner anode substrate (ASC-B). As a result, P_{max} of ASC-B with Concept-II exceeded that of ASC-A with the same concept by 16%. To explain this positive trend, the effect of the anode thickness in Concept-II on the electrochemical performance at the total polarization (V_{pol}) of 0.6 V was described in Fig. 5.19. For the ASC-B with thinner anode substrate, H_2O (product of the anodic reaction) was easily drained out of the anode. As a result, p_{H_2O} build-up within the AFL under high current densities (the decrease in electromotive force) can be suppressed. These results indicate that the anode thickness is an important factor of cell design for the DIR-operation, where P_{max} is governed by both syngas production rate and mass transport limitation.

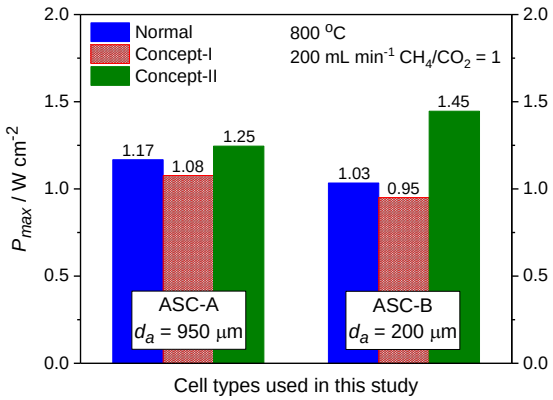

Fig. 5.18: Calculated maximum power densities (P_{max}) at 800 °C with the feed of 200 mL min^{-1} simulated biogas (CH_4/CO_2 = 1 mixture), showing the effects of Concept-I and Concept-II for different thicknesses of anode substrate.

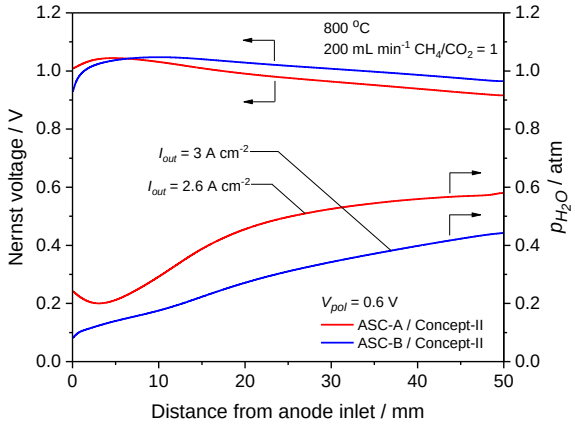

Fig. 5.19: Calculated profiles of Nernst voltage (electromotive force) and p_{H_2O} within the AFL along fuel flow direction at the total polarization (V_{pol}) of 0.6 V for the Concept-II with ASC-A and ASC-B at 800 °C with the feed of 200 mL min^{-1} simulated biogas (CH_4/CO_2 = 1 mixture). I_{out} is the average output current density.

As mentioned in the previous section, to ensure the mechanical stability in the DIR operation, Concept-I was effective, and therefore, the combination of the Concept-I and Concept-II for thinner anode substrate may bring about the best operating condition in terms of both mechanical stability and electrochemical performance.

5.3 Conclusions

Control of internal reforming rate is a key to enhance power generation and improve thermo-mechanical stability of DIR-SOFCs running with biogas. Here, the effects of the anode gas-barrier mask ((Concept-I) shown in Fig. 5.1-(b)) and the in-cell reformer using paper-structured catalyst (PSC) ((Concept-II) shown in Fig. 1-(c)) were numerically evaluated using the CFD model developed in Chapter 4. Two types of 20 × 50 mm^2 ASC (Ni-YSZ) that have electrolyte thickness of 5 μm and cathode thickness of 60 μm but different anode thicknesses (d_a) of 950 (ASC-A) and 200 μm (ASC-B) were considered.

For both types of ASC, Concept-I with gas-barrier mask, which can control mass flux of fuel entering the anode along fuel flow direction, was confirmed to suppress rapid

syngas production within fuel inlet region, leading to homogeneous temperature distribution over the cell. In comparison to normal ASCs (Normal) in which reforming rates are not controlled, about 20% decrease in the maximum thermally-induced stress was estimated with a slight loss (about 8%) of maximum power density, indicating that the use of anode gas-barrier mask is effective to reduce the risk of electrolyte fracture. Concept-I could be a good choice for stable operation under fuel utilizations over 70%, especially for ASC-A with thick anode substrate having high content of Ni catalyst.

Concept-II increases the total catalytically-active surface area, promoting syngas production. At a fuel flow rate of 200 mL min^{-1}, total CH_4 conversion decreased to about 80% and less than 60% for normal ASC-A and -B, respectively, because CH_4 conversion was kinetically limited. On the other hand, those of ASC-A and -B for Concept-II were higher than 90%, by which the maximum power density was boosted by 7 and 40% compared to normal ASC-A and -B, respectively, although the risk of electrolyte fracture was increased. The effect of Concept-II was more pronounced for ASC-B with thin anode substrate having low content of Ni catalyst.

In practical applications, anode thickness (or amount of metallic Ni in anode substrate) is an important factor to select a proper cell design for DIR operation. For ASCs with thick anode substrates, Concept-I is promising approach to achieve stable operation without noticeable drop in power generation. For ASCs with thin anode substrates, application of Concept-II is effective to maximize power density, however elevation of thermal stresses has to be taken into consideration. Requirements of efficiency and mechanical stability may be simultaneously met by a mixed concept of Concept-I and -II (Concept-III) which will be studied in the future work.

References

[1] Y. Shiratori, T. Ogura, H. Nakajima, M. Sakamoto, Y. Takahashi, Y. Wakita, T. Kitaoka, K. Sasaki, Study on paper-structured catalyst for direct internal reforming SOFC fueled by the mixture of CH_4 and CO_2, Int. J. Hydrogen Energy 38 (2013) 10542–10551.

[2] H. Greiner, E. Keim, W. Kleinlein and E. Weiss, in *Proceedings of International Symposium SOFC II*, F. Grosz, P. Zergers, S.C. Singhal and O. Yamamoto, Editors, p. 705, The Electrochemical Society, Pennington, NJ (1991).

[3] D. Mogensen, J.D. Grunwaldt, P.V. Hendriksen, K.D. Johansen, J.U. Nielsen, Internal steam reforming in solid oxide fuel cells: Status and opportunities of kinetic studies and their impact on modeling, J. Power Sources 196 (2011) 25–38.

[4] T. Takeguchi, Y. Kani, T. Yano, R. Kikuchi, K. Eguchi, K. Tsujimoto, Y. Uchida, A. Ueno, K. Omoshiki, M. Aizawa, Study on steam reforming of CH4 and C2 hydrocarbons and carbon deposition on Ni-YSZ cermets, J. Power Sources 112 (2002) 588–595.

[5] R. Kikuchi, K. Eguchi, Solid oxide fuel cell as a multi-fuel applicable power generation device, J. Jpn. Petrol. Inst. 47 (2004) 225–238.

[6] V.V. Krishnan, S. McIntosh, R.J. Gorte, J.M. Vohs, Measurement of electrode overpotentials for direct hydrocarbon conversion fuel cells, Solid State Ionics 166 (1–2) (2004) 191–197.

[7] W. Wang, H. Zhu, G. Yang, H.J. Parl, D.W. Jung, C. Kwak, Z. Shao, A NiFeCu alloy anode catalyst for direct-methane solid oxide fuel cells, J. Power Sources 258 (2014) 134–141.

[8] Y. Lin, Z. Zhan, S.A. Barnett, Improving the stability of direct-methane solid oxide fuel cells using anode barrier layers, J. Power Sources 158 (2006) 1313–1316.

[9] H. Zhu, A.M Colclasure, R.J. Kee, Y. Lin, S.A. Barnett, Ande barrier layers for tubular solid-oxide fuel cells with methane fuel streams, J. Power Sources 161 (2006) 413–419.

CHAPTER 6

Conclusions

6.1 Conclusions

Solid oxide fuel cell (SOFC) is a highly efficient energy conversion device which directly generates electricity through the electrochemical reaction of a fuel with oxygen. SOFC is attributed to all solid state construction (ceramic and metal) and high operating temperature (600–1000 ^{o}C), making it an attractive power generator due to cell/stack design flexibility, multiple fabrication options, multi-fuel capability (H_2, CO, hydrocarbons, etc.), and high quality waste heat. Under the catalytic activity of metallic Ni particles embedded in anode materials, hydrocarbons fed to the anode quickly react with H_2O and CO_2 to produce syngas, H_2 and CO, subsequently electrochemically oxidized at the triple-phase boundary (TPB) of anode to generate electricity and heat. This is called direct internal reforming (DIR) operation by which enhancement of electrical efficiency and system downsizing are expected. Biogas, CH_4-CO_2 mixtures obtained from the anaerobic fermentation of organic matters from garbage, livestock manure and agricultural waste, can thus be used as a direct fuel for SOFCs. Since biogas is considered as one of energy carriers derived from the solar energy, distributed power generators based on biogas-fuelled SOFCs is promising technology for sustainable development, especially in developing countries where H_2 infrastructure is an unrealistic option.

In order to achieve stable DIR operation with biogas, the risk of electrolyte fracture due to the endothermicity of reforming reactions and the degradation of anode performance caused by carbon deposition can simultaneously be suppressed by properly selecting operating conditions such as operating temperature, the degree of fuel humidification (steam-to-carbon (S/C) ratio in fuel stream), and fuel utilization. Numerical simulation is invaluable approach to understand physical and chemical processes occurring within the cell, investigate effectiveness of various cell/stack designs, and evaluate influences of operation parameters on SOFC performance. The estimated results can be applied for optimizing cell/stack designs and operating conditions, as a result, significantly lowering efforts, time and cost for developing SOFC-based power systems. For this purpose, this

study aims to develop a comprehensive computational fluid-dynamics (CFD) model of DIR-SOFC running with biogas coupling mass and heat transport, chemical and electrochemical processes occurring simultaneously within the cell.

Under DIR operation, both H_2 and CO are electrochemically-active species at the TPB. The contribution of each as an active fuel to SOFC power generation with the direct feed of simulated biogas mixtures (CH_4:CO_2:N_2 = 20:f_{CO_2}:(60 − f_{CO_2})) was first investigated. Under open-circuit condition, CH_4 reacted with CO_2 in dry reforming reaction, producing H_2 and CO. Reverse-WGS reaction was promoted with increase of CO_2 flow rate (f_{CO_2}) at a constant CH_4 flow rate (f_{CH_4}). In consequence, the partial pressure of H_2O (by-product of reverse-WGS reaction) was elevated, leading to increase in the concentration of O(Ni), which was produced internally from the dissociation of H_2O on the Ni surface. Oxygen partial pressure in anode side ($p_{O_2,a}$) also increased with increase of oxygen carrier content (here, CO_2) in the fuel stream. Impedance data measured at anode side revealed that both surface diffusion of electrochemically-active species to the TPB and charge-transfer reactions were significantly accelerated with increasing O(Ni) concentration and $p_{O_2,a}$. These electrochemical behaviors were identical with those of Ni-based anodes fuelled by H_2. Because the electrochemical oxidation of CO is known to be suppressed by the presence of H_2O to form O(Ni), it can be concluded that in the DIR operation H_2 is the predominant active fuel for power generation, even though H_2/CO ratio is as low as 0.3. The electrochemical contribution of CO to power generation can thus safely be neglected in numerical calculations of DIR-SOFCs operating with biogas.

Generally, syngas production in biogas-fuelled SOFCs is governed by the simultaneous CH_4 conversions with CO_2 and H_2O (the methane multiple-reforming (MMR) process). Due to its complex kinetics strongly dependent on gas composition and temperature, MMR could not be fully modeled by conventional approaches based on power-law model fitting, first order reaction kinetics related to CH_4 partial pressure and Langmuir-Hinshelwood kinetics. In this study, a complete MMR model, which can calculate the consumption and production rates of gaseous species involved in CH_4 conversion at arbitrary temperatures

and gas compositions (CH_4-CO_2-H_2O-H_2-CO mixtures), was developed using an approximation method adopting Artificial Neural Network (ANN) and Fuzzy Inference System (FIS). The MMR process in Ni-based SOFC anodes can thus be expressed by a single model, even if either dry or steam reforming is the main reaction pathway. Moreover, applicable temperature range can easily be extended. Although the ANN/FIS-based MMR model was established for a Ni-8YSZ anode in a temperature range of 700–800 ^{o}C based on the reforming tests using button-type anode-supported half-cells, it was revealed that the MMR model can be applied for different types of Ni-based catalysts by adjusting a correction factor to compensate the differences in catalytically-active surface area.

The comprehensive CFD model for DIR-SOFCs operating with biogas was established using well-known mathematical models of mass and heat transport, and electrochemical oxidation of H_2 in conjunction with the developed ANN/FIS-based MMR model. The consistency of the MMR-model-incorporated CFD calculation with the measured performance of DIR-SOFC fuelled by CH_4-CO_2 mixture was confirmed through a three-step model validation process consisting of two model-parameter-tuning steps, model fitting steps with the data experimentally obtained under non-DIR and DIR operations, followed by a validity check whether the established-model can reproduce a performance of DIR-SOFC under an arbitrary operating condition. Compared to conventional approaches in literature considering MMR as a sum of CH_4 dry and steam reforming (ignoring the concurrent effect of CO_2 and H_2O on the catalytic CH_4 conversion), the CFD model developed in this study was proved to be able to provide more reliable and meaningful estimation on behavior of internal reforming SOFCs.

Using the developed comprehensive CFD model of DIR-SOFC considering MMR, further numerical analyses were conducted for two DIR concepts to control the internal reforming reactions in two types of Ni-YSZ anode-supported cells (ASCs) that have electrolyte thickness (d_e) of 5 μm and cathode thickness (d_c) of 60 μm but different anode thicknesses (d_a) of 950 (ASC-A) and 200 μm (ASC-B).

- In Concept-I, a thin patterned gas-barrier mask is sintered on the anode surface to control mass flux of fuel entering the anode along fuel flow direction. It was confirmed to suppress rapid syngas production within fuel inlet region, leading to homogeneous temperature distribution over the cell and 20% reduction in maximum thermally-induced stress compared to normal ASCs, in which internal reforming rates are not controlled. Accompanied with only slight drop (about 8%) in power generation, Concept-I could be a good choice for stable operation under fuel utilizations over 70%, especially for ASC-A with thick anode substrate having high content of Ni catalyst.

- In Concept-II, a sheet of Ni-based paper-structured catalyst (PSC) is placed on the anode as an in-cell reformer, increasing the total catalytically-active surface area. Syngas production was confirmed to be promoted by which boosting maximum power density by 7 and 40% compared to normal ASC-A and ASC-B, respectively, although the risk of electrolyte fracture was increased. The effect of Concept-II was more pronounced for ASC-B with thin anode substrate having low content of Ni catalyst.

- In practical applications, anode thickness (or amount of metallic Ni in anode substrate) is an important factor to select a proper cell design for DIR operation. For ASCs with thick anode substrates, Concept-I is promising approach to achieve stable operation without noticeable drop in power generation. For ASCs with thin anode substrates, application of Concept-II is effective to maximize power density; however elevation of thermal stresses has to be taken into consideration.

6.2 Outlook for future work

In this study, a comprehensive CFD model for DIR-SOFCs operating with biogas considering MMR was successfully developed. The model can provide more reliable and meaningful estimation on cell behaviour at any operating conditions compared to conventional approaches, and can be considered as a powerful numerical tool for developing DIR-SOFCs operating with biogas. In pursuit of realizing highly efficient and

robust power generating systems based on biogas-fuelled SOFCs, the following research works can be conducted in future adopting the developed CFD mode.

1. A mixed concept of Concept-I and -II (Concept-III). The effect of Concept-II in improving power generation is more pronounced for ASCs with thin anode substrates, although thermal stresses are increased. To ensure the mechanical stability in the DIR operation, Concept-I is effective, and therefore, the combination of the Concept-I and Concept-II for thin anode substrates may bring about the best operating condition in terms of both mechanical stability and electrochemical performance.

2. Development of functionally-graded PSCs. To minimize the risk of electrolyte fracture caused by rapid CH_4 conversion within the fuel inlet region of a PSC, the use of functionally-graded PSCs, in which amount of Ni loaded is gradually increased along fuel flow direction, is a promising option. By appropriate designs (profile of Ni-loaded amount along fuel flow direction), both complete CH_4 conversion and homogeneous temperature distribution in electrolyte is expected to be simultaneously obtained under open-circuit condition (see Fig. 6.1).

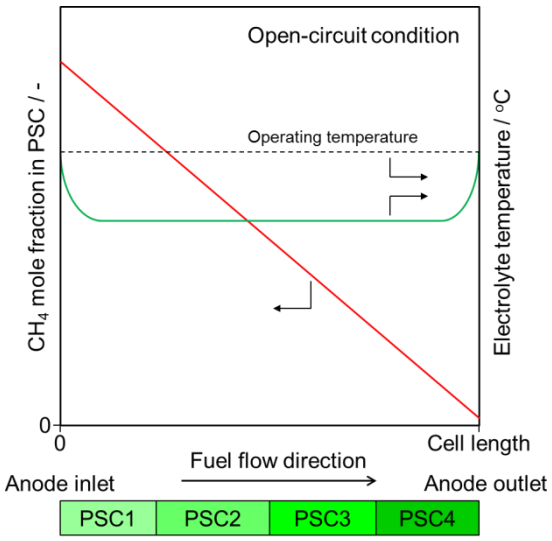

Fig. 6.1: Profiles of (a) CH_4 mole fraction in fuel channel and (b) electrolyte temperature along fuel flow direction expected to be simultaneously obtained with functionally-graded PSC (here, 4 PSCs with Ni-loaded amount elevated in the order of PSC1, PSC2, PSC3 and PSC4) for achieving complete CH_4 conversion with minimum risk of electrolyte fracture under open-circuit condition.

3. Study on modeling of DIR-SOFCs operating with anode off-gas recirculation. As shown in Fig. 6.2, biogas stream (f_{biogas}) can be mixed with a portion of anode off-gas ($f_{a,recir}$) and then supplied to the anode. By this fuel supply configuration, carbon removal is promoted due to elevated S/C ratio of the fuel stream (f_{fuel}); in addition, less temperature drop can be obtained because reforming rates are reduced with decrease in the partial pressure of CH_4 in the fuel stream. The use of anode off-gas recirculation can improve overall system efficiency due to the elimination of external humidifier. However, increase in oxygen-carriers content in the feeding stream can lower maximum power density. Therefore, the degree of the recirculation of off-gas ($k_{a,recir}$) is an important factor and should be defined for practical systems.

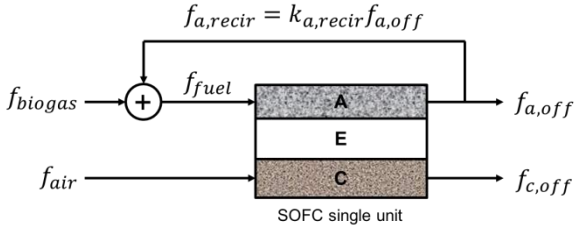

Fig. 6.2: Configuration illustration of anode off-gas recirculation for DIR-SOFCs operating with biogas. f_{biogas} – biogas flow; f_{fuel} – fuel flow; $f_{a,off}$ – anode off-gas flow; f_{air} – air flow; $f_{c,off}$ – cathode off-gas flow; $f_{a,recir}$ – anode recirculation flow; $k_{a,recir}$ – recirculation factor in a range of 0–1.

Appendix A

Effects of H_2O and CO_2 on the electrochemical oxidations of Ni-based SOFC anodes with H_2 and CO as a fuel

Appendix A – Effects of H_2O and CO_2 on the electrochemical oxidations of Ni-based SOFC anodes with H_2 and CO as a fuel

A.1 Effect of H_2O

For the electrochemistry of H_2 at TPB of anode, the overall surface reaction is globally formulated as

$$H_2 + O^{2-}(YSZ) \leftrightarrows H_2O + (YSZ) + 2e^-(Ni) \quad (A.1)$$

,where '()' denotes the surface to which the species is attached. H_2 molecule reacts with an oxygen ion on the YSZ surface ($O^{2-}(YSZ)$) to release two electrons accompanied by steam production. Reaction path of the heterogeneous reaction is rather complex. The reaction is promoted by the presence of H_2O (see Fig. A-1) [1–3]. H_2-spillover mechanism has commonly been used to explain this promotion for Ni-based SOFC anodes [3, 4]. Considering a Ni-based anode, the heterogeneous electrochemistry of H_2 is illustrated in Figure A.2-(a) and described as follows:

+. Adsorption on the Ni surface:

$$H_2 + 2(Ni) \leftrightarrows 2H(Ni) \quad (A.2)$$

$$H_2O + (Ni) \leftrightarrows O(Ni) + H_2 \quad (A.3)$$

+. Surface diffusion of hydrogen atom over the Ni surface to the TPB:

$$H(Ni) \rightarrow H(Ni)_{TPB} \quad (A.4)$$

$$H(Ni) + O(Ni) \rightarrow H(O)(Ni) + (Ni) \quad (A.5)$$

$$H(O)(Ni) \rightarrow H(O)(Ni)_{TPB} \quad (A.6)$$

+. Diffusion of hydrogen atom from the Ni surface to the YSZ surface:

$$H(Ni)_{TPB} + (YSZ)_{TPB} \rightarrow H(YSZ)_{TPB} + (Ni)_{TPB} \quad (A.7)$$

$$H(O)(Ni)_{TPB} + (YSZ)_{TPB} \rightarrow H(YSZ)_{TPB} + O(Ni)_{TPB} \quad (A.8)$$

+. Charge-transfer reactions:

$$O^{2-}(YSZ) + 2H(YSZ)_{TPB} \rightarrow H_2O + 2e^-(YSZ)_{near\ TPB} \quad (A.9)$$

$$e^-(YSZ)_{near\ TPB} \rightarrow e^-(Ni) \quad (A.10)$$

With pure H_2 as a fuel, the formation of H(Ni) species (reaction (A.2)) is the first step of the electrochemical oxidation process. Then, H(Ni) species diffuse over the Ni surface to the TPB (reaction (A.4)), and subsequently to the YSZ surface (reaction (A.7)) where they combine with O^{2-}(YSZ) species to form gaseous H_2O (reaction (A.9)). Simultaneously, two electrons are released to the YSZ surface near by the reaction site and subsequently received by metallic Ni (reaction (A.10]). Therefore, the surface diffusion rate of H_2 to TPB and the electronic conductivity of the cermet electrode in the region vicinity to the TPB strongly affect the rate of H_2 oxidation.

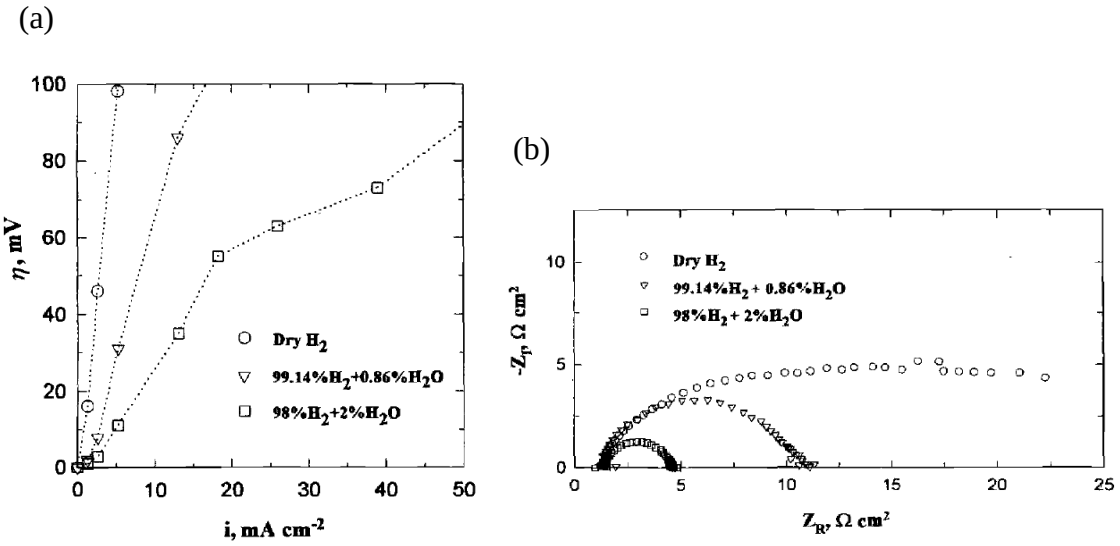

Fig. A.1: Electrochemical behavior of a porous Ni electrode at 1000 ^oC for different H_2O vol% in H_2 gas: (a) anode activation overvoltage and (b) impedance spectra, showing the positive effect of H_2O on promoting the surface diffusion of H_2 to the TPB and the charge-transfer reaction of H_2 [3].

As H_2O appears in anode gas composition, H_2O is dissociated on the Ni surface to form O(Ni) species and H_2 (reaction (A.3)). H(Ni) species can diffuse to active O(Ni) sites (reaction (A.5)), and subsequently travel over active O(Ni) sites toward the TPB (reaction (A.6)), and then diffuse to the YSZ surface (reaction (A.8)) to take part in charge-transfer reactions. O(Ni) concentration increases with increase of the partial pressure of H_2O (p_{H_2O}), and thus the total surface diffusion rate of H_2 to the TPB is significantly enhanced with elevated p_{H_2O}. In addition, the partial pressure of oxygen in anode ($p_{O_2,a}$) varies proportionally to p_{H_2O}, accounting for increase of interfacial conductivity of anode [1, 3]; in consequence, the rates of charge-transfer reactions

(reactions (A.9) and (A.10)) are accelerated with increase of p_{H_2O}. As a result of these, the rate of the electrochemical oxidation of H_2 is promoted with increasing p_{H_2O}.

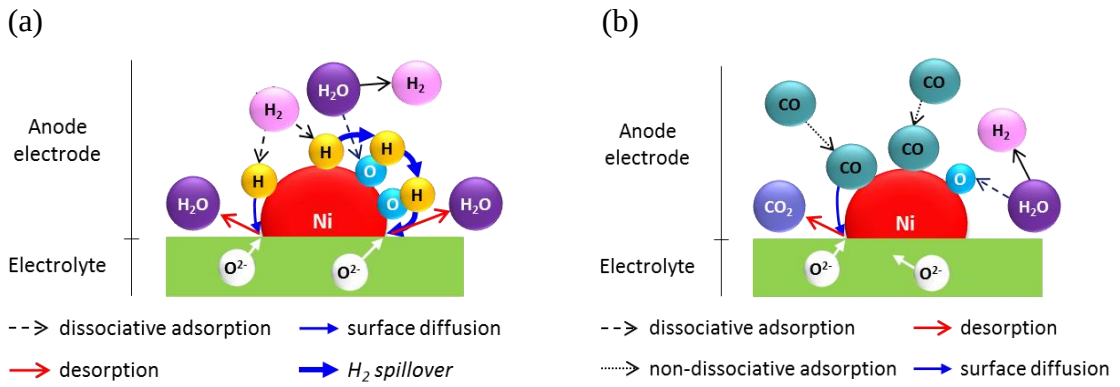

Figure A.2: Mechanism illustrations of the electrochemical oxidations of (a) H_2 and (b) CO on Ni-based SOFC anodes, showing effect of H_2O to both reactions. In H_2 oxidation (a), the surface diffusion rate of H(Ni) to the TPB is promoted by H_2-spillover through O(Ni). In CO oxidation (b), the surface diffusion of CO(Ni) is blocked by O(Ni).

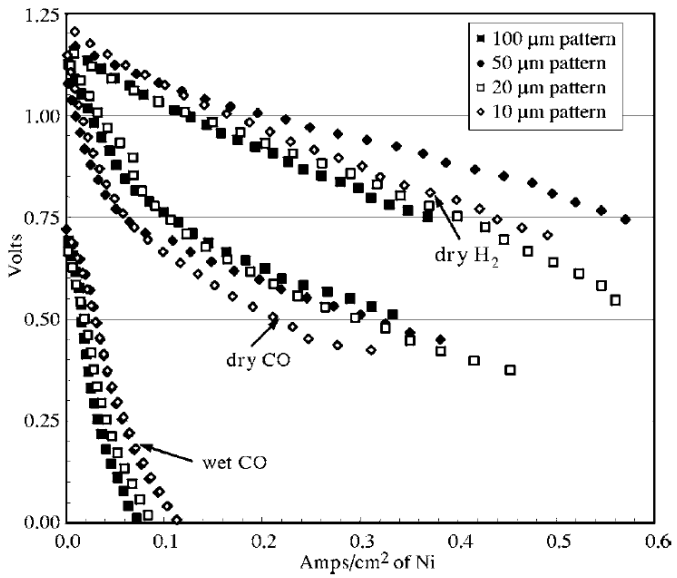

Fig. A.3: *i-V* characteristics of Ni patterned anode at 850 °C with pure H_2, pure CO and humidified CO (4 vol% H_2O) in Ar diluent. Data is shown for patterned anodes constructed by 3-mm-long parallel strips of Ni with different widths (10, 20, 50 and 100 μm) [6].

In the case of the electrochemical oxidation of CO in Ni-based SOFC anodes, the reaction rate is commonly found to be governed by the adsorption rate of CO on the Ni surface, the surface diffusion rate of CO(Ni) to the TPB and the rate of charge-transfer

reactions between CO(Ni) and O^{2-} [5–7]. In the work of Sukeshini *et al.*, anode activation overvoltage with humidified CO (4 vol% H_2O) at low current densities was dramatically increased compared to that with pure CO (see Fig. A.3) [6], indicating that the rate of CO oxidation was reduced because of decrease in CO(Ni) concentration accompanied by the coverage of O(Ni). Moreover, this result revealed that CO(Ni) cannot diffuse over O(Ni) to the TPB, and hence the surface diffusion of CO(Ni) is blocked by O(Ni) (see Fig. A.1-(b)).

A.2 Effect of CO_2

In the work of Jiang and Virkar, power generation characteristics measured at 800 ^oC for H_2 diluted with H_2O were found to be higher than those for H_2 diluted with CO_2 at the same degrees of dilution [8] (see Fig. A.4). Derived from these experimental data, limiting current densities (i_{lim}) and the corresponding fuel utilization (U_f) are listed in Table A.1. As shown in Table A.1, U_f of about 33% was obtained for H_2-H_2O system as the partial pressure (p_{H_2}) in fuel stream increased from 0.2 to 0.5 atm. For H_2-CO_2 system, U_f varied from 20 to 26.1% for p_{H_2} in a range of 0.19–0.5 atm. These values showed that concentration losses in two fuel systems were negligible small, and limiting current densities were mainly governed by the adsorption rate of H_2 on the Ni surface and the surface diffusion rate of H_2 to the TPB. With decrease of p_{H_2}, the adsorption rate of H_2 on the Ni surface was reduced by the coverage of H_2O in H_2-H_2O system or CO_2 in H_2-CO_2 system, primarily leading to decrease in i_{lim}. i_{lim} obtained with the H_2-CO_2 system is 20–44% smaller that with the H_2-H_2O system at the same p_{H_2}, indicating that the surface diffusion of H_2 to the TPB in the H_2-CO_2 system was not promoted as in the H_2-H_2O system (by O(Ni)). It could be inferred that CO_2 adsorption on the Ni surface might not lead to the formation of O(Ni) as in H_2-H_2O systems.

Sumi *et al.* reported that open-circuit voltage in CO-CO_2 systems decreased with increase of partial pressure of CO_2 (p_{CO_2}) due to elevated $p_{O_2,a}$ [9]. In addition, fuel streams with low CO/CO_2 ratio could prevent solid carbon produced from CO disproportionation ($2CO \leftrightarrows C + CO_2$).

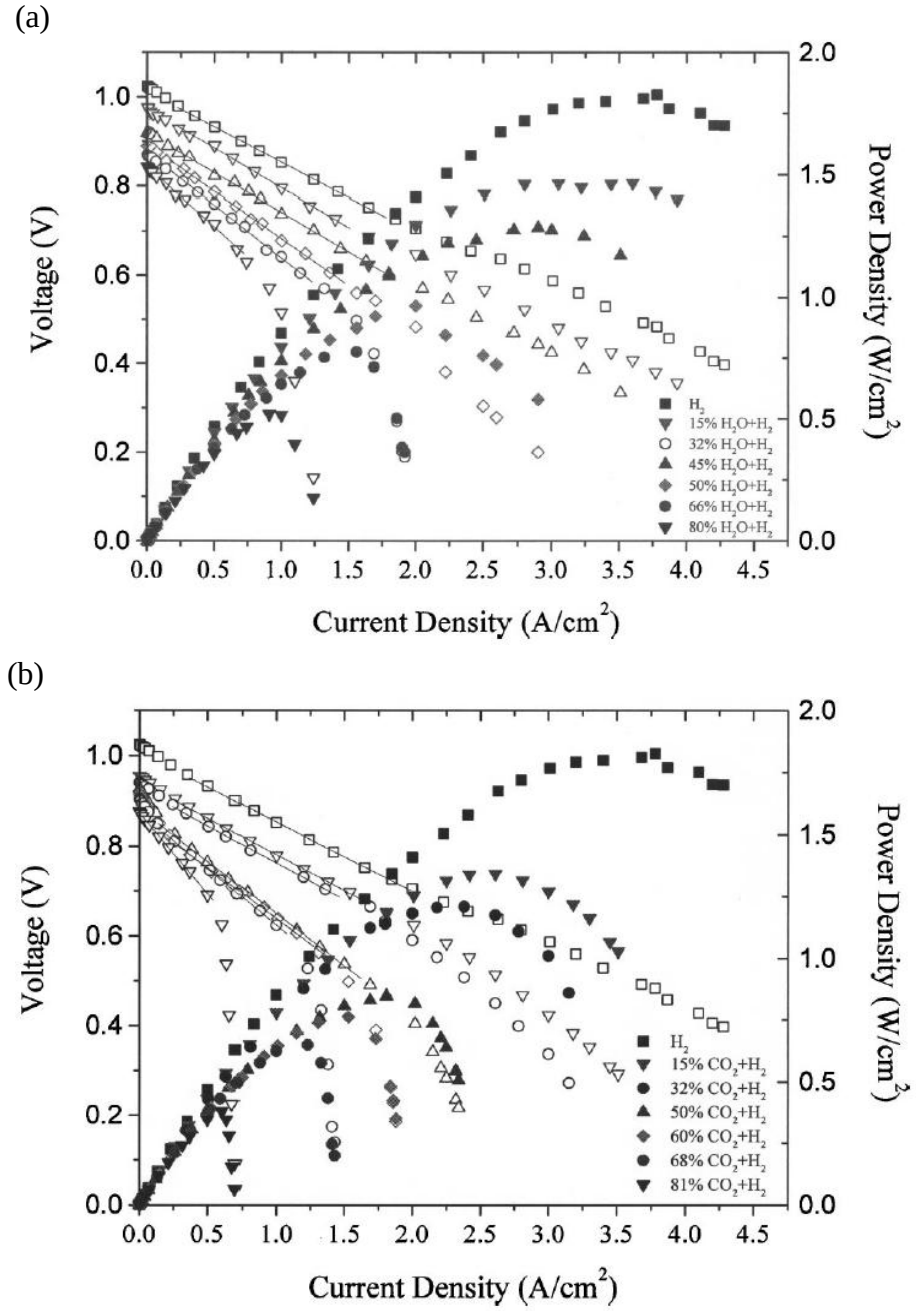

Fig. A.4: *i-V* characteristics of anode supported-SOFC (anode thickness of 1.1 mm and surface area of 1.1 cm^2) at 800 ^oC with fuel flow rate of 140 mL min^{-1}: (a) fuel: H_2-H_2O mixture and (b) fuel: H_2-CO_2 mixture [8].

Table A.1: Limiting current density (i_{lim}) and fuel utilization (U_f) derived from Fig. A.4.

	Fuel: H_2-H_2O		Fuel: H_2-CO_2	
p_{H_2} / atm	i_{lim} / A cm^{-2}	U_f / %	i_{lim} / A cm^{-2}	U_f / %
0.19–0.2	1.25	34	0.7	20
0.32–0.34	2	32	1.4	23.8
0.5	3	32.6	2.4	26.1

A.3 Conclusions

- O(Ni) produced from the dissociation of H_2O on the Ni surface accelerates the surface diffusion of H_2 to the TBP via H_2-spillover mechanism, promoting the electrochemical oxidation of H_2.
- The adsorption of CO on the Ni surface is significantly suppressed by the coverage of H_2O (O(Ni)), and thus the electrochemical oxidation of CO is dramatically reduced if H_2O is present in gas composition.
- The adsorption of CO_2 on the Ni surface does not lead to the formation of O(Ni).
- CO_2 can maintain anode performance against carbon formation caused by Boudouard reaction.

References

[1] J. Mizusaki, H. Tagawa, T. Saito, T. Yamamura, K. Kamitani, K. Hirano, S. Ehara, T. Takagi, T. Hikita, M. Ippommatsu, S. Nakagawa, K. Hashimoto, Kinetics studies of the reaction at the nickel pattern electrode on YSZ in H_2-H_2O atmospheres, Solid State Ionics, 70/71 (1994), 52–58.

[2] A. Bieberle, L.P. Maier, I.J. Gauckler, The electrochemistry of Ni patterns anodes used as solid oxide fuel cell model electrodes, J. Electrochem. Soc. 148(6) (2001) A646–A656.

[3] S.P. Jiang, S.P.S. Badwal, An electrode kinetics study of H2 oxidation on Ni/Y_2O_3–ZrO_2 cermet electrode of the solid oxide fuel cell, Solid State Ionics 123 (1999), 209–224.

[4] W.G. Bessler, J. Warnatz, D.G. Goodwin, The influence of equilibrium potential on the hydrogen oxidation kinetics of SOFC anodes, Solid State Ionics 177 (2007) 3371–3383.

[5] G.Ø. Lauvstad, R. Tunold, S. Sunde, Electrochemical oxidation of CO on Pt and Ni point electrodes in contact with an ytrria-stabilized zirconia electrolyte, J. Electrochem. Soc. 149(2) (2002) E497–E505.

[6] A.M. Sukeshini, B. Habibzadeh, B.P. Becker, C.A. Stoltz, B.W. Eichhorn, G.S. Jackson, Electrochemical oxidation of H_2, CO and CO/H_2 mixtures on patterned Ni anodes on YSZ electrolytes, J. Electrochem. Soc. 153(4) (2006) A705–A715.

[7] V. Yurkiv, D. Starukhin, H.-R. Volpp, W.G. Bessler, Elementary reaction kinetics of the CO/CO_2/Ni/YSZ electrode, J. Electrochem. Soc. 158(1) (2011), B5–B10.

[8] Y. Jiang, A.V. Virkar, Fuel composition and diluent effect on gas transport and performance of anode-supported SOFCs, J. Electrochem. Soc. 150(7) (2003) A942–A951.

[9] H. Sumi, Y.H. Lee, H. Muroyama, T. Matsui, K. Eguchi, Comparison between internal steam and CO_2 reforming of methane for Ni-YSZ and Ni-ScSZ SOFC anodes, J. Electrochem. Soc. 157(8) (2010), B1118–B1125.

Appendix B

Overview of Artificial Neural Network

B.1 Introduction

An Artificial Neural Network (ANN) is a computational model based on the structure and functions of biological neural networks. An ANN can be trained to express the internal relationship and estimate system behavior without any physical equations. ANNs are thus universal approximators which produce output data as a response to a specific combination of input data. The use of ANNs is effective if systems of interest are difficult to be described adequately with conventional approaches because of the large number of variables and the great diversity of data.

B.2 History

The concept of ANNs as computing machines was first introduced in 1943 by McCulloch and Pitts [1]. Their works showed that any arithmetic or logical functions could, in principle, be represented by a network of artificial neurons (see Fig. B-1). In 1958, Rosenblatt and his colleagues demonstrated the capability of a single neuron consisting of a summing node followed by a hard-limiter (see Fig. B-2(a)) to perform the classification of two linearly-separable patterns (two classes are able to be separated by a line). Although this simple ANN, namely a single-layer perception network, was limited as a binary classifier (whether an input belongs to a specific class or not), it has been acknowledged as the first practical application of ANNs. At the same time, Widrow and Hoff introduced a training algorithm for a single-layer linear perceptron network, of which output data is the linear combination of input data (see Fig. B-2-(b)). During the 1960s–70s, theories of ANNs were slowly developed due to the lack of new ideas and powerful computers to realize them. From the 1980s, personal computers and workstations rapidly matured in capability, leading to significant increase in new concepts for ANNs. One of the key developments in the 1980s was the learning algorithm based on the backward propagation of error (so-called backpropagation algorithm), which was reported independently by several different researchers. By this achievement, complex multilayer ANNs can

successfully be trained for arbitrary tasks. At the present, ANNs find countless applications in aerospace, transportation, telecommunications, securities, speech, robotics, banking, medical, etc.

In the field of fuel cell modeling, Saengrung *et al.* trained an ANN to predicted output voltage and current of a commercial proton exchange membrane fuel cell (PEMFC) stack with respect to air flow rate and stack temperature [2]. Arrigada *et al.* developed an ANN-based simulator receiving fuel utilization, cell voltage, fuel flow rate and fuel inlet temperature as input data for estimating operational parameters of solid oxide fuel cell (SOFC) including air flow, current density, air and fuel outlet temperatures, and mean solid temperature [3]. Milewski and Swirski trained an ANN for predicting i-V curves of an SOFC associated with working conditions (current density, temperature, fuel and air flow rates) and cell structure (electrolyte thickness, anode thickness and porosity) [4]. Marra *et al.* reported a neural network estimator of 5-cell SOFC stack for diagnostics applications [5]. This network could predict cell degradation (the drop in cell voltage) over long-term operation with respect to current density, fuel flow rate and inlet temperature, air flow rate and operating time.

B.3 Principle

An artificial neuron is the basic processing element of an ANN. Simulating basic functions of biological neurons, an artificial neuron receives input data (x) from other sources, processes them in some way, and then outputs the final result (y) to the next neurons (see Fig. B.1). The correlation between x and y is numerically expressed as

$$y = \varphi(wx + b) \tag{B.1}$$

,where $x = [x_1, .., x_n]^{\mathrm{T}}$ is the input vector ($[.]^{\mathrm{T}}$ is the transpose of the vector); n is the number of inputs; y is the output value; w is the weight vector, of dimension $n \times 1$; b is the bias; and $\varphi(.)$ is the activation function (see Fig. B.3).

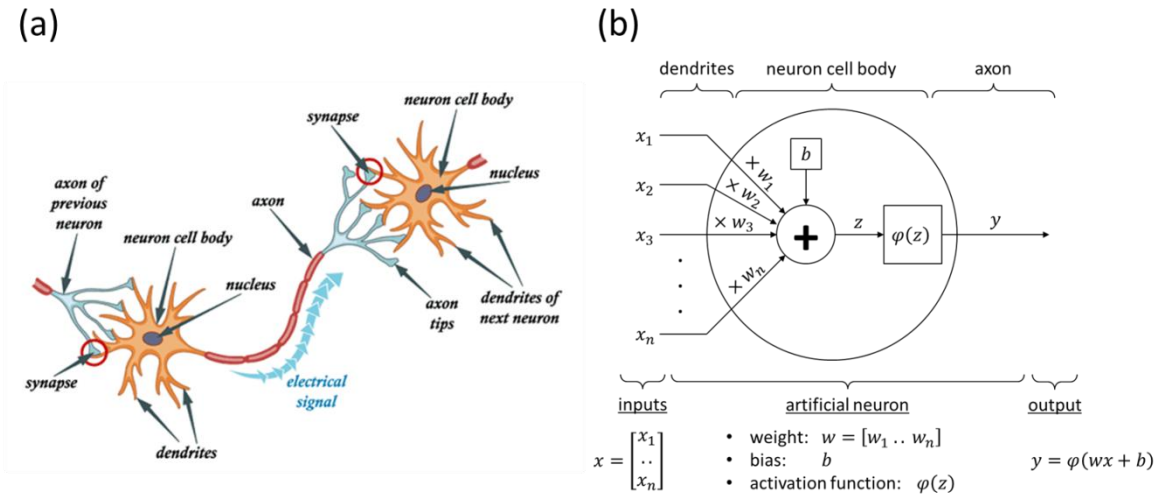

Figure B.1: Illustrations of (a) biological neuron [6] and (b) McCulloch-Pitts's model of artificial neuron.

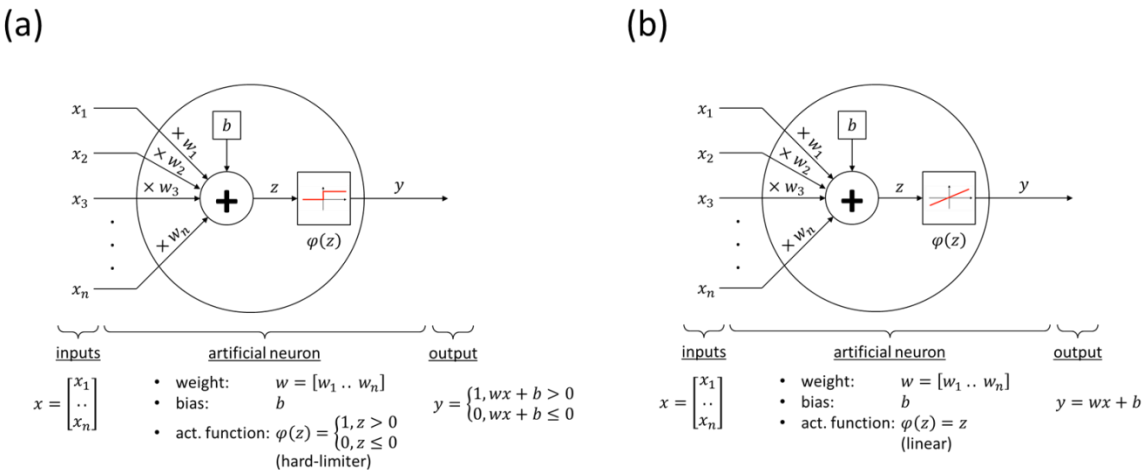

Figure B.2: Single-layer perceptron network: (a) Rosenblatt's neuron model and (b) Widrow-Hoff's neuron model.

Activation function	Equation	Example	1D Graph
Unit step (Heaviside)	$\phi(z) = \begin{cases} 0, & z < 0, \\ 0.5, & z = 0, \\ 1, & z > 0, \end{cases}$	Perceptron variant	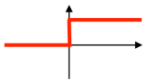
Sign (Signum)	$\phi(z) = \begin{cases} -1, & z < 0, \\ 0, & z = 0, \\ 1, & z > 0, \end{cases}$	Perceptron variant	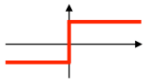
Linear	$\phi(z) = z$	Adaline, linear regression	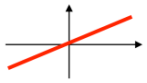
Piece-wise linear	$\phi(z) = \begin{cases} 1, & z \geq \frac{1}{2}, \\ z + \frac{1}{2}, & -\frac{1}{2} < z < \frac{1}{2}, \\ 0, & z \leq -\frac{1}{2}, \end{cases}$	Support vector machine	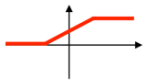
Logistic (sigmoid)	$\phi(z) = \frac{1}{1 + e^{-z}}$	Logistic regression, Multi-layer NN	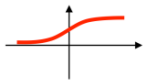
Hyperbolic tangent	$\phi(z) = \frac{e^{z} - e^{-z}}{e^{z} + e^{-z}}$	Multi-layer NN	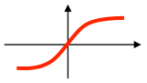

Figure B.3: Typical activation functions used in ANNs [7].

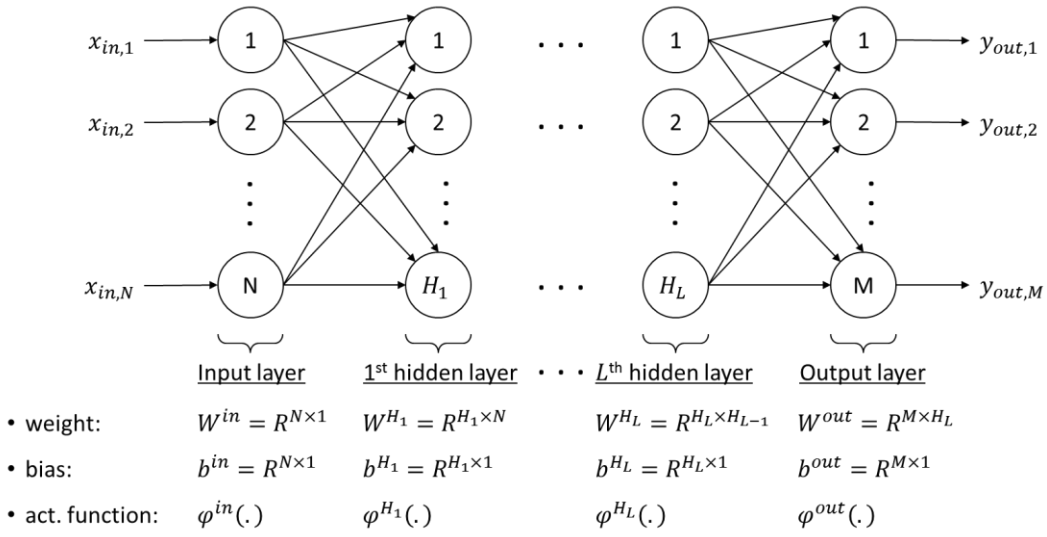

Figure B.4: Schematic illustration of the feed-forward multilayer ANN. Circle indicates the artificial neuron (computing node). Arrow indicates the connection between two neurons. N is the number of neurons in the input layer. L is the number of hidden layers. H_k is the number of neurons in the k^{th} hidden layer. M is the number of neurons in the output layer. $R^{m\times n}$ is the real matrix having m rows and n colums.

As shown in Figure B.4, an ANN is typically organized in interconnected layers, consisting of one input layer, several hidden layers and one output layer. Each layer is composed of a number of artificial neurons. A neuron in one layer receives output values from all neurons in the preceding layer, and delivers its output value to all neurons in the next layer. Usually, neurons in a layer contain the same type of activation function to simplify the learning process. The response of an ANN with respect to input data is governed by the number of layers, the number of neurons in each layer, as well as the weights, bias and activation function of each neuron.

A multilayer ANN with appropriate design, weights and biases can exactly reproduce the relationship between inputs and outputs of a practical system. Network parameters are determined through a learning (or training) process, in which weights and biases are adjusted so that for the same input data (x_{in}) the deviations between system and network outputs (y_{sys} and y_{out}, respectively) are minimized. Backpropagation learning algorithm has commonly been used in conjunction with an optimization method such as gradient descent, and the learning rule (parameter-adjustment mechanism) is described as follow

$$w_{i,j}^{k}(s+1) = w_{i,j}^{k}(s) - \alpha \frac{\partial C(x_{in})}{\partial w_{i,j}^{k}} \tag{B.2}$$

$$b_{i}^{k}(s+1) = b_{i}^{k}(s) - \alpha \frac{\partial C(x_{in})}{\partial b_{i}^{k}} \tag{B.3}$$

,where $w_{i,j}^{k}$ is the weight of the i^{th} neuron in the layer k (input, hidden and output layers) for its j^{th} input; b_{i}^{k} is the bias of the corresponding neuron; α is the learning-rate constant; s is the iteration; and $C(x_{in})$ is the cost function which is usually expressed in terms of the square error as

$$C(x_{in}) = e^{\mathrm{T}}e \tag{B.4}$$

,where $e = y_{sys} - y_{out}$ is the network error with respect to x_{in}. Depending on $\varphi(.)$, $\partial C(x_{in})/\partial w_{i,j}^{k}$ and $\partial C(x_{in})/\partial b_{i}^{k}$ are analytically determined.

Prior to the learning process, all $w_{i,j}^k$ and b_i^k are set to random values, and α is pre-defined. In the first iteration (s = 1), y_{out} is calculated with respect to x_{in}, subsequently, e and $C(x_{in})$ are sequentially solved. If $C(x_{in})$ is larger than a pre-defined threshold ε, $\partial C(x_{in})/\partial w_{i,j}^k$ and $\partial C(x_{in})/\partial b_i^k$ are determined, followed by the adjustments of $w_{i,j}^k$ and b_i^k (Eqs. (B.2) and (B.3)). The learning process is repeated until $C(x_{in}) < \varepsilon$ is satisfied, and network parameters are said to be converged.

With a well-trained ANN, outputs of the practical system can quickly be estimated from inputs without the detailed descriptions of system processes. Therefore, the ANN can be considered to be the black-box model of the system.

Reference

[1] M.T. Hagan, H.B. Demuth, M.H. Beale, O.D. Jesús, Neural Network Design, 2nd Edition, eBook, ISBN-13: 978-0971732117.

[2] Saengrung, A. Abtahi, A. Zilouchian, Neural network model for a commercial PEM fuel cell system, J. Power Sources 172 (2007) 749–759.

[3] J. Arriagada, P. Olausson, A. Selimovic, Artificial neural network simulator for SOFC performance prediction, J. Power Sources 112 (2002) 54–60.

[4] J. Milewski, K. Swirski, Modelling the SOFC behaviours by artificial neural network, Int. J. Hydrogen Energy 34 (2009) 5546–5553.

[5] D. Marra, M. Sorrentino, C. Pianese, B. Iwanchitz, A neural network estimator of solid oxide fuel cell performance for on-field diagnostics and prognostics applications, J. Power Sources 241 (2013) 320–329.

[6] https://medium.com/autonomous-agents/mathematical-foundation-for-activation-functions-in-artificial-neural-networks-a51c9dd7c089.

[7] https://www.quora.com/What-is-the-role-of-the-activation-function-in-a-neural-network.

Appendix C

Overview of Fuzzy Inference System

C.1 Introduction

In everyday situations, instead of manipulating precise valuations, human brain uses linguistic descriptions to express information (e.g. velocity) as degrees of truth (e.g. too slow, slow, fast and too fast), and makes judgments in imprecise terms (e.g. if the car velocity is too slow then push the acceleration pedal hard). A fuzzy inference system (FIS) is a computational model which processes data in the same manner that human brain does, in which a given input is mapped to an output using fuzzy logic. Different from classical logic, a statement in fuzzy logic is no longer true (1) or false (0) but rather as partially truth (many values between 0 and 1). By adopting FIS, experience of people in solving a problem can be encoded. The problem can thus be solved without knowing its mathematical descriptions, which are mandatorily required by conventional approaches.

C.2 History

Fuzzy sets and *fuzzy logic* were first introduced in 1965 by Zadeh [1]. In its early days, fuzzy logic theory was not well received because some of mathematical terms had not yet been explored. In 1973, he published a paper introducing the concept of *linguistic variable* to express a variable in terms of fuzzy sets. This work provided the methodology of designing controllers using fuzzy logic theory, attracting other researchers to develop fuzzy logic theories and apply FIS to practical applications.

In 1975, Mamadani and Assilian succeeded in controlling a steam engine with a fuzzy controller using a set of control rules based on experience from manual operation [2]. Their work has been acknowledged as the first practical application of FIS. Moreover, they showed that processes that had never been successfully automated before could be controlled by FISs which encoded experience of human operators.

In 1982, Holmblad and Østergaard established a fuzzy controller with 27 rules to control the wet process cement kiln for a cement plant in Denmark, known as the first

industrial application of FIS [3]. This work was greatly impressive since the plant was attributed to time-varying, nonlinear behavior and only few measurements available.

In 1985, Yasunobu and Miyamoto of Hitachi demonstrated the feasibility of FISs for automatically controlling acceleration, braking and stopping of trains in a subway system [4]. In 1987, these FIS-based automatic train operation systems were realized to the Sendai Subway System. Although at least one human operator must still be aboard each train to take over in case of a breakdown or other emergency, it was the first time that the safety of large numbers of people was entrusted, even in part, to a fuzzy control device.

In 1988, the Laboratory for International Fuzzy Engineering (LIFE), a cooperative arrangement between 48 companies to pursue fuzzy research, was found in Japan, leading to "fuzzy boom" in industrial applications as well as consumer goods from the end of 1980s. Some practical applications adopting FIS can be listed as group control in elevators (Hitachi), ventilation systems in expressway tunnels (Toshiba), city garbage incinerator (Mitsubishi Heavy Industries), water treatment plant (Fuji), vacuum cleaner (Matsushita), air conditioner (Mitsubishi), washing machine (Hitachi), fuzzy autofocus still camera (Canon).

FISs have been successfully applied to many fields such as automatic control, data classification, decision analysis, expert systems, and computer vision. FISs are associated with a number of names, such as fuzzy-rule-based systems, fuzzy expert systems, fuzzy modeling, fuzzy associative memory, fuzzy logic controllers, and (simply) fuzzy systems.

C.3 Principle

In FIS point of view, a mathematical variable z (e.g. temperature) is considered as a linguistic variable having N linguistic values, $V_{i=1..N}$, (e.g. N = 3, V_1 = 'cold', V_2 = 'warm' and V_3 = 'hot'). Each V_i is expressed by a fuzzy set, Z_i, usually having a shape of triangle (see Fig. C.1-(a)), or trapezoid (see Fig. C.1-(b)), or is a singleton-type (see Fig. C.1-(c)),

corresponding to a membership function, $\mu_i(z)$, which maps the real value of z into a membership value in a range of 0–1. $\mu_i(z) = 1$ indicates that z is absolutely V_i, whereas $\mu_i(z) = 0$ means that z is absolutely not V_i. $0 < \mu_i(z) < 1$ shows that $z = V_i$ is partially true.

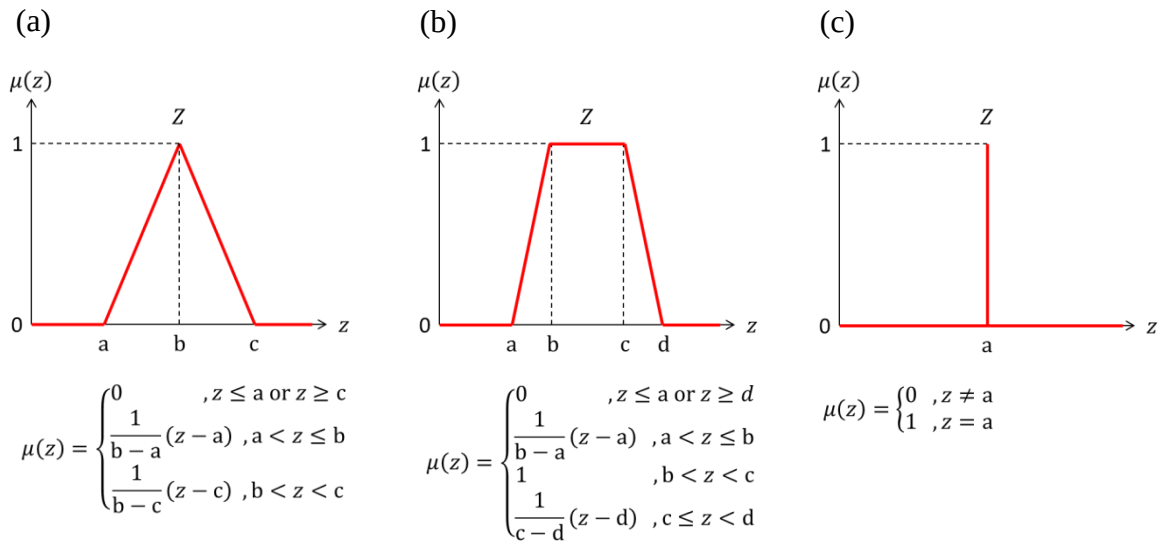

Fig. C.1: Typical fuzzy sets: (a) triangle-shape, (b) trapezoid-shape and (c) singleton-type.

Considering a simple FIS having an input x and an output y. $V_{x,i=1..N}$ and $V_{y,i=1..N}$ are linguistic values of x and y, respectively. Fuzzy sets of x, $X_{i=1..N}$, are triangle-shape (see Fig. C.2-(a)) while fuzzy sets of y, $Y_{i=1..N}$, are singleton-type (see Fig. C.2-(b)). Operation of a FIS to map a real value x_{in} to a real value y_{out} is performed through three following processing steps (see Fig. C-3).

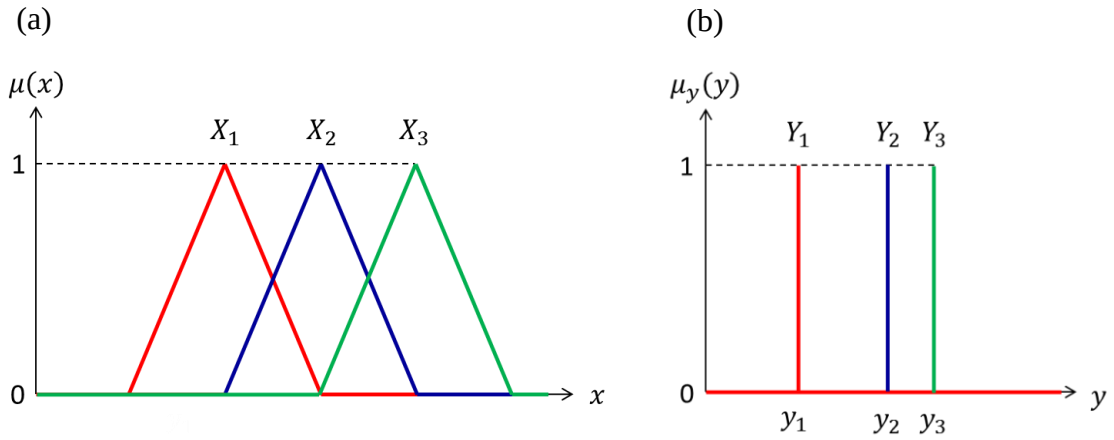

Fig. C.2: Example of fuzzy sets for a variable: (a) input, x, and (b) output, y. N = 3.

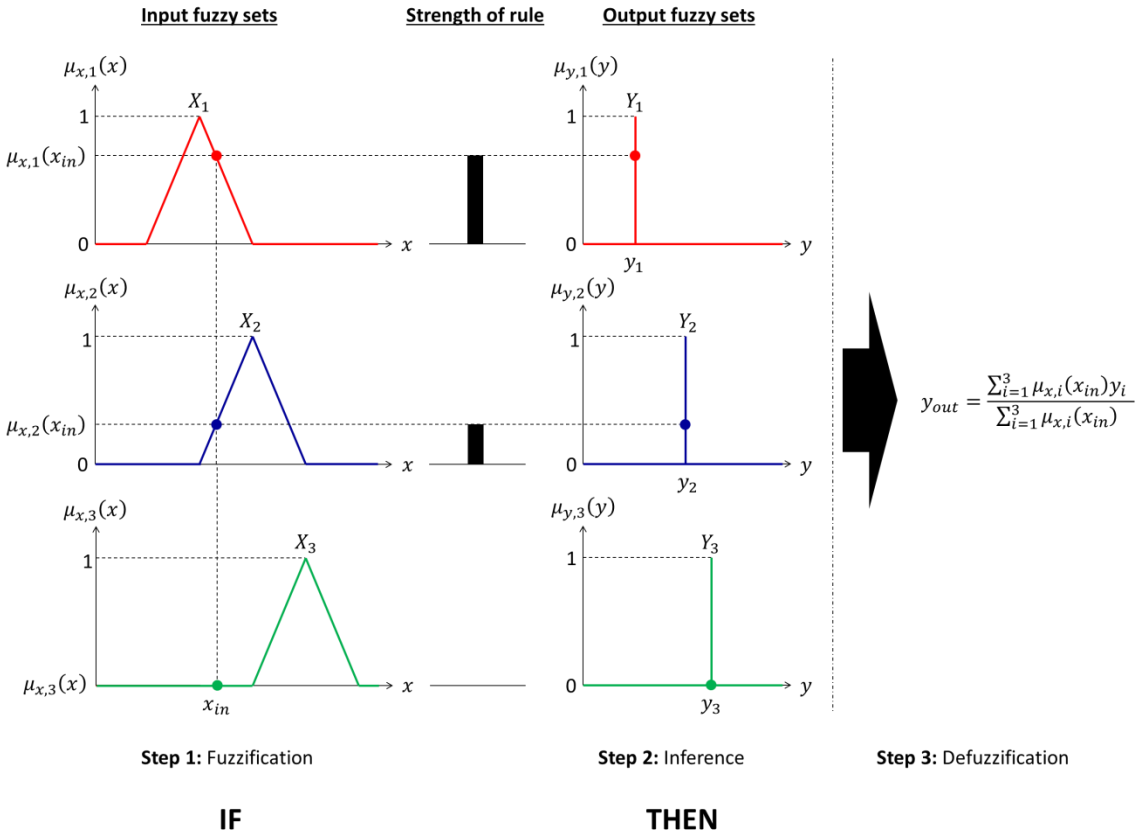

Fig. C.3: Operation mechanism of a FIS to map x_{in} into y_{out} using fuzzy sets in **Fig. C-2** and weighted average as defuzzification method.

Step 1: Fuzzification. All $\mu_{x,i=1..N}(x = x_{in})$ are computed.

Step 2: Inference. The correlation between x and y is expressed by a set of N IF-THEN rules as follow

$$\text{IF } x \text{ is } V_{x,i} \text{ THEN } y \text{ is } V_{y,i}.$$

The strength of the ith rule is represented by $\mu_x(x_{in})$.

Step 3: Defuzzification. Since $Y_{i=1..N}$, are singleton-type, the final y_{out} can be determined as a weighted average value:

$$y_{out} = \frac{\sum_{i=1}^{3} \mu_{x,i}(x_{in}) y_i}{\sum_{i=1}^{3} \mu_{x,i}(x_{in})}.$$

Reference

[1] L.A. Zadeh, Fuzzy sets, Information and Control 8(3) 1965 338–353.
[2] Mamdani, H. Ebrahim, Application of fuzzy algorithms for control of simple dynamic plant, Proceedings of the Institution of Electrical Engineers 112(2) (1974) 1585–1588.
[3] J.J. Østergaard, High level process control in the cement industry by fuzzy logic.
[4] H.B. Verbruggen, R.Babuska, Fuzzy Logic Control: Advances in Applications, 1999.